National Technical University of Athens
School of Mechanical Engineering
Lab. of Thermal Turbomachines
Parallel CFD & Optimization Unit

Optimization of Cooling Ducts using the Continuous Adjoint Method for Conjugate Heat Transfer Problems

Diploma Thesis

Koukougkelis Georgios

Supervisor: Kyriakos C. Giannakoglou, Professor NTUA

Athens, July 15, 2023

Acknowledgments

I would like to take this opportunity to express my deepest gratitude to the individuals who have contributed to the completion of this thesis.

First and foremost, I am immensely grateful to my supervisor, Professor Kyriakos C. Giannakoglou, for their invaluable guidance, unwavering support, and expert knowledge throughout this research journey. Their insightful feedback, constructive criticism, and dedication have been instrumental in shaping the direction and quality of this thesis. I am truly fortunate to have had the opportunity to work under their supervision. I would also like to express my

sincere gratitude to Dr. Evangelos Papoutsis-Kiachagias and Nikolaos Galanos (Ph.D. student), who are part of the Parallel CFD & Optimization Unit of the NTUA (NTUA) team. Their technical expertise in OpenFOAM$^{©}$and precise suggestions have been essential to my progress.

National Technical University of Athens
School of Mechanical Engineering
Lab. of Thermal Turbomachines
Parallel CFD & Optimization Unit

Optimization of Cooling Ducts using the Continuous Adjoint Method for Conjugate Heat Transfer Problems

Diploma Thesis

Koukougkelis Georgios

Advisor: Kyriakos C. Giannakoglou, Professor NTUA

Athens, July 15, 2023

Abstract

The goal of this diploma thesis is to investigate the utilization of the continuous adjoint method for optimizing problems involving Conjugate Heat Transfer (CHT) in Computational Fluid Dynamics (CFD). The areas of focus in this context encompass Shape Optimization (ShpO) and Topology Optimization (TopO), where various cases are addressed and dealt with. Special emphasis is given to the known problems of TopO occurring due to the absence of a clearly defined Fluid-Solid Interface (FSI), which subsequently results in the inability to impose Boundary Conditions (BCs) on it.

The applications examined exclusively pertain to laminar flows of incompressible fluids that are governed by the steady-state Navier-Stokes (NS) equations. The relevant software used for the analysis and optimization has been developed by the PCOpt/NTUA based on the open-source CFD toolbox OpenFOAM$^{©}$.

The first application deals with the analysis and optimization of the cooling duct of a 2D turbine blade-like geometry. A serpentine-like duct is initially designed and optimized through ShpO. The primal problem is then solved using the TopO code in order to identify differences in the results between this solution approach and the conventional one using body-fitted meshes. Several TopO cases are conducted and the geometries produced are evaluated.

The second application addresses the design of a 2D duct system. This time, an initial design of the duct is produced by TopO. Body-fitted meshes for both the fluid and solid regions are produced based on the computed optimal porosity field. After the TopO results are compared with those produced on the body-fitted mesh, several ShpO cases are performed on the geometry.

Εθνικό Μετσόβιο Πολυτεχνείο
Σχολή Μηχανολόγων Μηχανικών
Εργαστήριο Θερμικών Στροβιλομηχανών
Μονάδα Παράλληλης ΥΡΔ & Βελτιστοποίησης

Βελτιστοποίηση Αγωγών Ψύξης με τη Συνεχή Συζυγή Μέθοδο για Προβλήματα Συζευγμένης Μεταφοράς Θερμότητας

Διπλωματική εργασία

Κουκουγκέλης Γεώργιος

Επιβλέπων: Κυριάκος Χ. Γιαννάκογλου, Καθηγητής ΕΜΠ

Αθήνα, July 15, 2023

Περίληψη

Ο στόχος της παρούσας διπλωματικής εργασίας είναι η διερεύνηση της χρήσης της συνεχούς συζυγούς μεθόδου σε προβλήματα συζευγμένης μεταφοράς θερμότητας στην Υπολογιστική Ρευστοδυναμική (ΥΡΔ). Σε αυτό το πλαίσιο εξετάζονται προβλήματα βελτιστοποίησης μορφής και τοπολογίας σε διάφορες εφαρμογές. Ιδιαίτερη έμφαση δίνεται στα γνωστά προβλήματα της βελτιστοποίησης τοπολογίας που προκύπτουν λόγω της έλλειψης σαφώς ορισμένου ορίου μεταξύ ρευστών-στερεών περιοχών, γεγονός που οδηγεί στην αδυναμία επιβολής οριακών συνθηκών σε αυτό.

Οι εφαρμογές που εξετάζονται αφορούν αποκλειστικά τις στρωτές ροές ασυμπίεστων ρευστών που διέπονται από τις χρονικά μόνιμες Navier-Stokes εξισώσεις. Το σχετικό λογισμικό που χρησιμοποιήθηκε για ανάλυση και βελτιστοποίηση έχει προγραμματιστεί από την ΜΠΥΡ&Β/ΕΜΠ βασισμένο στο περιβάλλον ανοιχτού κώδικα OpenFOAM©.

Η πρώτη εφαρμογή αφορά την ανάλυση και βελτιστοποίηση ενός αγωγού ψύξης 2Δ πτερυγίου στροβιλομηχανής. Αρχικά σχεδιάζεται ένας καμπύλος αγωγός ο οποίος βελτιστοποιείται εφαρμόζοντας βελτιστοποίηση μορφής. Έπειτα, το πρωτεύον πρόβλημα λύνεται με χρήση του κώδικα βελτιστοποίησης τοπολογίας με σκοπό την διερεύνηση των διαφορών στα αποτελέσματα μεταξύ της συγκεκριμένης προσέγγισης επίλυσης και αυτή της συμβατικής με χρήση σωματόδετων πλεγμάτων. Πραγματοποιούνται διάφορες εφαρμογές βελτιστοποίησης τοπολογίας και οι προκύπτουσες γεωμετρίες αξιολογούνται.

Η δεύτερη εφαρμογή αφορά τον σχεδιασμό ενός 2Δ συστήματος αγωγών. Αυτή τη φορά, η αρχική γεωμετρία των αγωγών προκύπτει από βελτιστοποίηση τοπολογίας. Έπειτα, γενώνται σωματόδετα πλέγματα για τις ρευστές και στερεές περιοχές βάσει του βελτιστοποιημένου πορώδους πεδίου. Αφού τα αποτελέσματα του πρωτεύοντος προβλήματος της βελτιστοποίησης τοπολογίας συγκριθούν με αυτά που προκύπτουν με την συμβατική προσέγγιση επίλυσης, πραγματοποιούνται διάφορα τρεξίματα βελτιστοποίησης μορφής της γεωμετρίας.

Abbreviations

ABC	Adjoint Boundary Condition
AD	Automatic Differentiation
BC	Boundary Condition
BFGS	Broyden–Fletcher–Goldfarb–Shanno
BFM	Body-Fitted Mesh
CFD	Computational Fluid Dynamics
CHT	Conjugate Heat Transfer
CP	Control Point
DD	Direct Differentiation
FAE	Field Adjoint Equations
FD	Finite Difference
FI	Field Integral
FSI	Fluid-Solid Interface
GBM	Gradient-Based Method
ISQP	Implicit SQP
KKT	Karush-Kuhn-Tucker
MMA	Method of Moving Asymptotes
NS	Navier-Stokes
NTUA	National Technical University of Athens
PBF	Primal Body-Fitted
PCOpt/NTUA	Parallel CFD & Optimization Unit of the NTUA
PDE	Partial Differential Equation
PM	Porosity Mesh
PPB	Primal Porosity-Based
r.h.s.	right hand side
SD	Sensitivity Derivatives
ShpO	Shape Optimization
SIMP	Solid Isotropic Material Penalization
SQP	Sequential Quadratic Programming
TopO	Topology Optimization
VBS	Volumetric B-Splines
w.r.t.	with respect to

Contents

Chapter 1

Introduction

In the last decades, advancements in the design of gas turbines are directed toward continuously improving output power and thermal efficiency. Both of those objectives are dependent upon the increase of turbine entry temperature which is limited by the melting point of the materials used. For this reason, state-of-the-art gas turbines employ efficient coolant systems to allow turbine blades to survive under excessive thermal loads. Blade cooling channels are characterized by complex geometries the performant design of which, demands numerous simulations and experiments to accomplish. Therefore, optimization methods can be utilized as an effective way to achieve cooling structures with higher overall performance.

1.1   Turbine Blade Cooling

Advanced gas turbines operate in temperatures that are far above the ones permissible by the metal. To ensure safe operation and structural integrity, cooling of the blades is necessary. In most cases, the coolant is air bled from the high-pressure compressor, which bypasses the combustor and enters the blades through their roots. This extraction of air incurs a severe penalty to the thermal efficiency making it crucial to optimize the cooling technique. Several methods are utilized that cool the blade both internally and externally.

Internal cooling is achieved by passing the coolant through several serpentine passages lined with rib turbulators. Also, internal cooling is enhanced through impingement and pin-fin cooling. Impingement cooling is used near the leading edge of the blade where the thermal load is the greatest and also the blade walls are thick enough to sustain the impact with the cooling jets. Pin-fin cooling is used in the very narrow trailing edge of the blade due to manufacturing restrictions. As the coolant flows past the pins, the flow separates and wakes are shed reinforcing the extraction of heat from the outside of the blade.

External cooling is also called film cooling. Coolant air is ejected from the inside of the blade to the outside surface through discrete holes or slots, forming a protective layer between the blade surface and the hot combustion gases. The aforementioned cooling methods are described in great detail in [1–4].

For an effective cooling system design, it is critical to ensure that the maximum temperatures and temperature spatial gradients during operation do not

1

exceed the maximum blade thermal stress. Additionally, the coolant mass flow rate and total pressure drop in the cooling channels should be minimal, considering the impact that those have on the thermal efficiency of the gas turbine.

1.2   Gradient-Based Optimization

Optimization problems are generally characterized by the objective function J, the design or optimization variables b_n and the constraints. The objective function is the quantity to be either maximized or minimized. Design variables are controllable parameters of the system and constraints place limits to problem quantities. The goal of the optimization is to find the set of design variables that maximizes/minimizes the value of the objective function while the constraints are satisfied.

Optimization methods are divided into stochastic [5–7] and deterministic or gradient-based [8–11]. In the context of this thesis, only Gradient-Based Methods (GBMs) are studied and used. The gradient-based optimization algorithms start with a given set of design variables and improve it based on information related to the derivatives of the objective function with respect to (w.r.t.) the design variables (also referred to as Sensitivity Derivativess (SDs)). Since the direction along which the design variables should be updated is dictated by the SDs, a GBM can be trapped into a local minimum/maximum where the values of the SDs are zeroed. In such cases, an optimized solution is obtained rather than the optimal one. It is possible to get another solution by starting the optimization algorithm from a different set of design variables.

The efficiency of GBMs strongly depends on the method used to compute the required SDs. Known methods for computing SDs are:

- Finite Differences (FDs)

- Complex Variable Method [12]

- Direct Differentiation (DD) [13]

- Automatic Differentiation (AD) [14]

- Adjoint Methods [15, 16]

While the FDs method is straightforward to implement, its cost scales linearly with the number of design variables, N, making it unsuitable for large-scale optimization problems. Another disadvantage of the method is the selection of an appropriately small step size in the computation of the discretized gradient formula in order to minimize the truncation error. While a small step size is beneficial, it cannot be arbitrarily decreased or the round-off error can become significant, [17].

The error due to round-off can be circumvented by using the complex variable method [12]. Nevertheless, the cost of the method is again linearly proportional to the number of the design variables, N, making it infeasible for the problems studied in this thesis.

The DD method [13] is formulated by differentiating the system equations and the objective function w.r.t. the design variables. A total of N new systems

of equations arise, which include the variations of the primal problem variables. The SDs can be computed by solving the primal equations and the N newly derived systems of equations. Therefore, the cost of DD is proportional to the number of design variables.

The AD technique [14] provides accurate numerical approximations of derivatives by applying the chain rule repeatedly to a sequence of elementary arithmetic operators and functions. Even though AD (in reverse mode) can compute derivatives for a cost independent of the number of design variables, it creates codes with significant memory usage since it stores intermediate values during the computation of derivatives, which can become a problem in large-scale applications.

Among the aforementioned methods for the computation of SDs, the adjoint method [15, 16] is the one used in this thesis. This is due to the fact that the cost of computing the necessary derivatives with this method is practically independent of the number of design variables. Moreover, it is applicable to a wide range of problems while being more memory-efficient than AD.

Adjoint methods are classified into continuous and discrete. In continuous adjoint [15, 18, 19], the objective function is augmented by the residuals of the primal equations in their continuous form (prior to their discretization). By the proper mathematical development of the augmented objective function, the adjoint Partial Differential Equations (PDEs) and their BCs arise, which can be numerically solved to produce the fields of the adjoint variables. In contrast, in discrete adjoint [16, 20, 21], the objective function is augmented by the discretized residuals of the primal equations. The adjoint system of equations is then derived, already in discrete form, by differentiating and rearranging the augmented objective function. The adjoint variables are finally computed by numerically solving the system of discrete adjoint equations.

1.2.1 Shape Optimization

The goal of ShpO is to find a shape that minimizes or maximizes a certain performance measure (objective function, J) while satisfying the given constraints. The shape of the geometric form under consideration is controlled by a number of variables, for instance, the coefficients of the Bézier-Bernstein polynomials. In such case, those act as the design variables of the optimization problem. The mapping from the design variables to the geometry is called shape parameterization.

This thesis deals with the analysis of problems involving heat transfer between fluids and solids, known as CHT analysis. Such problems appear in various applications including turbine cooling systems [22–24], cooling of electronics [25] and heat sinks [26]. ShpO has been utilized in CHT problems both using stochastic methods [27] and GBMs [28, 29]. For the latter, an adjoint method can be used for the computation of the SDs.

Adjoint methods have been developed for ShpO in CHT problems, [28, 30, 31]. In [31], the formulation of the adjoint equations governing both the fluid and the solid domains along with the Adjoint Boundary Conditions (ABCs) in the FSI was presented using the continuous adjoint method. Contrary to [31], in [28] the continuous adjoint method for CHT ShpO was presented taking the

effect of the turbulence model into account, in the computation of the SDs.

1.2.2   Topology Optimization

The concept of TopO was first introduced in the field of structural mechanics by Bendsøe and Kikuchi, [32]. There, the aim was to determine the optimal distribution of material within a design space rather than just modifying the shape of a structure to optimize it. Nodes of the discretized domain to be assigned with unary material density values were sought, in areas of the structure where material should be added to improve its structural stiffness under specific loads, while the rest were assigned with zero values indicating the absence of material.

A few years later, the same idea migrated to fluid dynamics for problems governed by the Stokes equations, [33]. TopO in fluids was accomplished by incorporating a porosity-dependent term into the flow equations. The flow encounters great resistance in areas of high porosity values meaning that its velocity becomes practically zero. Hence, those areas correspond to the solidified part of the domain while areas of zero porosity value belong to the flow since there is no porosity-induced resistance. To minimize an objective function, TopO aims to determine the ideal porosity value at each cell. This means that the number of design variables is equal to the number of mesh cells, and therefore, the adjoint method is the most suitable approach to compute the sensitivities of the objective function w.r.t. the porosity values. Finally, it gives the ability to design unconventional shapes and is particularly useful in the preliminary design of ducts or duct systems when only the inlet and outlet of the duct are known. On the other hand, while the absence of parameterization is considered one of the advantages of TopO, the formed geometry, i.e. the interface between the solidified and fluid parts of the domain, needs post-processing to be extracted.

Following [33], the concept of TopO was extended to laminar flows by Gersborg-Hansen et al., [34] and Olesen et al., [35]. Regarding turbulent flows, the adjoint equations and BCs were derived using the continuous adjoint method in [36] with the omission though of the eddy viscosity variation. Later on, an exact continuous adjoint formulation for TopO problems of 2D incompressible turbulent flows was presented in [37] and was extended to 3D flows in [38].

1.3   Thesis Outline

This thesis consists of six chapters, including the Introduction, which are summarized below.

In Chapter 2, the primal and adjoint equations for CHT ShpO problems with laminar steady-state flows of incompressible fluids are presented. The equations that govern the system are the steady-state NS equations, which are combined with the energy equation for the fluid domain, as well as the steady-state heat conduction equation for solids.

In Chapter 3, the primal and adjoint equations for CHT TopO problems are presented.

In Chapter 4, CHT analysis is conducted on a 2D test case. This case studies a cooling duct the geometry of which was inspired by the serpentine passages found in internally cooled turbine blades. At first, the primal problem is solved using the publicly available OpenFOAM©solver. Then, the ShpO of the duct is performed using the solver developed by the PCOpt/NTUA, after comparing its results with those from the previous solver.

In Chapter 5, the primal problem discussed in Chapter 4 is solved again using a porosity-based approach this time. An OpenFOAM©utility is used to initialize the porosity field so that the cells corresponding to the solid domain, are given a porosity value of 1 while the others are 0. Then, a study is conducted for the β_{max} parameter and the effects of the omission of the BCs on the FSI are quantified. Finally, several TopO runs are carried out for different weights in the objective function. In section 5.3, a new fully-structured mesh is generated consisting of cells of uniform size which is typical for TopO, since the geometry is unknown. A mesh independence study is conducted to determine the appropriate cell density of the mesh. Then, the TopO of the 2D internally cooled turbine blade-like geometry is performed, starting from all-fluid domain, for several weights in the objective function. The resulting geometries correspond to a U-shaped duct like the ones formed in section 5.2. In section 5.4, a U-shaped duct is designed, similar to the ones produced in sections 5.2 and 5.3, to evaluate the TopO results. Finally, ShpO of the U-shaped duct is carried out for differently weighted objective functions.

In Chapter 6, the assumptions drawn in previous chapters are revisited on a second test case regarding the design of a 2D duct system. At first, TopO cases are run the results of which are discussed. Then, using a utility developed by the PCOpt/NTUA, body-fitted meshes are generated for both the fluid and solid regions based on the background mesh of TopO and the optimized porosity field. Finally, the primal problem is solved on the body-fitted mesh to compare the results with those of TopO and several ShpO cases are performed.

Chapter 2

Continuous Adjoint Method for CHT ShpO

In this chapter, the flow and adjoint equations for CHT ShpO problems with laminar flows of incompressible fluids are presented. The adjoint equations are derived by applying the continuous adjoint method [18] to the steady-state Navier-Stokes equations. The adjoint PDEs used in this thesis are the ones proposed in [39].

2.1 The Primal Problem

In CHT problems, the computational domain is composed of the fluid domains Ω^F and the solid domains Ω^S separated by an interface $\overline{S}$. Depending on whether the interface is seen from the fluid or solid point of view, the latter will be denoted by $\overline{S}^F$ or $\overline{S}^S$ respectively. For the fluid domains, the governing equations are the steady-state Navier-Stokes for incompressible flows solved along with the energy equation [40] while for the solid domains, the steady-state heat conduction equation is solved.

2.1.1 State Equations

Every quantity pertaining to the fluid domain is marked with the superscript F whereas the S superscript is used for the solid domain. The fluid flow PDEs for the CHT problem are written as

$$R^p = -\frac{\partial v_j}{\partial x_j} = 0 \tag{2.1a}$$

$$R_i^v = v_j \frac{\partial v_i}{\partial x_j} - \frac{\partial \tau_{ij}}{\partial x_j} + \frac{\partial p}{\partial x_i} = 0, \qquad i = 1, 2, (, 3) \tag{2.1b}$$

$$R^{T^F} = \rho^F v_j c_p \frac{\partial T^F}{\partial x_j} + \rho^F \frac{v_j}{2} \frac{\partial v_k^2}{\partial x_j} - \frac{\partial}{\partial x_j}\left(k^F \frac{\partial T^F}{\partial x_j}\right) = 0 \tag{2.1c}$$

which correspond to the continuity, momentum and energy equations respectively. In the energy equation, the viscous energy dissipation term is omitted. Since the flow is incompressible, the energy equation does not give feedback

to the NS PDEs thus; thus, it can be solved after the latter have converged. These equations are solved using the SIMPLE algorithm [41]. In the above equations, p, v_i, τ_{ij} are the static pressure divided by the constant fluid density, velocity and stress components ($\tau_{ij} = \nu \left(\frac{\partial v_i}{\partial x_j} + \frac{\partial v_j}{\partial x_i} \right)$ where ν stands for the kinematic viscosity). In addition, ρ^F is the constant fluid density, c_p is the specific heat transfer coefficient under constant pressure and k^F is the fluid thermal conductivity, for which

$$k^F = \rho^F c_p \alpha = \rho^F c_p \left(\frac{\nu}{Pr} \right) \tag{2.2}$$

where *Pr* is the Prandtl number and α is the thermal diffusivity. The thermal diffusivity α is defined as $\alpha = \nu / Pr$.

On the other hand, heat conduction over solid region Ω^S is governed by,

$$R^{T^S} = -\frac{\partial}{\partial x_j} \left(k^S \frac{\partial T^S}{\partial x_j} \right) = 0 \tag{2.3}$$

where k^S stands for the thermal conductivity of the solid region.

2.1.2 Boundary Conditions

The conditions imposed on each type boundary type are presented. The boundaries S^F of Ω^F are decomposed as $S^F = S_I^F \cup S_O^F \cup S_W^F \cup \overline{S}^F$, indicating the inlet, outlet, plain and FSI walls, respectively. The solid domain boundaries S^S are decomposed as $S^S = S_D^S \cup S_{Fl}^S \cup \overline{S}^S$, where S_D^S and S_{Fl}^S have fixed temperature and fixed heat-flux distributions (adiabatic or non-adiabatic), respectively.

Inlet Boundaries, S_I^F

At the inlet, a uniform velocity and temperature distribution is imposed. Additionally, zero Neumann conditions are imposed on pressure.

Outlet Boundaries, S_O^F

At the outlet, zero Neumann conditions are imposed on velocity and temperature with the assumption that the flow has settled near the exit. On pressure, zero Dirichlet condition is set and so the manometric pressure is calculated in the domain.

Fluid Wall Boundaries, S_W^F

All the velocity components take on zero value on the wall boundaries since the flow under consideration is viscous. Additionally, $\partial p / \partial n = 0$. The walls that belong to the Ω^F domain are considered adiabatic, so $\partial T / \partial n = 0$.

Solid Wall Boundaries, (S_D^S, S_{Fl}^S)

Fixed temperature boundary conditions are imposed on S_D^S. Along S_{Fl}^S, zero Neumann conditions are imposed which means that all these boundaries are considered adiabatic.

FSI Boundaries $(\overline{S}^F, \overline{S}^S)$

The conditions imposed on velocity and pressure at $\overline{S}^F$ are the same as the ones used for the wall boundaries S_W^F. The only difference is in the temperature boundary conditions. The conditions imposed on temperature along each point at the FSI boundary $(\overline{S}^F, \overline{S}^S)$ are

$$T^S\big|_{\overline{S}^S} = T^F\big|_{\overline{S}^F} \tag{2.4}$$

$$k^S \frac{\partial T^S}{\partial n}\bigg|_{\overline{S}^S} = -k^F \frac{\partial T^F}{\partial n}\bigg|_{\overline{S}^F} \tag{2.5}$$

where n is the outward unit normal vector and, thus, $n_i\big|_{\overline{S}^F}$=-$n_i\big|_{\overline{S}^S}$. If the heat flows from the solid region to the fluid, the left-hand side in eq. (2.5) is positive because it follows the direction of the solid outward normal $n_i\big|_{\overline{S}^S}$. Observing the heat flow from the fluid perspective, the opposite is true and thus, a negative sign is added in eq. (2.5) to ensure heat-flux conservation. The first condition eq. (2.4) is there to ensure temperature equality on the interface of the two regions.

2.2   The Adjoint Problem

In gradient-based optimization, the gradient of the objective function w.r.t. the design variables, also called SDs, should be computed in order to update their value. The continuous adjoint is an efficient method for the computation of the exact derivatives of objective functions.

2.2.1   Introduction of the Adjoint Variables

Starting point for the formulation of the adjoint problem is the introduction of the augmented objective function, J_{aug}, which is defined by adding the volume integrals of the state equations (eqs. (2.1)), multiplied by the adjoint variables, to the objective function J, namely,

$$J_{aug} = J + \int_{\Omega^F} qR^p d\Omega + \int_{\Omega^F} u_i R_i^v d\Omega + \sum_{D=F,S} \int_{\Omega^D} T_a^D R^{T^D} d\Omega \tag{2.6}$$

where q, u_i are the adjoint to the pressure and velocity fields. Additionally, T_a^D stands for the adjoint temperature with $D = F$ for the fluid and $D = S$ for the solid domains. Since the residuals of the primal equations are zero, the value of J_{aug} is identical to that of J. Differentiating J_{aug}, which is as if J is differentiated, w.r.t. the design variables b_n, yields

$$\frac{\delta J_{aug}}{\delta b_n} = \frac{\delta J}{\delta b_n} + \frac{\delta}{\delta b_n} \int_{\Omega^F} qR^p d\Omega + \frac{\delta}{\delta b_n} \int_{\Omega^F} u_i R_i^v d\Omega + \sum_{D=F,S} \frac{\delta}{\delta b_n} \int_{\Omega^D} T_a^D R^{T^D} d\Omega \tag{2.7}$$

Introducing additional degrees of freedom in eq. (2.6), in the form of the adjoint variables, gives the ability to get rid of the terms multiplying the derivatives of

the primal variables in $\delta J_{aug}/\delta b_n$ which are computationally expensive. After some lengthy mathematical development of eq. (2.7) shown in [38, 42] the field adjoint equations as well as the ABCs arise by setting the aforementioned terms to zero.

2.2.2 Objective Function Definition

Before proceeding with the presentation of the adjoint problem, the objective function should be defined as it contributes to the field adjoint equations and their BCs as well as to the SDs. In this thesis, the objective function used combines two separate objectives; the first one is to maximize the surface-averaged temperature at the outlet and the other is to minimize the volume-averaged total pressure losses. The total objective function to be minimized is written as,

$$J^{total} = -w\hat{J}^{meanT} + (1-w)\hat{J}^{p_t} \tag{2.8}$$

where $w \in [0,1]$ is a weight used to control the contribution of each objective in the total objective function. The negative sign in eq. (2.8) appears because the maximization of J^{meanT} objective is sought. The hat symbol is used as an indication that the two objectives are separately normalized. The normalization is made by dividing each objective by its value computed as $\hat{J} = J/J_0$ where the denominator corresponds to the starting geometry.

The surface-averaged temperature objective is computed by

$$J^{meanT} = \frac{\int_{S_O} T^F dS}{\int_{S_O} dS} = \frac{1}{S_O} \int_{S_O} T^F dS \tag{2.9}$$

while the volume-averaged total pressure losses objective function is written as

$$J^{p_t} = -\int_{S_{I,O}} \left(p + \frac{1}{2}v_k^2\right) v_i n_i dS \tag{2.10}$$

The contribution of each objective in the adjoint equations and BCs is determined by differentiating it w.r.t. the design variables b_n. For the mean outlet temperature objective this yields

$$\frac{\delta\hat{J}^{meanT}}{\delta b_n} = \frac{1}{J_0^{meanT}} \frac{1}{S_O} \int_{S_O} \frac{\delta T^F}{\delta b_n} dS \tag{2.11}$$

and for the volume-averaged total pressure losses,

$$\frac{\delta\hat{J}^{p_t}}{\delta b_n} = -\frac{1}{J_0^{p_t}} \int_{S_{I,O}} v_i n_i \frac{\delta p}{\delta b_n} dS - \frac{1}{J_0^{p_t}} \int_{S_{I,O}} \left[v_i v_j n_j + \left(p + \frac{1}{2}v_j^2\right) n_i\right] \frac{\delta v_i}{\delta b_n} dS \tag{2.12}$$

Based on the development in [42], the two objectives only contribute to the ABCs and the SDs. Those contributions will be presented in detail later on.

2.2.3 Field Adjoint Equations

The Field Adjoint Equations (FAE) for CHT ShpO problems are derived in [42] for a general objective function. For the fluid domain Ω^F, the adjoint PDEs are

$$R^q = -\frac{\partial u_j}{\partial x_j} = 0 \tag{2.13a}$$

$$R_i^u = u_j \frac{\partial v_j}{\partial x_i} - v_j \frac{\partial u_i}{\partial x_j} - \frac{\partial \tau_{ij}^a}{\partial x_j} + \frac{\partial q}{\partial x_i} + \rho^F c_p T_a^F \frac{\partial T^F}{\partial x_i} + \rho^F T_a^F v_k \frac{\partial v_k}{\partial x_i}$$
$$- \rho^F v_i v_k \frac{\partial T_a^F}{\partial x_k} = 0, \quad i = 1, 2, (, 3) \tag{2.13b}$$

$$R_F^{T_a} = -\rho^F c_p v_j \frac{\partial T_a^F}{\partial x_j} - \frac{\partial}{\partial x_j} \left(k^F \frac{\partial T_a^F}{\partial x_j} \right) = 0 \tag{2.13c}$$

$$\tag{2.13d}$$

where R^q, R_i^u and $R_F^{T_a}$ are the adjoint continuity, momentum and energy PDEs. The adjoint stress tensor τ_{ij}^a is given by $\tau_{ij}^a = \nu \left(\frac{\partial u_i}{\partial x_j} + \frac{\partial u_j}{\partial x_i} \right)$. Equations (2.13a)–(2.13c) are solved by the SIMPLE algorithm [41], i.e. the same algorithm used to solve the primal PDEs, eqs. (2.1a)–(2.1c).

The adjoint heat conduction PDE solved over the solid region Ω^S, is written as

$$R_S^{T_a} = -\frac{\partial}{\partial x_j} \left(k^S \frac{\partial T_a^S}{\partial x_j} \right) = 0 \tag{2.14}$$

Since eq. (2.13c) and eq. (2.14) do not involve any adjoint variable other than T_a^F and T_a^S, they can be solved prior to solving the rest of the adjoint PDEs.

2.2.4 Adjoint Boundary Conditions

Inlet Boundaries, S_I^F

The ABCs are presented for the fluid region Ω^F at first. Along the inlet boundaries S_I^F, the conditions imposed for a general objective function are, [42]

$$u_j n_j = u_{\langle n \rangle} = (1-w) \frac{1}{J_0^{p_t}} v_i n_i \tag{2.15a}$$

$$u_{\langle t \rangle}^I = 0 \tag{2.15b}$$

$$u_{\langle t \rangle}^{II} = 0 \tag{2.15c}$$

where t_i^I, t_i^{II} are the components of the tangent to the surface unit vectors. Also, $\partial q / \partial n = 0$ and $T_a^F = 0$.

Outlet Boundaries, S_O^F

Along the outlet boundary S_O^F, the boundary conditions for u_i and q are, [42]

$$q = u_{\langle n \rangle} v_{\langle n \rangle} + 2\nu \frac{\partial u_{\langle n \rangle}}{\partial n} - (1-w) \frac{1}{J_0^{p_t}} \left[v_i v_k + \left(p + \frac{1}{2} v_j^2 \right) \delta_{ik} \right] n_k n_i + \rho^F T_a^F v_{\langle n \rangle}^2 = 0 \tag{2.16}$$

Regarding the normal component of the adjoint velocity, the condition $\partial u_{\langle n \rangle}/\partial n = 0$ is imposed and the tangential adjoint velocity components ($l = I$, II in 3D; only $l = I$ in 2D) are given by

$$v_{\langle n \rangle} u_{\langle t \rangle}^l + \nu \left(\frac{\partial u_{\langle t \rangle}^l}{\partial n} + \frac{\partial u_{\langle n \rangle}}{\partial t^l} \right) - (1-w)\frac{1}{J_0^{p_t}} \left[v_i v_k + \left(p + \frac{1}{2}v_j^2 \right) \delta_{ik} \right] n_k t_i^l$$
$$+ \rho^F T_a^F v_{\langle n \rangle} v_{\langle t \rangle}^l = 0 \tag{2.17}$$

The following BC is used for T_a^F along S_O^F

$$\rho^F c_p T_a^F v_j n_j + k^F \frac{\partial T_a^F}{\partial n} - w \frac{1}{J_0^{meanT}} \frac{1}{S_O} n_i = 0 \tag{2.18}$$

Fluid Wall Boundaries, S_W^F

Along S_W^F, the BCs for the adjoint velocity components are the same as the ones imposed on the inlet boundary S_I^F eq. (2.15). The objective function used in this thesis (section 2.2.2), is not defined on any wall boundary and thus, it does not contribute to the ABCs imposed on S_W^F. Therefore, the adjoint velocity on S_W^F is given as, [42],

$$u_{\langle n \rangle} = u_{\langle t \rangle}^I = u_{\langle t \rangle}^{II} = 0 \tag{2.19}$$

Additionally, $\partial q/\partial n = 0$. Considering that on the fluid domain walls, zero Neumann conditions are imposed on temperature, the condition imposed on the adjoint temperature based on [42] reads

$$\left. \frac{\partial T_a^F}{\partial n} \right|_{S_W^F} = 0 \tag{2.20}$$

Solid Wall Boundaries, (S_D^S, S_{Fl}^S)

Along the boundaries S_D^S with fixed temperature value, the condition imposed for the adjoint temperature T_a^S is

$$T_a^S = 0 \tag{2.21}$$

whereas for the adiabatic boundaries S_{Fl}^S, the following condition is imposed

$$\left. \frac{\partial T_a^S}{\partial n} \right|_{S_{Fl}^S} = 0 \tag{2.22}$$

FSI Boundaries $(\overline{S}^F, \overline{S}^S)$

The conditions imposed on u_i, q along the FSI boundary $\overline{S}^F$, are identical with the ones imposed on S_W^F. The only difference is in the adjoint temperature

T_a^F BC. Conditions imposed along the FSI boundary ($\overline{S}^F$, $\overline{S}^S$) on the adjoint temperature T_a are, [42],

$$-T_a^F\Big|_{\overline{S}^F} = -T_a^S\Big|_{\overline{S}^S} \tag{2.23a}$$

$$k^F \frac{\partial T_a^F}{\partial n}\Big|_{\overline{S}^F} = -k^S \frac{\partial T_a^S}{\partial n}\Big|_{\overline{S}^S} \tag{2.23b}$$

where $\boldsymbol{n}$ is the outward unit normal vector and, thus, $n_i|_{\overline{S}^F}$=-$n_i|_{\overline{S}^S}$. The objective function used in this thesis is only defined on the inlet and outlet boundaries. Therefore, all the objective function contributions in eqs. (2.23) are equal to zero.

2.2.5 Sensitivity Derivatives

After satisfying the FAE and their BC, the SDs are computed by the following expression developed in [42]

$$\frac{\delta J}{\delta b_n} = \int_{\Omega^F} \left[-u_i v_j \frac{\partial v_i}{\partial x_k} - u_j \frac{\partial p}{\partial x_k} - \tau_{ij}^a \frac{\partial v_i}{\partial x_k} + u_i \frac{\partial \tau_{ij}}{\partial x_k} + q \frac{\partial v_j}{\partial x_k} - \rho^F c_p T_a^F v_j \frac{\partial T^F}{\partial x_k} \right.$$
$$\left. - \rho^F T_a^F v_i v_j T_a^F \frac{\partial v_i}{\partial x_k} - k^F \frac{\partial T_a^F}{\partial x_j} \frac{\partial T^F}{\partial x_k} + T_a^F \frac{\partial}{\partial x_k} \left(k^F \frac{\partial T^F}{\partial x_j} \right) \right] \frac{\partial}{\partial x_j} \left(\frac{\delta x_k}{\delta b_n} \right) d\Omega \quad (2.24)$$
$$+ \int_{\Omega^S} \left[-k^S \frac{\partial T_a^S}{\partial x_j} \frac{\partial T^S}{\partial x_k} + T_a^S \frac{\partial}{\partial x_k} \left(k^S \frac{\partial T^S}{\partial x_j} \right) \right] \frac{\partial}{\partial x_j} \left(\frac{\delta x_k}{\delta b_n} \right) d\Omega$$

Field Integrals are present in the expression of the SDs eq. (2.24), which is the reason this adjoint formulation is abbreviated as the Field Integral (FI) adjoint. More adjoint formulations regarding ShpO are developed and examined in [43].

Chapter 3

Continuous Adjoint Method for CHT TopO

In porosity-based TopO, the value-field of design variables α ("porosity" field) is used to solidify the part of the design domain that is counter-productive w.r.t. the objective function J to be minimized. Parts of the computational domain with zero porosity values, or practically $\alpha \leq \epsilon$, where ϵ is a user-defined infinitesimally small positive number, correspond to the fluid part of the domain. All the remaining areas where $\alpha \neq 0$, or practically $\alpha > \epsilon$, define the part of the domain to be solidified. In fig. 3.1 the concept of TopO in fluid mechanics is illustrated.
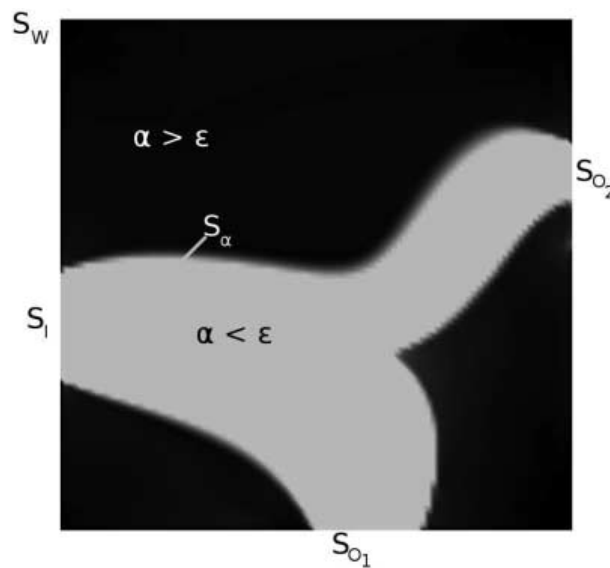
Figure 3.1: Schematic representation of a porous media (Ω) domain and its boundaries. S_I is the inlet (or inlets, if more than one), S_{Ol}, $l = 1, L$ are the outlets and S_W are the solid wall boundaries along the domain, all predefined. White areas correspond to the flow domain ($\alpha \leq \epsilon$), while black color indicates solidified areas ($\alpha > \epsilon$). From [37].

Given that in TopO, the number of design variables is equal to the number of mesh cells, the adjoint method is the perfect choice for computing the sensitivity derivatives $\delta J/\delta \alpha$ since its cost is independent of the number of design variables.

A known problem in the porosity-based approach of TopO is that "grey" areas usually emerge, that do not belong to either the fluid or solid domain and thus, a user-defined criterion must be applied to track the boundary between the two. To reduce the formation of "grey" areas in the domain, projection methods that drive the resulting porosity field towards a more binary state are employed. An alternative approach for TopO dealing with this problem is based on the level-set method in which the boundaries between the flow and solidified areas are clearly marked. This diploma thesis deals only with the porosity-based approach but level-set methods have also been attracting attention during the last few years [44, 45].

3.1 The Primal problem

In all the TopO cases studied in this diploma thesis, the flow is governed by the steady-state Navier-Stokes equations along with the energy equation. In porosity-based TopO, to simulate the solidification of parts of the domain, the flow equations are augmented with α-dependent source terms, whose role is to deactivate the flow equations over the solid and apply solid wall conditions.

3.1.1 State Equations

The so-modified flow equations along with the energy equation for steady flows of incompressible fluids read, [37],

$$R^p = -\frac{\partial v_j}{\partial x_j} = 0 \tag{3.1a}$$

$$R_i^v = v_j \frac{\partial v_i}{\partial x_j} - \frac{\partial \tau_{ij}}{\partial x_j} + \frac{\partial p}{\partial x_i} + \beta_{max} I^v(\beta) v_i = 0, \qquad i = 1, 2, (, 3) \tag{3.1b}$$

$$R^T = (1-\beta)\rho(I^\rho(\beta))c_p(I^{c_p}(\beta))v_j \frac{\partial T}{\partial x_j} - \frac{\partial}{\partial x_j}\left(k(I^k(\beta))\frac{\partial T}{\partial x_j}\right) = 0 \tag{3.1c}$$

where $\beta \in [0,1]$ is a field that emerges from the porosity field α after the regularization and projection steps are performed. The I^v, I^ρ, I^{c_p}, I^k functions, are used to either drive the flow solution towards values corresponding to solid walls (eq. (3.1b)) or to interpolate between the thermo-physical properties of the fluid and solidified domains (eqs. (3.1)). Also, $\rho(I^\rho(\beta))$, $c_p(I^{c_p}(\beta))$, $k(I^k(\beta))$, denote the interpolated values of those quantities between the fluid and the solid. In eqs. (3.1), the convection term is multiplied with $(1-\beta)$ to cancel out its contribution in areas where small leakage of fluid into the solid domain is observed in TopO. For the porosity-related source terms of the form $\beta_{max} I^\Phi(\beta)\Phi$, a linear function is used defined as

$$I^\Phi(\beta) = \beta \tag{3.2}$$

The interpolation of thermophysical properties is based on the following scheme

$$\Phi(\beta) = (1 - I^\Phi(\beta))\Phi^F + I^\Phi(\beta)\Phi^S \tag{3.3}$$

where the superscripts F and S denote the value of the quantity Φ in the fluid and solid domain respectively. For the interpolation, the Solid Isotropic Material Penalization (SIMP) function [32] is used namely

$$I^\Phi(\beta) = \beta^b \tag{3.4}$$

with constant value of $b = 3$ for all the cases studied in this diploma thesis.

The β_{max} value is used to ensure that the v_i values are practically zero in the solidified domain. Its value can be computed based on the Darcy number, quantifying the ratio between viscous and porous forces, [35],

$$Da = \frac{\nu}{\beta_{max}L^2} \Rightarrow \beta_{max} = \frac{\nu}{DaL^2} \tag{3.5}$$

where L is the characteristic length of the case under consideration, which is either the inlet length or the inlet hydraulic diameter for 2D and 3D cases, respectively. Based on [35], for $Da = 10^{-5}$ the solidified area obtained from the TopO is practically impermeable.

Often, in TopO problems, especially those dealing with CHT, the design may result in checkerboards. Checkerboards refer to designs with alternating solid and fluid cells ordered in checkerboard-like patterns. This can be avoided by using filtering schemes applied to the porosity field α. The regularization of α is implemented based on a Helmholtz-type filter [46], transforming α to $\tilde{\alpha}$,

$$R^F(\tilde{\alpha}, \alpha) = -\left(\frac{R}{2\sqrt{3}}\right)^2 \frac{\partial^2 \tilde{\alpha}}{\partial x_j^2} + \tilde{\alpha} - \alpha = 0 \tag{3.6}$$

where $\tilde{\alpha}$ is the regulated porosity field and R can be seen as a smoothing radius, usually computed as a function of the average mesh cell size. For the solution of the Helmholtz PDE, zero Neumann BCs are imposed. The regularization of the porosity field blurs changes between the fluid and solidified domains and, thus, a projection step is required, to increase the contrast of the $\tilde{\alpha}$ field producing the β field as,

$$\beta = \frac{\tanh(\eta b) + \tanh[b(\tilde{\alpha} - \eta)]}{\tanh(\eta b) + \tanh[b(1 - \eta)]} \tag{3.7}$$

with $\eta = 0.5$ and b being a sharpening parameter (irrelevant to the one found in eq. (3.4)). The value of b varies throughout the optimization and may differently be defined for each optimization case.

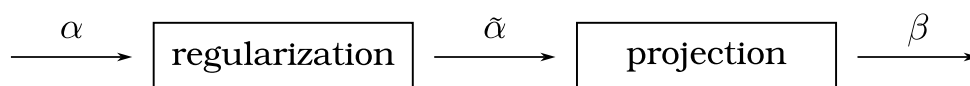The processing steps of the porosity field α are summarized in fig. 3.2.

Figure 3.2: Porosity field processing steps.

Firstly, the regularization step is used to eliminate possible checkerboards by transforming the α field to a smoother field $\tilde{\alpha}$ and, then, the projection step transforms $\tilde{\alpha}$ to the β field which gives a more binary representation of the interface between fluid and solid areas.

3.1.2 Boundary Conditions

The conditions imposed on various quantities along the boundaries of the domain are identical to the ones presented in section 2.1.2.

3.2 The Adjoint Problem

3.2.1 Augmented Objective Function

Again, the first step for the formulation of the adjoint problem with the continuous adjoint method is the definition of the augmented objective function (Lagrangian) J_{aug}. This is defined for TopO problems as

$$J_{aug} = J + \int_\Omega qR^p d\Omega + \int_\Omega u_i R_i^v d\Omega + \int_\Omega T_a R^T d\Omega \tag{3.8}$$

where R^p, R_i^v, R^T are the residuals of eqs. (3.1). When the primal equations are converged, the residuals are practically zero meaning that $J_{aug} = J$. Additionally, q, u_i, T_a are the adjoint to the pressure, velocity, and temperature fields.

In porosity-based TopO, the objective function gradient w.r.t. the porosity field should be computed. Since $J_{aug} = J$, the SDs can be computed by differentiating the augmented objective instead of J, which yields

$$\frac{\delta J_{aug}}{\delta a_m} = \frac{\delta J}{\delta a_m} + \int_\Omega q\frac{\delta R^p}{\delta a_m}d\Omega + \int_\Omega u_i\frac{\delta R_i^v}{\delta a_m}d\Omega + \int_\Omega T_a\frac{\delta R^T}{\delta a_m}d\Omega \tag{3.9}$$

The adjoint equations and BCs arise from eq. (3.9) after the terms multiplying the derivatives of primal variables are set to zero. The development of eq. (3.9) and the formulation of the adjoint problem is presented in detail in [37]. By eliminating the aforementioned terms, an expression of the objective sensitivities independent of the derivatives of primal variables emerges. Therefore, the cost of the SDs is independent of the number of design variables; only the primal and the adjoint problem solutions are needed to compute them.

3.2.2 Field Adjoint Equations

Following the mathematical development outlined in [47], the continuous adjoint PDEs to eqs. (3.1) can be derived and written as,

$$R^q = -\frac{\partial u_j}{\partial x_j} = 0 \tag{3.10a}$$

$$R_i^u = u_j\frac{\partial v_j}{\partial x_i} - v_j\frac{\partial u_i}{\partial x_j} - \frac{\partial \tau_{ij}^a}{\partial x_j} + \frac{\partial q}{\partial x_i} + \rho(I^\rho(\beta))c_p(I^{c_p}(\beta))(1-\beta)T_a\frac{\partial T}{\partial x_i} \tag{3.10b}$$

$$+ \beta_{max}I^v(\beta)u_i = 0, \quad i = 1,2,(,3)$$

$$R^{T_a} = -\rho(I^\rho(\beta))c_p(I^{c_p}(\beta))v_j\frac{\partial}{\partial x_j}[(1-\beta)T_a] - \frac{\partial}{\partial x_j}\left(k(I^k(\beta))\frac{\partial T_a}{\partial x_j}\right) = 0 \tag{3.10c}$$

The objective function used in this thesis (section 2.2.2), does not contribute to the adjoint equations and only contributes to the ABCs, same as for ShpO. The presence of the porosity-dependent term in eq. (3.10b) indicates that u_i will practically take on zero values in the solidified parts of the domain.

3.2.3 Adjoint Boundary Conditions

The ABCs of the TopO problem are identical to those presented in section 2.2.3, for ShpO problems. The reason for this is that the primal equations of the TopO problem differ from those used in ShpO only due to the presence of the additional porosity-dependent source terms. Since none of these terms contains a differential operator, the Gauss divergence theorem is not employed on those during the formulation of the adjoint, and thus, no additional surface integrals that contribute to the ABCs are produced.

3.2.4 Sensitivity Derivatives

After solving the primal and adjoint PDEs, the SDs of the objective function J w.r.t. the α field can be computed as

$$\frac{\delta J}{\delta a_m} = \int_\Omega \Theta_{\tilde{\alpha}} \frac{\partial \tilde{\alpha}}{\partial a_m} d\Omega \tag{3.11}$$

where

$$\begin{aligned}
\Theta_{\tilde{\alpha}} = {} & \left(\beta_{max} v_i u_i \frac{\partial I^v}{\partial \beta} - \rho c_p T_a v_j \frac{\partial T}{\partial x_j} \right) \frac{\partial \beta}{\partial \tilde{\alpha}} + \left[\frac{\partial}{\partial x_j} \left(T_a \frac{\partial T}{\partial x_j} \right) - T_a \frac{\partial^2 T}{\partial x_j^2} \right] \frac{\partial k}{\partial \beta} \frac{\partial \beta}{\partial \tilde{\alpha}} \\
& + (1 - \beta) T_a v_j \frac{\partial T}{\partial x_j} \left(c_p \frac{\partial \rho}{\partial \beta} + \rho \frac{\partial c_p}{\partial \beta} \right) \frac{\partial \beta}{\partial \tilde{\alpha}}
\end{aligned} \tag{3.12}$$

In eq. (3.12), $\partial \beta / \partial \tilde{\alpha}$ is computed analytically by differentiating the tanh function eq. (3.7) which yields

$$\frac{\partial \beta}{\partial \tilde{\alpha}} = \frac{b \operatorname{sech}^2 [b(\tilde{\alpha} - \eta)]}{\tanh(\eta b) + \tanh[b(1 - \eta)]} \tag{3.13}$$

On the other hand, the computation of $\partial \tilde{\alpha} / \partial \alpha$ is a costly process that can be avoided through the solution of the adjoint equation. Consequently, a new term is added to the augmented objective eq. (3.8) which reads

$$\frac{\delta J}{\delta a_m} = \int_\Omega \Theta_{\tilde{\alpha}} \frac{\partial \tilde{\alpha}}{\partial a_m} d\Omega - \int_\Omega \Psi_{\tilde{\alpha}} \frac{\partial R^F(\tilde{\alpha}, \alpha)}{\partial a_m} d\Omega \tag{3.14}$$

where $R^F(\tilde{\alpha}, \alpha)$ is the Helmholtz filtering PDE residual (eq. (3.6)) and $\Psi_{\tilde{\alpha}}$ is an additional adjoint variable. After some mathematical development of eq. (3.14) and by setting the terms multiplying $\partial \tilde{\alpha} / \partial a_m$ equal to zero, the adjoint to the Helmholtz filtering PDE arises in the following form

$$R^{\Psi_{\tilde{\alpha}}} = - \left(\frac{R}{2\sqrt{3}} \right)^2 \frac{\partial^2 \Psi_{\tilde{\alpha}}}{\partial x_j^2} + \Psi_{\tilde{\alpha}} - \Theta_{\tilde{\alpha}} = 0 \tag{3.15}$$

and, finally, the SDs are given by

$$\frac{\delta J}{\delta \alpha_m} = \Psi_{\tilde{\alpha}}^m \Omega^m \qquad (3.16)$$

where Ω^m is the volume of the m-th cell; repeated superscripts on the right hand side (r.h.s.) of eq. (3.16) do not imply summation. In case regularization is omitted, $\delta J / \delta \alpha$ is given directly by eq. (3.11)

Chapter 4

CHT Analysis on Body-Fitted Meshes

In this chapter, the results of the of a cooling duct are presented. The duct geometry is inspired by the serpentine passages found in internally cooled turbine blades. Only the flow inside the blade is computed and, thus, the analysis is monofluid. In section 4.1, details regarding the general formulation of the problem are discussed. At first, the problem is solved using the compressible solver for steady fluid flow and solid heat conduction, with CHT between regions, publicly available with OpenFOAM©[48]. The same problem is then solved with the incompressible CHT solver developed by the PCOpt/NTUA since this is the one to be used in the optimization i.e. the one for which the adjoint method and software has been developed.

4.1   Problem Description

The geometry studied in this thesis corresponds to a simplified 2D turbine blade with an internal cooling duct. The duct geometry used in this chapter is arbitrarily designed to achieve effective transfer of heat from the solid domain to the fluid, inspired by the flow path found in an internally cooled turbine blade. The geometry and its dimensions are presented in fig. 4.1. The domain is composed of three regions, the fluid region (Ω^F) and two solid regions (Ω^S), referred to as Solid1 and Solid2.
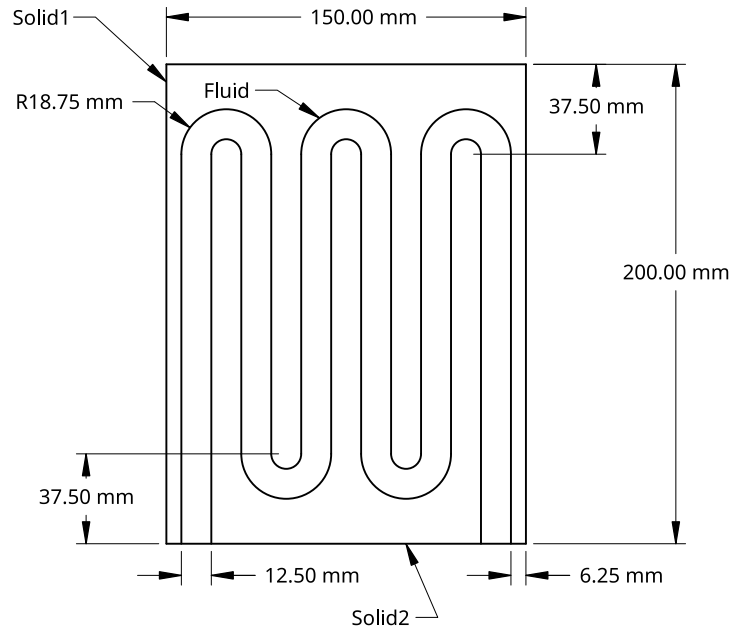
Figure 4.1: 2D geometry & dimensions of the serpentine-shaped duct used in the analysis.

The mesh is presented in fig. 4.2 and is fitted to the body's geometry. To distinguish this mesh from the others that are used later, it will be referred to as BFM1 (Body-Fitted Mesh).
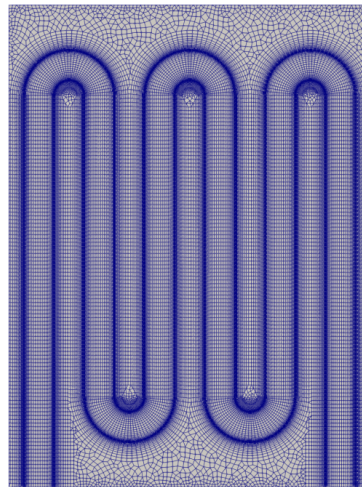
Figure 4.2: Initial Body-fitted mesh used for the CHT analysis (BFM1).

In the Fluid region, the mesh generated is structured, consisting of $\sim 32K$ cells. For the solid regions, an unstructured mesh is used, with structured layers along the FSI. For both the Solid1 and Solid2 regions, the mesh consists of $\sim 18K$ cells. The fluid flow is laminar with inlet velocity equal to $0.5\,\mathrm{m/s}$ and $Re = 417$ based on the duct hydraulic diameter. Additionally, the fluid enters the domain at a temperature of $T = 373\,\mathrm{K}$. Along the non-FSI walls of Ω^S, a Dirichlet temperature condition ($T = 873\,\mathrm{K}$) is imposed except along the bottom walls where a zero Neumann condition (adiabatic walls) is imposed.

The coolant is considered air with constant thermophysical properties. The fluid density is taken $\rho^F = 1.2\,\mathrm{kg/m^3}$, the kinematic viscosity $\nu = 1.5 \times 10^{-5}\,\mathrm{m^2/s}$,

the specific heat capacity under constant pressure $c_p^F = 1006\,\text{J/(kg·K)}$ and the thermal conductivity $k^F = 0.026\,\text{W/(m·K)}$. The thermal conductivity of the solid regions is taken $k^S = 12.7\,\text{W/(m·K)}$ corresponding to ASTM 310 stainless steel. The air inlet temperature as well as the solid temperature and material used are taken similar to the ones reported in the experiment of Hylton et al. [49] for a real internally cooled turbine blade.

4.2 Results of the compressible solver

In this section, the results of the analysis of the CHT problem described in section 4.1 are presented. Results were produced using the standard OpenFOAM©solver for CHT analysis of steady compressible flow problems called chtMultiRegion-SimpleFoam. It solves the equations of mass, momentum and sensible enthalpy following a pressure-based segregated solution strategy. Despite that the solver is capable of analyzing compressible flows, the fluid density is set constant and the equation of state is omitted. This comes in accordance with the physics of the problem since flows with low Mach numbers (normally less than 0.3) can safely be studied as incompressible. In the context of this thesis, this solver will be referred to as **PBF1** (Primal Body-Fitted) so as to ensure that a clear distinction is made among the different solvers used for the primal problem.

The computed temperature field as well as the total pressure field are presented in fig. 4.3. As expected, the fluid enters the domain and its temperature rises, and the Solid1 region is cooled down. The two areas of Solid2 where the temperature is significantly lower, are the ones that are further away from the external wall where the Dirichlet BC for temperature ($T = 873\,\text{K}$) is set, and there is less material coming in contact with the fluid. The temperature of Solid2 is rising towards the outlet, as the coolant is heated up.
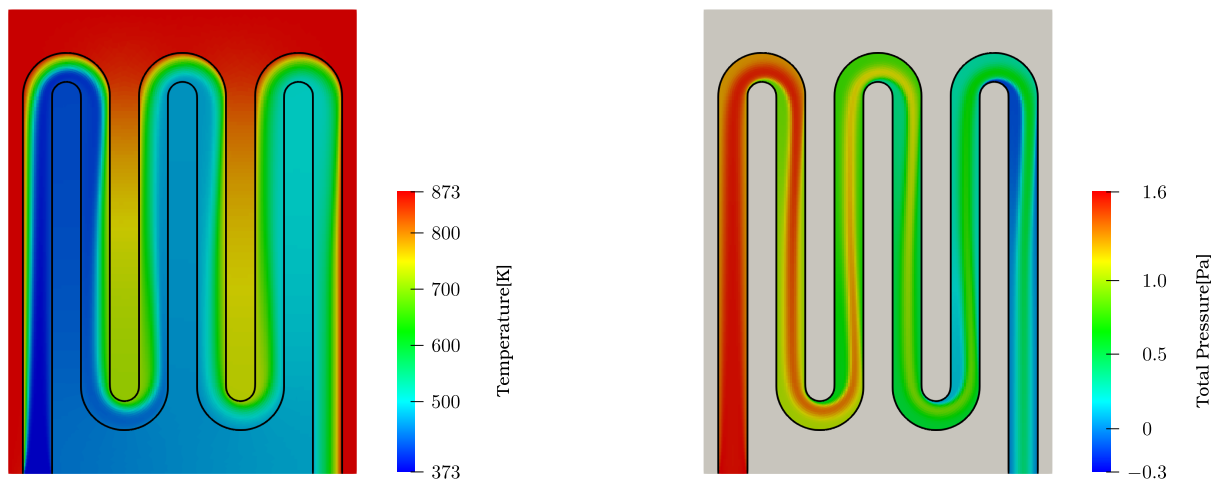
Figure 4.3: Temperature (left) and total pressure (right) field computed using **PBF1**.

Additionally, concerning the pressure field, there are distinct total pressure drops at certain regions of the duct. This is due to flow separation in those

areas, as the flow cannot follow the steep curvature of the duct. This is better visualized by the velocity field and the streamlines shown in fig. 4.4.
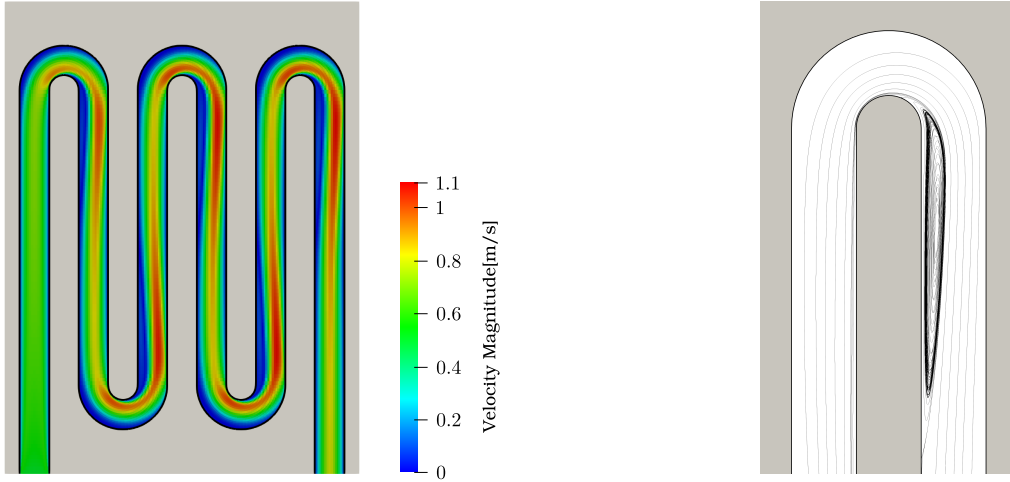

Figure 4.4: Velocity magnitude field (left) and streamlines at the separation area in the middle curve of the duct (right).

Investigating the heat balance in the domain, given that the analysis is steady over time, the heat entering from the external wall of the Solid1 region must be equal to the heat leaving the domain with the fluid at the outlet, minus the heat entering at the inlet. The rest of the boundaries are adiabatic, so they do not contribute to the heat balance. This is written as,

$$Q^S|_{wall} = Q^F|_{outlet} - Q^F|_{inlet} \tag{4.1}$$

The transfer of heat over a surface S of the solid region is due to conduction and is computed as,

$$Q^S = -\int_S k^S \frac{\partial T}{\partial x_j} n_j dS \tag{4.2}$$

Heat transferred by the flow is carried out in two ways, both by conduction and convection. Hence, the total heat of a fluid flowing through a surface S can be expressed mathematically as,

$$Q^F = Q^F_{cond} + Q^F_{conv} = -\int_S k^F_{eff} \frac{\partial T}{\partial x_j} n_j dS + \int_S \rho^F c_p^F T v_i n_i dS \tag{4.3}$$

The resulting heat transferred through the boundaries of the domain is presented in table 4.1. The sum of the total conductive and convective heat transfer over the domain is very close to zero denoting adequate convergence of the energy equation as well as an adequately conservative solver. The negative sign corresponds to heat leaving the domain while the positive sign is the heat entering the domain.

Additionally, the mean fluid temperature at the outlet and the total pressure losses are computed. The surface-averaged temperature of the fluid at the outlet computed through eq. (2.9) is $T_{out} = 629.6\,\text{K}$ while the total pressure losses are

$$\Delta p_t = p_t|_{inlet} - p_t|_{outlet} = 1.396\,\text{Pa} \tag{4.4}$$

Patch	Q_{cond}[W]	Q_{conv}[W]
External Solid Walls	18.705	—
Fluid outlet	0	-46.798
Fluid inlet	-0.049	28.143
$\sum$	18.656	-18.655

Table 4.1: Conductive and convective heat transfer over the domain boundaries.

where the surface-averaged total pressure at the inlet and outlet is

$$p_t = \frac{\int_S \left(p + \frac{1}{2}\rho^F v_k^2\right) dS}{\int_S dS} \tag{4.5}$$

4.3 Results produced by the solver developed by the PCOpt/NTUA

In this section, the results produced by the solver developed by the PCOpt/NTUA (adjointOptimisationFoam; only its primal solver) are showcased and the differences between the two solvers are assessed. This solver uses an incompressible fluid model. It solves the NS equations along with the energy equation in a segregated manner, with CHT between solid and fluid regions. Moreover, it solves the adjoint NS and adjoint energy equations and can be used for gradient-based optimization. The results only corresponding to the primal problem are discussed in this section, and the solver is referred to as the **PBF2** to discern it from the previous one.

The temperature field is shown in fig. 4.5. Next to it is the field resulting from the subtraction of the two temperature fields computed by the two different solvers.
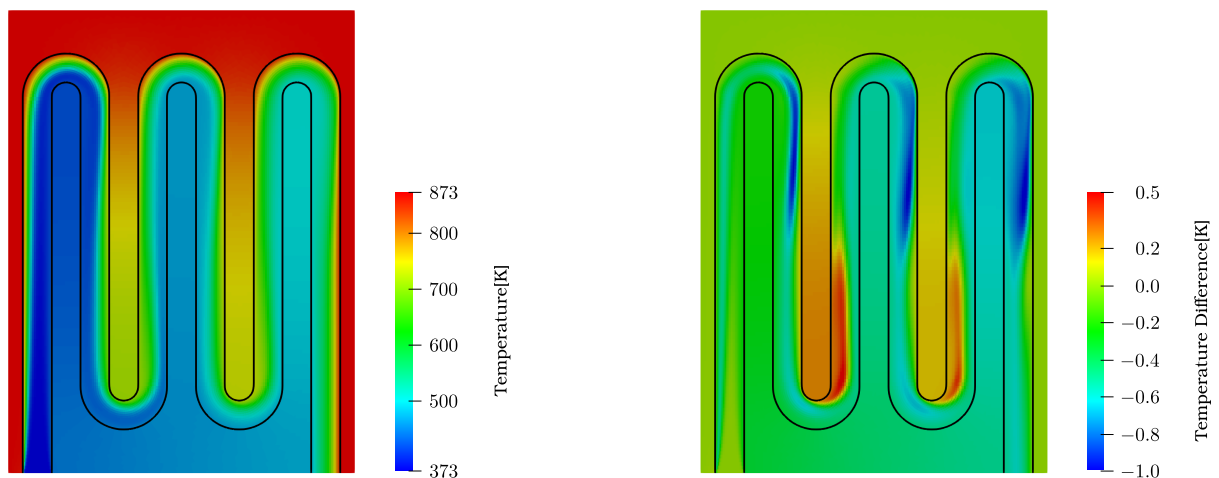
Figure 4.5: Temperature field computed by the **PBF2** solver (left), field of differences in the temperature between **PBF2** and **PBF1** (right).

The temperature fields computed by the two solvers are almost identical. While there are very small temperature differences, the results differ mostly in the fluid region, right at the separation zone.

To better understand the difference in the temperature fields, the velocity field computed by the **PBF2** as well as the differences in the velocity magnitudes computed by the two solvers, are depicted in fig. 4.6.
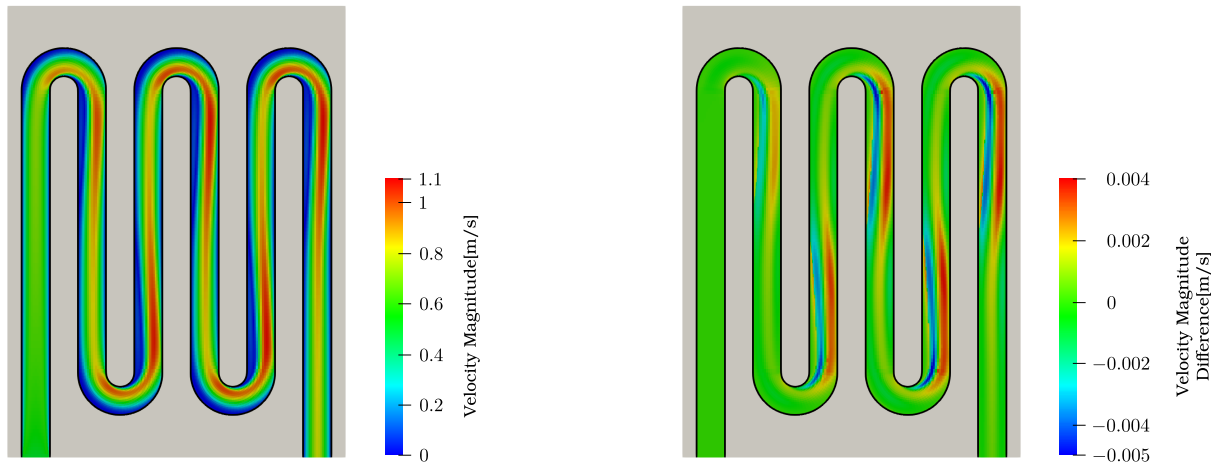
Figure 4.6: Velocity field computed by the **PBF2** solver (left), field of differences in the velocity magnitude between **PBF2** and **PBF1** (right).

The velocity fields are very close with very small differences in the velocity magnitudes. Again, the results differ mostly at the flow separation area where changes in flow quantities are more intense. The **PBF1** solver predicts slightly more extended recirculation zones. These zones act as an obstacle in the flow, forcing the mass flux to pass through a narrower passage in the duct which in turn, explains the higher velocity magnitudes computed by **PBF1** at the cells near the separation zone. Additionally, recirculation zones assist in the transfer of heat between the regions which explains the temperature differences shown on the right side of fig. 4.5. At the lower curved parts of the duct where the separation zone occurs at the interface between the Fluid and the Solid1 region, the temperature predicted by the **PBF1** is higher, as the heat transfer from the Solid1 region to the fluid is reinforced by the greater recirculation of the flow. The same thing happens at the upper curved parts of the duct, where the recirculation zone occurs at the interface between the fluid and the Solid2 region and, thus, heat is transferred more effectively from the fluid to the Solid2 region.

Finally, the temperature of the fluid at the outlet and the total pressure losses are computed by equations eqs. (2.9) and (4.4). The results produced by both solvers are presented in table 4.2. The difference in both the outlet temperature and total pressure losses computed by the two solvers is negligible.

	PBF1	**PBF2**
T_{out}[K]	629.6	630.1
Δp_t[Pa]	1.396	1.395

Table 4.2: Outlet temperature and total pressure losses computed by both solvers.

4.4 The ShpO Problem

In ShpO, a mesh displacement model is used so that the geometry and mesh are updated in each optimization cycle. In this thesis, a Volumetric B-Splines (VBS) Morpher [50] is used for the displacement of the mesh, and, therefore, the design variables are the x and y coordinates of the Control Points (CPs). Details about the use of VBS for surface parameterization and mesh displacement can be found in appendix A.

The parameterization box is shown in fig. 4.7 and consists of 11×21 control points, controlling the FSI. All boundary CPs are kept fixed.
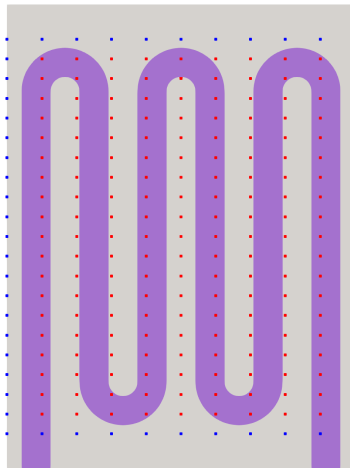
Figure 4.7: A 11×21 VBS box parameterizing the geometry. CPs in blue are kept fixed and red ones are allowed to move.

In ShpO, sometimes the simulation fails to continue due to overlapping cells in the mesh. To tackle this problem, bound constraints are imposed on the design variables. These constraints, ensure that there is no overlap between the CPs and therefore potentially prevent the cells of the mesh from overlapping. The Implicit SQP (SQP) update method [51] is applied and the quadratic sub-problem is solved using an interior point method with the ability to handle the inequality constraints. More details about this optimization method can be found in appendix B.1.

4.5   Results of ShpO

Four ShpO runs for four different weights in the objective function eq. (2.8) are performed. The selected weights are:

1. $w = 0.9$

2. $w = 0.8$

3. $w = 0.5$

4. $w = 0.2$

For values of $w > 0.5$, the maximization of the temperature objective is of higher significance than the minimization of total pressure losses. The optimal geometry produced for the current parameterization and optimizations using combinations of weights is shown in fig. 4.8.
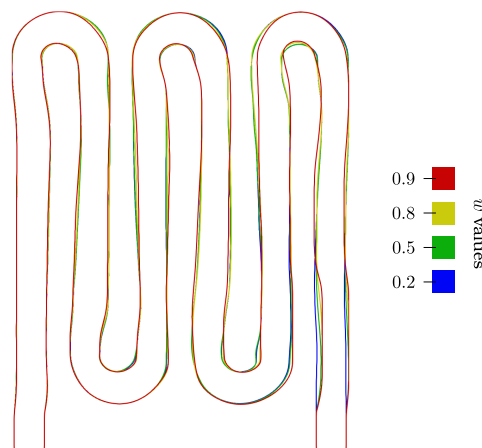
Figure 4.8: Optimized geometry for the four different weights used.

The duct geometry certainly becomes less wavy as the value of w is lowered. Wavy surfaces assist the transfer of heat between the regions, firstly because the FSI becomes longer and secondly it causes wider recirculation zones to appear. This comes in contrast with the second objective of minimizing the total pressure losses, which is achieved with less wavy geometries.

The two geometries that resulted from the optimization with the lowest and largest values of w, $w = 0.2$ and $w = 0.9$ respectively, are depicted in fig. 4.9 on top of the original geometry to visualize the change in the geometry produced by the ShpO.
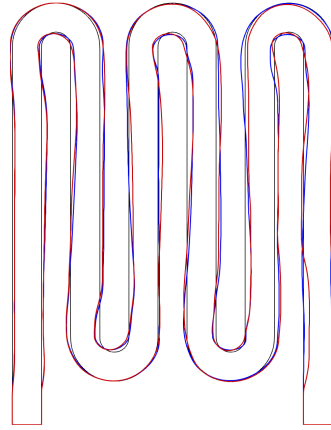
Figure 4.9: The red line corresponds to the geometry resulted for $w = 0.9$, the blue for $w = 0.2$ and in black is the original geometry.

The computed temperature fields for the cases with $w = 0.9$ and $w = 0.2$ are presented in fig. 4.10.
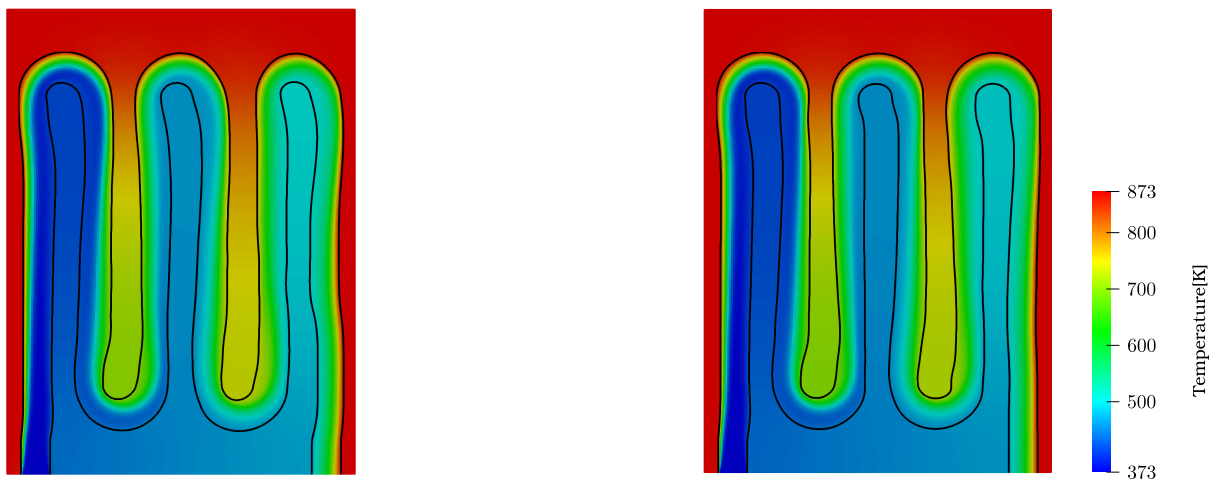
Figure 4.10: Resulting temperature fields for $w = 0.9$ (left) and $w = 0.2$ (right).

The main difference in the temperature fields appears in the Solid2 region. As the value of w is lowered and the total pressure losses objective becomes more important, the resulting temperature of the Solid2 region drops. Considering that the lower boundaries of the domain are adiabatic, this means that for $w = 0.9$ greater amount of heat is absorbed from the Solid1 region and transferred to Solid2 through the fluid, meaning that the cooling is done more effectively.

The velocity magnitude field for the two previous cases is presented in fig. 4.11.
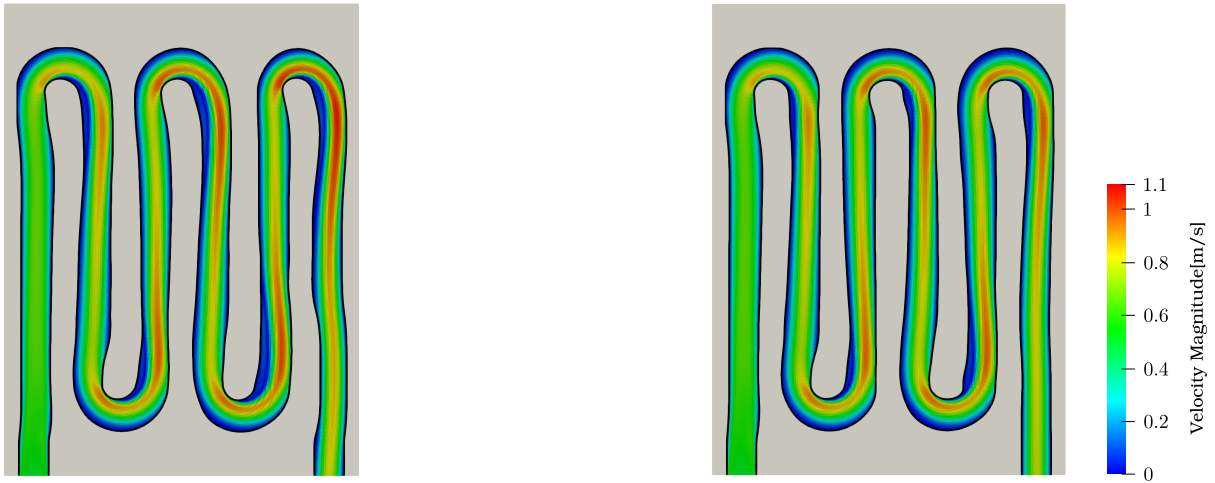
Figure 4.11: Resulting velocity magnitude fields for $w = 0.9$ (left) and $w = 0.2$ (right).

There is an obvious drop in velocity magnitude as the w value is decreased. Bigger velocity magnitudes contribute to higher total pressure losses. Viewing the velocity fields from left to right, the recirculation zones become smaller which enables the mass flow to take advantage of a bigger part of the duct cross-section, resulting in smaller velocity magnitudes and lower total pressure losses.

Finally, in table 4.3, the mean fluid temperature at the outlet and the total pressure losses calculated by eqs. (2.9) and (4.4) respectively are presented with an additional weight value. For the case with $w = 0.95$, the optimization converged until the fourth cycle where the mesh displacement caused overlapping cells and so the simulation was terminated. The results are also depicted in fig. 4.12 with the left vertical axis representing the mean outlet temperature and the right axis the total pressure losses. At the x-axis, the value of w weight used in the objective function is measured.

w	T_{out}[K]	Temperature increase	Δp_t[Pa]	Losses decrease
0.95	645.4	2.43 %	1.517	−8.69 %
0.9	635.3	0.82 %	1.250	10.42 %
0.8	630.5	0.07 %	1.178	15.46 %
0.5	627.2	−0.45 %	1.165	16.49 %
0.2	622.9	−1.13 %	1.149	17.67 %

Table 4.3: Outlet temperature and total pressure losses for different weights in the objective function.
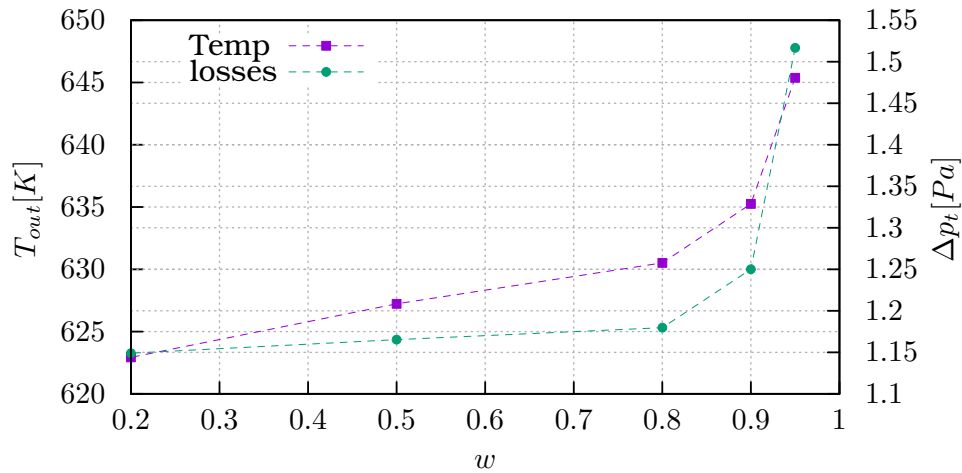
Figure 4.12: Results presented in table 4.3. The left axis represents the mean outlet fluid temperature, the right axis shows total pressure losses. Five different weights are presented.

The convergence of the primal and adjoint equations in the first optimization cycle is shown in fig. 4.13. Specifically, in fig. 4.13a, the normalized residuals of the primal and adjoint NS equations are presented, while also mentioning the relaxation factors used for each flow quantity in the setup of the SIMPLE algorithm. Additionally, in fig. 4.13b, the residuals of the primal and adjoint energy equations are presented as well as the relaxation factors, for all domain regions. The superscripts S_1 and S_2 found in the legend in fig. 4.13b denote the residuals of the heat conduction equations solved in Solid1 and Solid2 regions respectively.
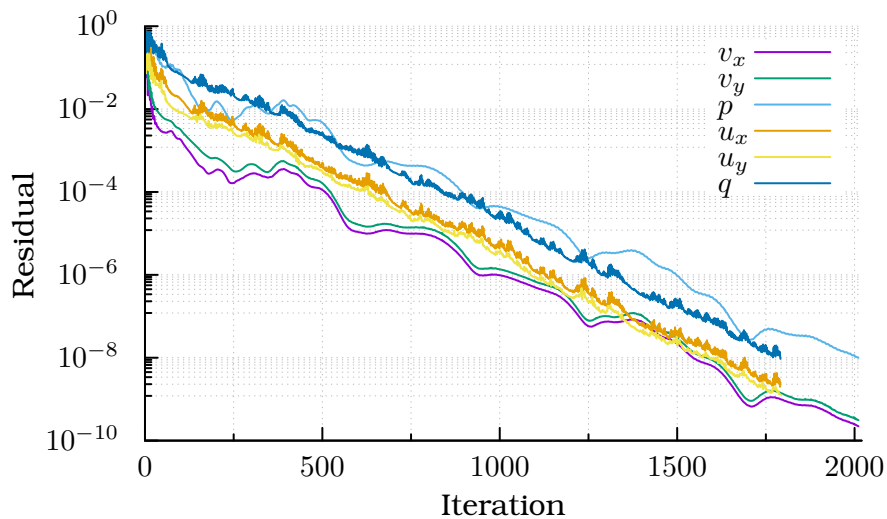
(a) NS equations' residuals; relaxation factors used are 0.3 for the pressure (primal and adjoint), 0.7 for the velocity (primal and adjoint).
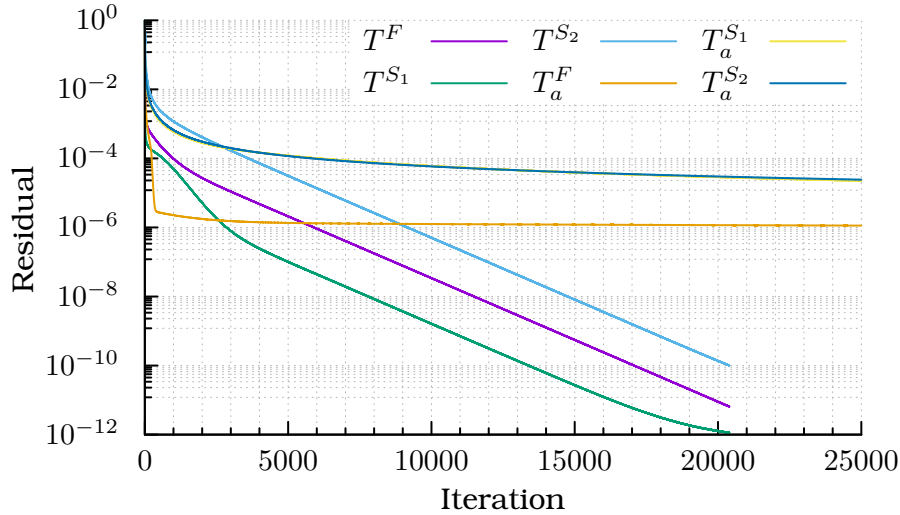
(b) Energy equations' residuals; relaxation factors used are 1.0 for the temperature in all regions, 0.8 for the adjoint temperature in the fluid region and 1.0 in the solid regions.

Figure 4.13: Convergence of the primal and adjoint equation residuals on the first optimization cycle.

A notable observation is that the energy equations require more iterations to converge compared to the NS equations. This is because, the fluid energy PDE and the solid heat conduction equations are solved in a segregated manner, meaning that the boundary conditions for temperature at the FSI boundary are updated in each iteration of the solver. Moreover, the residual of the energy equation should decrease at an order of 10^{-10} for it to be considered adequately converged.

The normalized total objective function in each optimization cycle for the four weight combinations is plotted in fig. 4.14a. For all the cases, a significant drop in the value of the objective function is observed in the first three optimization cycles and is, then, dropping at a much slower rate.
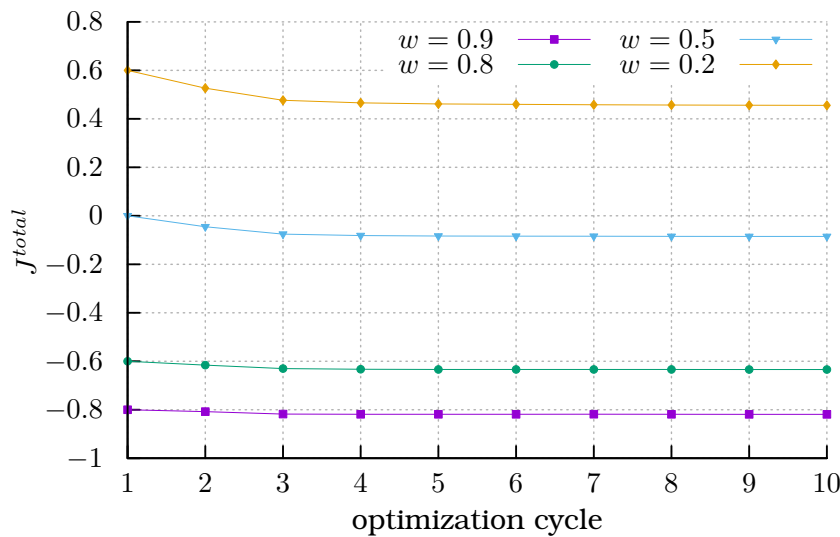
(a) Normalized total objective function for four weight values.
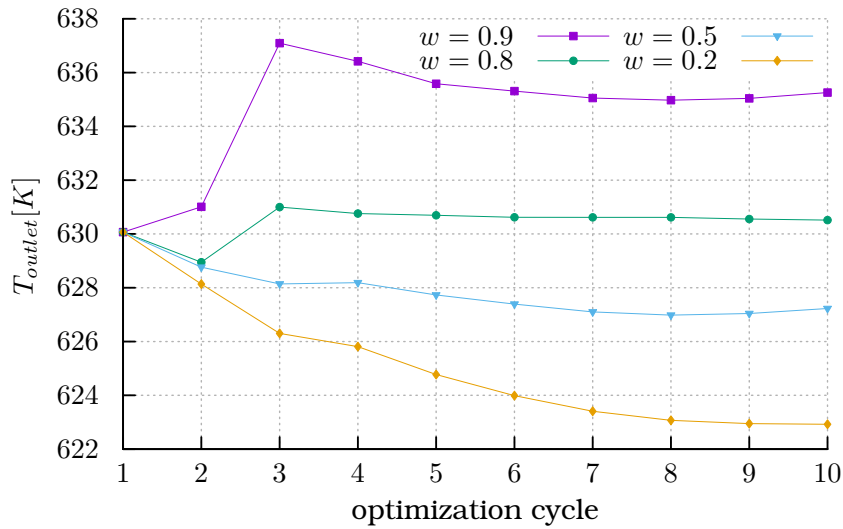
(b) Mean outlet temperature in each optimization cycle for four weight values.
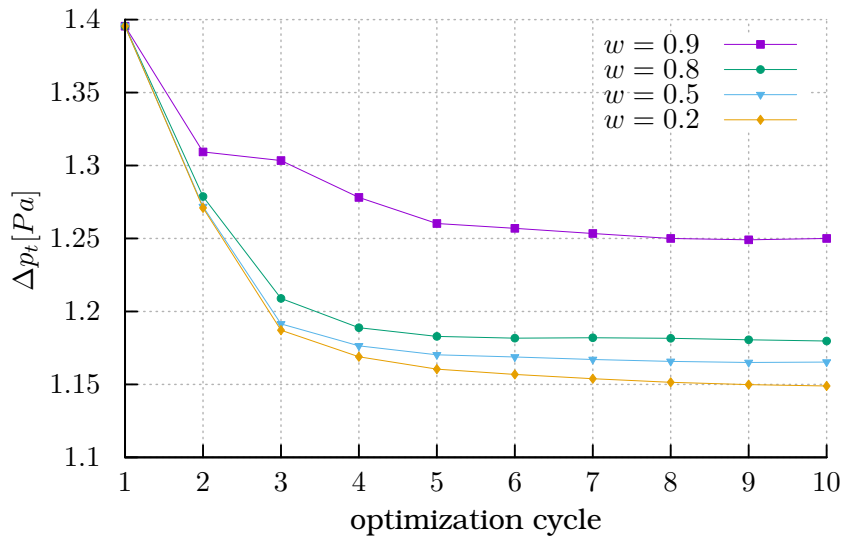
(c) Total pressure losses in each optimization cycle for four weight values.

Figure 4.14: Convergence of the normalized total objective function as well as of each objective comprising it.

Additionally, the drop in the objective function is bigger as the total pressure losses objective becomes more significant. The values in each optimization cycle of the mean outlet temperature as well as the total pressure losses are presented in fig. 4.14b and fig. 4.14c respectively.

4.6 Conclusions

In this chapter, a CHT analysis was conducted on a test case inspired by an internally cooled turbine blade. At first, the analysis was performed using the publicly available OpenFOAM©solver the results of which were compared with the ones produced by the solver developed by the PCOpt/NTUA. Both solvers gave similar results summarized in table 4.2. After that, the solver developed by the PCOpt/NTUA was used to optimize the shape of the serpentine-like duct. The geometry was optimized with the objectives being the maximization of the mean fluid temperature at the outlet and the minimization of total pressure losses. Multiple weights in the objective function were tested and the results as well as their percent change from the original geometry were outlined in table 4.3. The outlet temperature objective was multiplied by w while the total pressure losses objective was multiplied by $(1 - w)$. According to fig. 4.8, for greater w values the duct becomes wavy which assists the transfer of heat between regions because the FSI becomes longer and recirculation zones in the flow appear. Also, the duct comes closer to the heated external wall of the domain near the outlet which further increases the flow temperature. On the other hand, when the w value is reduced, the resulting duct is wider and so the velocity magnitudes in the flow are smaller which contributes to the minimization of total pressure losses.

Chapter 5

Analysis with the Porosity-Based solver

In this chapter, the TopO of the cooling duct of the test problem studied in chapter 4 is presented. In section 5.1, the primal CHT problem is solved using the porosity-based solution approach. An analysis is conducted to investigate how certain parameters affect the convergence and the results of the problem. Additionally, TopO is performed for different setups and the results are discussed.

5.1   Primal solution using the porosity-based solver

The primal CHT problem described in section 4.1 is solved using a porosity-based solver where the fluid and solid domains are represented by a porosity field α. In particular, this solver differs from the **PBF1** (section 4.2) and **PBF2** (section 4.3) as it solves a single system of equations (eqs. (3.1)) in both the fluid and solid domains. To distinguish this solver from the aforementioned ones, it will be called **PPB** (Primal Porosity-Based).

In the porosity-based approach, the FSIs are not defined as features of the mesh. A consequence of this is that there are no BCs imposed along the interfaces of the solid and fluid domains and their omission may introduce significant inaccuracy in the results. The purpose of this section is to quantify those inaccuracies derived from the porosity-based approach, as the same solution method will later on be used to optimize the topology of the turbine blade cooling duct.

For this case, the BFM1 mesh is used (fig. 4.2). The porosity field is set to represent the initially designed duct geometry (fig. 4.1). The mesh and the initial conditions for the porosity field α are shown in fig. 5.1.
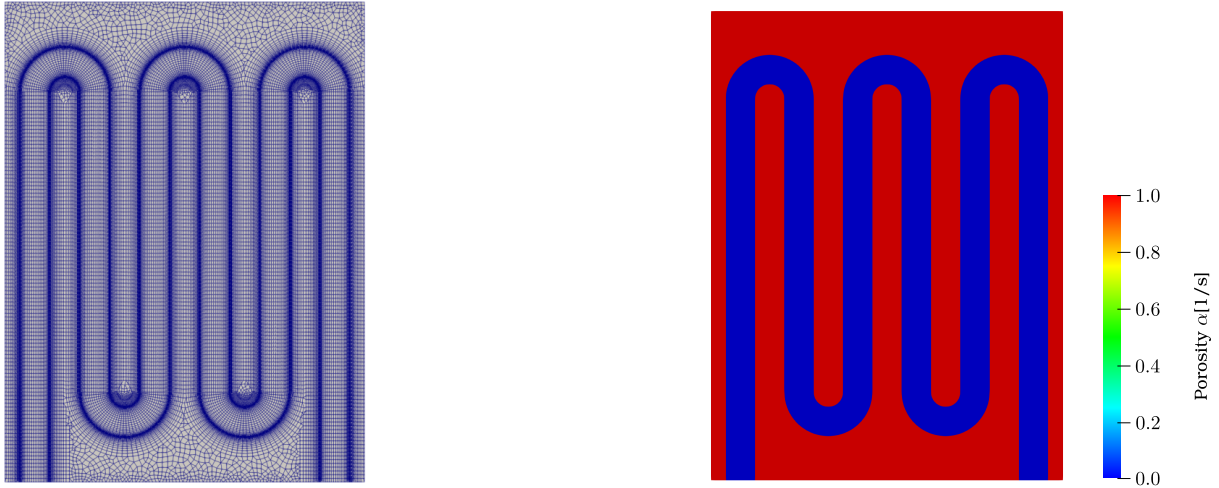
Figure 5.1: BFM1 mesh (left), porosity field (right)

For the value of $\alpha = 1$, the region corresponds to solid, while for $\alpha = 0$ the region corresponds to fluid. The values of the porosity field are set using an OpenFOAM©utility so that the separate mesh regions correspond to the ones shown in section 4.1. The primal equations are solved using the topology primal solver and the accuracy of the computations is evaluated based on the results produced by the **PBF2** code in section 4.3.

The value of β_{max} is critical for the convergence of the equations. Examining the additional source term in the momentum equation eq. (3.1b), if $\alpha = 1$ and therefore the region studied is solid, the bigger the value of β_{max}, the more the computed velocity approaches zero. This means that a bigger value of β_{max} results in a sharper distinction of regions and greatly affects the accuracy of the computations. Nonetheless, very large β_{max} values can significantly change flow behavior, especially in optimization cases where the porosity field is not strictly binary and there is a user-defined upper bound in porosity values for which a cell is included in the fluid domain.

A parametric analysis based on β_{max} is conducted and the results are presented in table 5.1. The solver converges for values of approximately $\beta_{max} = 2 \times 10^4 \, [1/s]$ or higher. Then, several runs were performed, doubling its value each time till the outlet temperature and total pressure losses computed by eqs. (2.9) and (4.4) do not exhibit significant changes.

$\beta_{max}[1/\text{s}]$	$T_{out}[\text{K}]$	T_{out} error	$\Delta p_t[\text{Pa}]$	Δp_t error
2.00×10^4	628.03	$0.323\,\%$	1.407	$-0.791\,\%$
4.00×10^4	629.24	$0.132\,\%$	1.398	$-0.203\,\%$
8.00×10^4	629.82	$0.039\,\%$	1.395	$0.014\,\%$
1.60×10^5	630.10	$-0.005\,\%$	1.394	$0.089\,\%$
3.20×10^5	630.23	$-0.026\,\%$	1.394	$0.111\,\%$
6.40×10^5	630.29	$-0.035\,\%$	1.394	$0.114\,\%$
1.28×10^6	630.32	$-0.039\,\%$	1.394	$0.112\,\%$

Table 5.1: Outlet total temperature and pressure losses computed by **PPB** for different values of β_{max}.

The percentage errors are computed as

$$\eta = 100\% \times \frac{J - J'}{J}$$

with J being the objective value produced by the **PBF2** solver presented in table 4.2 and J' being the values computed by the **PPB** solver. The results show that the solution of the **PPB** solver is very close to the ones computed by the **PBF1** and **PBF2** solvers in sections 4.2 and 4.3 respectively, regardless of the absence of BCs along the FSI. This is mostly because the porosity field is strictly binary and the region interfaces are well-defined. If "grey" areas were present in the porous media domain, there would probably be significant divergence in the results.

Observing table 5.1, the results are dependent on the β_{max} value even though the corresponding Darcy number in each case is lower than $Da = 10^{-5}$. It can therefore be concluded, that the solid is not completely impermeable for $Da = 10^{-5}$. As the value of β_{max} increases, the results converge to certain values corresponding to the solution for a completely impermeable solid.

The results produced by the three solvers are summarized in table 5.2 where the results of the case with $\beta_{max} = 1.28 \times 10^6$ are used. It can be seen that the values computed by **PPB** are close to the ones computed by the other two solvers. To investigate this matter, the fields computed by the **PPB** solver are examined and compared to the ones computed by the **PBF2** solver.

	PBF1	**PBF2**	**PPB**
$T_{out}[\text{K}]$	629.6	630.1	630.3
$\Delta p_t[\text{Pa}]$	1.396	1.395	1.394

Table 5.2: Outlet temperature and total pressure losses computed by the three solvers.

In fig. 5.2, on the left, there is the velocity magnitude field while the field on the right corresponds to the difference in the velocity magnitude fields computed by the **PPB** and **PBF2** solvers.
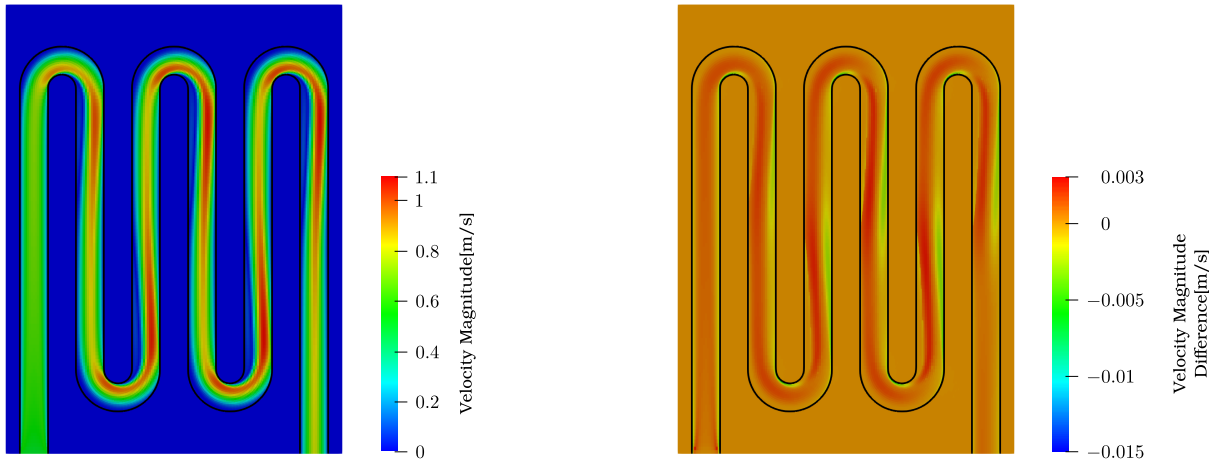
Figure 5.2: Velocity magnitude field for $\beta_{max} = 1.28 \times 10^6\,[1/\mathrm{s}]$ (left), field of differences in the velocity magnitude between **PPB** and **PBF2** (right).

Observing the velocity magnitude differences field, deviations exist mostly at the region interfaces. Specifically, the differences are bigger near the inlet and at the curved part where the flow velocity magnitude is bigger. The **PBF2** solver computes smaller velocity magnitudes at those areas which is due to the imposition of the no-slip condition. On the other hand, the topology solver tries to capture this flow behavior through the additional source term in the momentum equation. The results show that, at the region interfaces near the inlet, where the flow has not settled, and in areas of high velocity gradient, the **PPB** solver is more prone to errors.

The temperature field as well as the differences between the two solvers are presented in fig. 5.3.
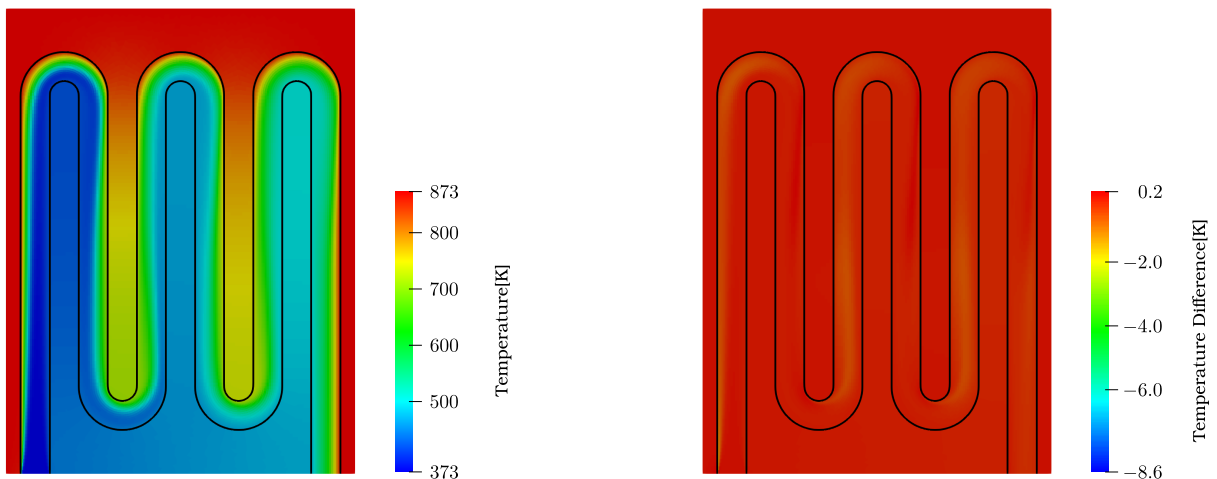
Figure 5.3: Temperature field for $\beta_{max} = 1.28 \times 10^6\,[1/\mathrm{s}]$(left), field of differences in temperature between **PPB** and **PBF2** (right).

It does not show any significant difference comparing it with the previous ones. Similarly to the previous results, the main divergence between the temperature fields is located right at the inlet.

In fig. 5.4, temperature differences along the width of the inlet are plotted, to better visualize the differences in the results.
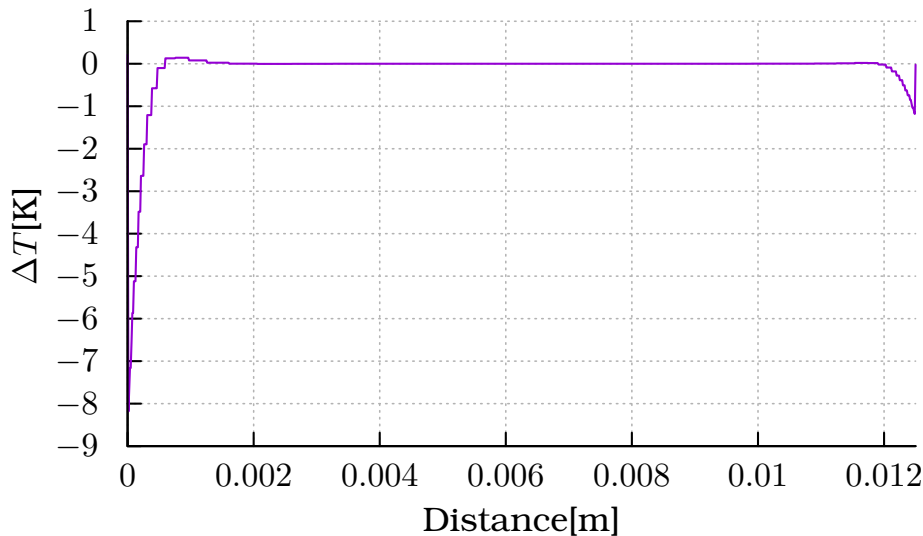

Figure 5.4: Temperature differences along the inlet

The zero distance in the horizontal axis of the figure corresponds to the interface between the fluid and the Solid1 at the inlet. The magnitude of the differences there is the highest computed and it extends near the inlet and specifically close to the walls. This is caused due to the absence of a Dirichlet temperature condition at the FSIs that guarantees temperature equality and heat-flux conservation. Soon after the inlet that the flow settles, those differences in the temperature fields become smaller.

5.2 TopO on the BFM1

In this section, TopO is conducted on the BFM1 (fig. 4.2). The dynamic TopO method is used which means that the porosity field is not updated simultaneously at all cells, but only in automatically selected ones called "active". In each subsequent optimization cycle, the set of "active" cells is enriched with cells neighboring to the current ones, before updating the porosity field. Dynamic TopO can potentially produce better results than the classic TopO approach. In classic TopO, the optimization algorithm is often stuck to a local minimum in the first few cycles which in dynamic TopO is tackled by gradually increasing the number of design variables. The downside is that dynamic TopO usually increases the computational cost of the optimization.

Four cases were run with the same weights as the ones tested in section 4.5. The optimization starts with an all-fluid state meaning that the initial field of the porosity has zero value at all cells. For the interpolation of thermal conductivity k, the SIMP function is used as described by eq. (3.4), where b is a parameter controlling the steepness of the interpolation function. This parameter is chosen constant and equal to $b = 3$.

For the projection of the regularized porosity field $\tilde{\alpha}$, the tanh function is used, described by eq. (3.7), with b again being a sharpening parameter. For

the first 50 optimization cycles, a constant value of $b = 3$ is used. Additionally, a marching step that adds 40 new cell rows in the design space in each optimization cycle is used, starting from the bottom of the domain and moving vertically upward. After the tenth cycle, the whole design space belongs to the set of "active" cells. Then, another 50 cycles are run with the classic TopO approach. This time, the sharpening parameter b starts at $b = 2$ and increments by two, every ten optimization cycles.

The β_{max} value is computed based on the Darcy number, through eq. (3.5) where $L = 1.25 \times 10^{-2}$ is the inlet length and $Da = 1 \times 10^{-5}$ is the value chosen for the Darcy number based on [35]. The resulting value for β_{max} is 9600. The Method of Moving Asymptotes (MMA) [52] is used to update the values of the porosity since it is designed to efficiently handle multiple bound constraints which is critical for TopO considering that the design variables are bound in the set $[0, 1]$. More about this method can be found in appendix B.2.

The objective function is the same as the one used for the previous cases (eq. (2.8)) which combines two objectives, the maximization of the fluid temperature at the outlet and the minimization of the total pressure losses. Finally, there is an inequality constraint imposed so as to control the volume occupied by the fluid in the domain. This is written as,

$$J = \frac{\int_{\Omega}(1 - \beta)d\Omega}{\int_{\Omega} d\Omega} - \pi_{tar} \leq 0 \tag{5.1}$$

where π_{tar} is the maximum value of the percentage of fluid volume to the total volume of the domain. This value is set to $\pi_{tar} = 0.426$ which corresponds to the percentage of fluid in the domain used in previous cases (fig. 4.1).

The resulting porosity fields are shown in fig. 5.5. Although the mesh is fitted to the geometry of the original serpentine fig. 4.1, no similarities are observed. Instead, a porosity field closer to a U-shaped duct design was derived.
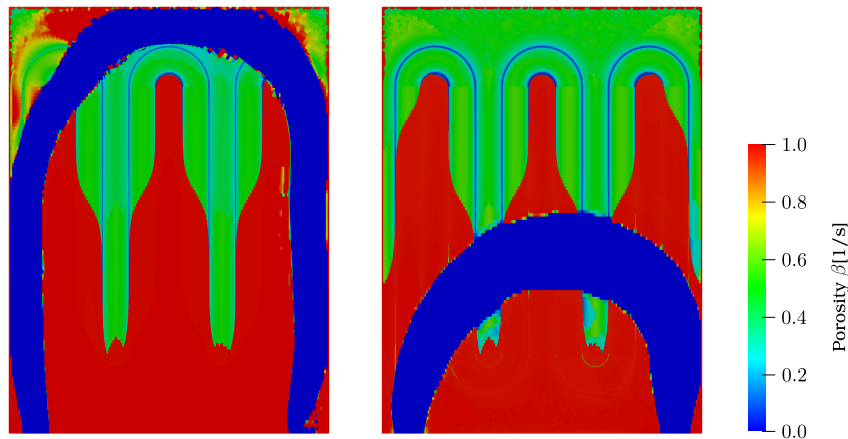

Figure 5.5: Resulting porosity fields for different weights in the objective function, $w = 0.9$ (left), $w = 0.2$ (right). The flow area is in blue and the rest of the domain is considered solid.

If maximizing the mean outlet temperature is of higher significance, the TopO tends to block the outlet and the designed duct reaches for the heated boundaries of the domain. On the other hand, when the minimization of the

total pressure losses is more important, the length of the duct becomes smaller and its width increases.

The temperature and velocity fields are shown for the two cases in figs. 5.6 and 5.7 respectively. The temperature of the Solid2 region for the case with $w = 0.9$ is higher while the velocity magnitude is smaller for $w = 0.2$.
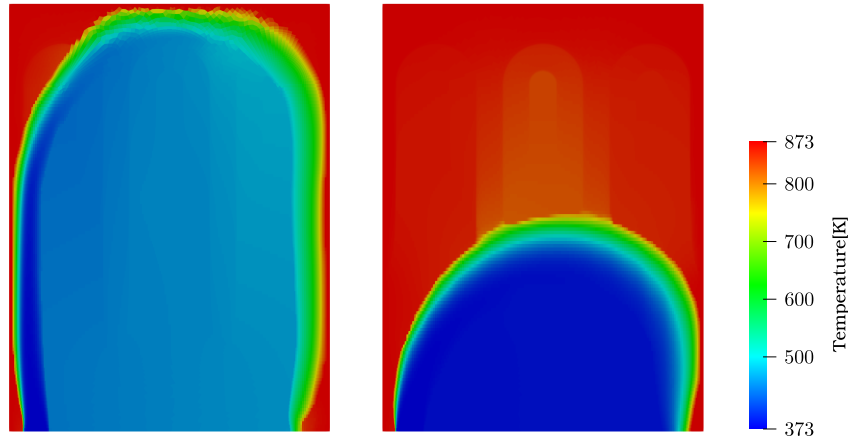

Figure 5.6: Resulting temperature fields for different weights in the objective function, $w = 0.9$ (left), $w = 0.2$ (right).
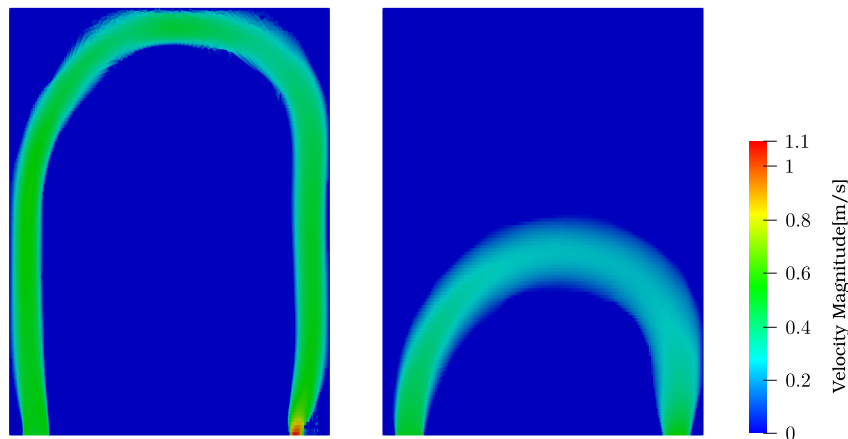

Figure 5.7: Resulting velocity fields for different weights in the objective function, $w = 0.9$ (left), $w = 0.2$ (right).

The mean fluid temperature at the outlet, total pressure losses and FSI length computed in each case, are presented in table 5.3 for the two weights.

w	T_{out}[K]	Δp_t[Pa]	FSI length[m]
0.9	747.7	0.679	0.950
0.2	517.5	0.071	0.501

Table 5.3: Outlet temperature, total pressure losses and FSI length for different weights in the objective function.

Finally, the normalized total objective function convergence is plotted in fig. 5.8a. Moreover, the values in each optimization cycle of the mean outlet
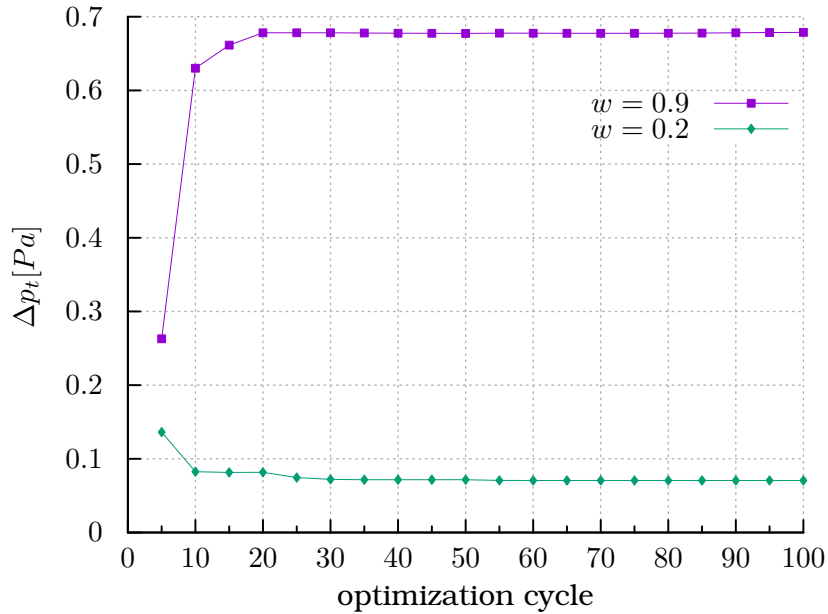
temperature as well as the total pressure losses are presented in fig. 5.8b and fig. 5.8c, respectively.
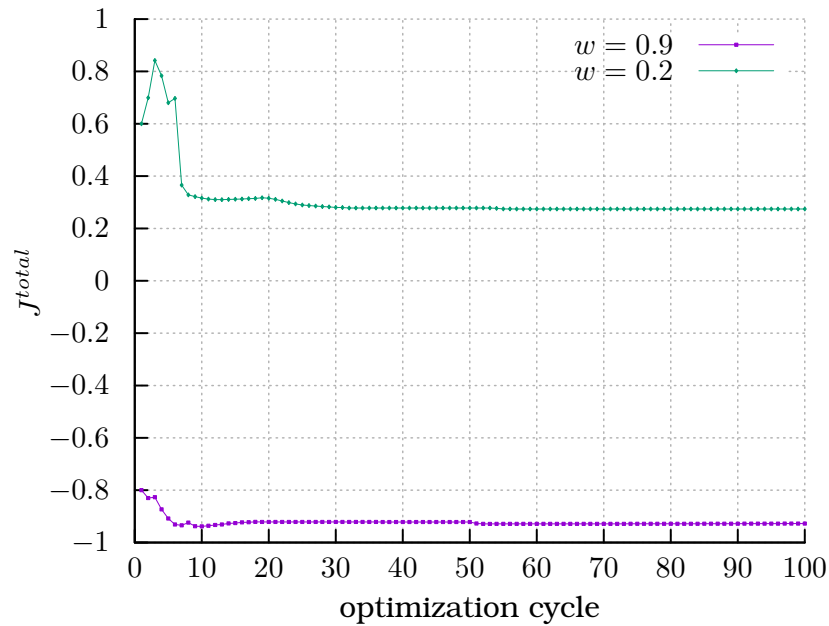
(a) Normalized total objective function for two different weight values.
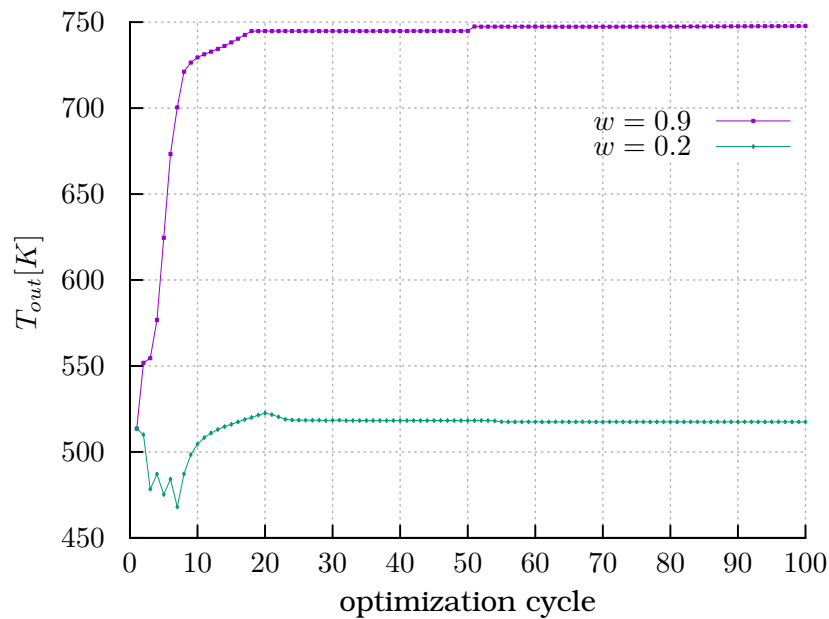
(b) Mean outlet temperature in each optimization cycle for two different weight values.

(c) Total pressure losses in every five optimization cycles for two different weight values.

Figure 5.8: Convergence of the normalized total objective function as well as of each objective comprising it.

5.3 TopO on a Structured Mesh

A new fully-structured mesh is generated for TopO, called PM1 (Porosity Mesh), named after the porosity techniques used in the optimization. It is typical for fully-structured meshes to be used in TopO since the geometry is initially unknown and formed during the optimization process.

5.3.1 Mesh Independence Study

The PM1 mesh is presented in fig. 5.9. A notable difference in the geometry is that there are straight extensions added to the inlet and the outlet of the domain. Those straight extensions are added so that the flow develops before entering the design space.

A mesh independence study is conducted to examine the appropriate mesh density. A coarse mesh with $\sim 30K$ cells, a medium-density mesh with $\sim 60K$ cells and a fine one with $\sim 120K$ cells, are tested. The porosity field is initialized to approximate the original geometry of the serpentine-shaped duct used in the original test case (fig. 4.1). In detail, an OpenFOAM©utility was used to "paint" in red (unitary porosity value) cells that are outside of the fluid domain while the rest were painted in blue (zero porosity value) as shown in fig. 5.9. Since the PM1 is not fitted to the serpentine-shaped duct geometry, the representation of the geometry through the porosity field is not exact.
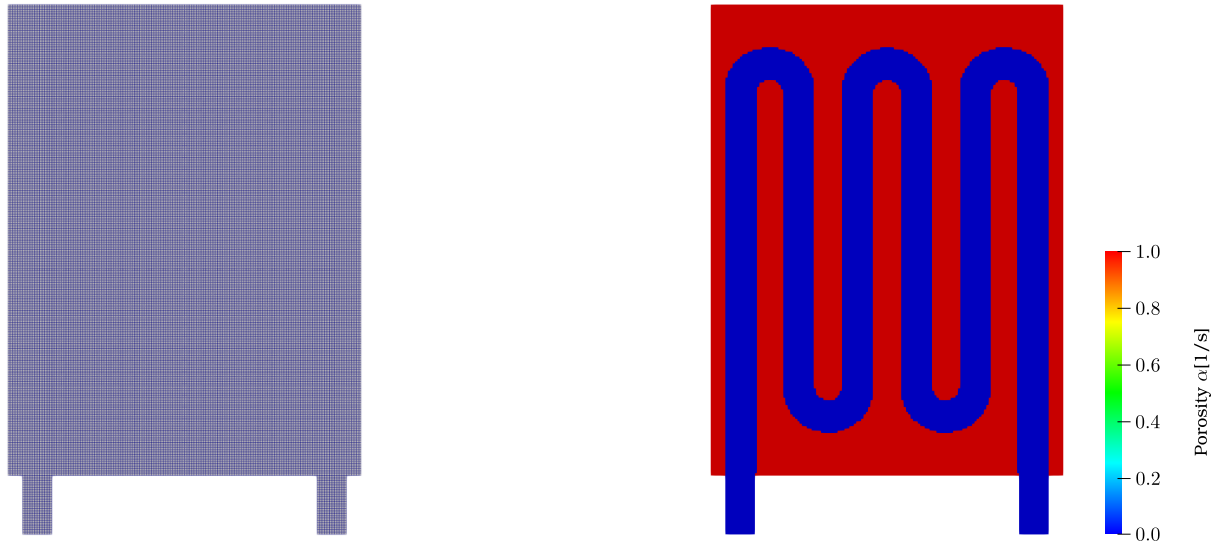
Figure 5.9: PM1 with $\sim 30K$ cells (left), porosity field approximating the original geometry (right)

The geometry representation through the porosity field will be more accurate as the number of cells in the mesh increases. Only the primal problem is solved using the **PPB** solver and the computed mean outlet temperature, total pressure losses and FSI length for the different mesh densities are presented in table 5.4. It is worth noting that the exact FSI length of the geometry is $2.043\,\mathrm{m}$.

Mesh size	$\sim 30K$	$\sim 60K$	$\sim 120K$
T_{out}[K]	684.7	663.4	651.3
Δp_t[Pa]	1.303	1.281	1.278
FSI length[m]	2.150	2.150	2.150

Table 5.4: Outlet temperature and pressure losses for different mesh densities.

The value of mean fluid temperature at the outlet decreases as the mesh density rises. With the decrease in cell density of the mesh, the FSI walls become more jagged causing more and wider recirculation areas in the flow, which assist the exchange of heat between the regions. On the other hand, jagged FSI walls contribute to larger total pressure losses.

To sum up, based on the mesh independence study, the PM1 consisting of $\sim 120K$ cells will be used for the optimization as it gives satisfactory results compared to the ones produced by the previous solvers summarized in table 5.2. Further refinement of the mesh will give even better results, but the computational cost of the optimization is a limiting aspect.

5.3.2 TopO on the PM1 mesh

TopO runs for three different weights in the objective function (eq. (2.8)). The weights used are:

1. $w = 0.95$

2. $w = 0.9$

3. $w = 0.8$

The value of the sharpening parameter b is given as a stepped ramp function which starts at $b = 1$ and increases every 5 optimization cycles by 1. The objective function is the same as the one used for the previous cases (eq. (2.8)). The constraint imposed on the volume of fluid in the domain described by eq. (5.1) has the value $\pi_{tar} = 0.437$ after including the straight extensions so that the percentage of fluid in the domain is the same as in fig. 4.1.

The porosity fields produced by the TopO after 50 optimization cycles are shown in fig. 5.10.
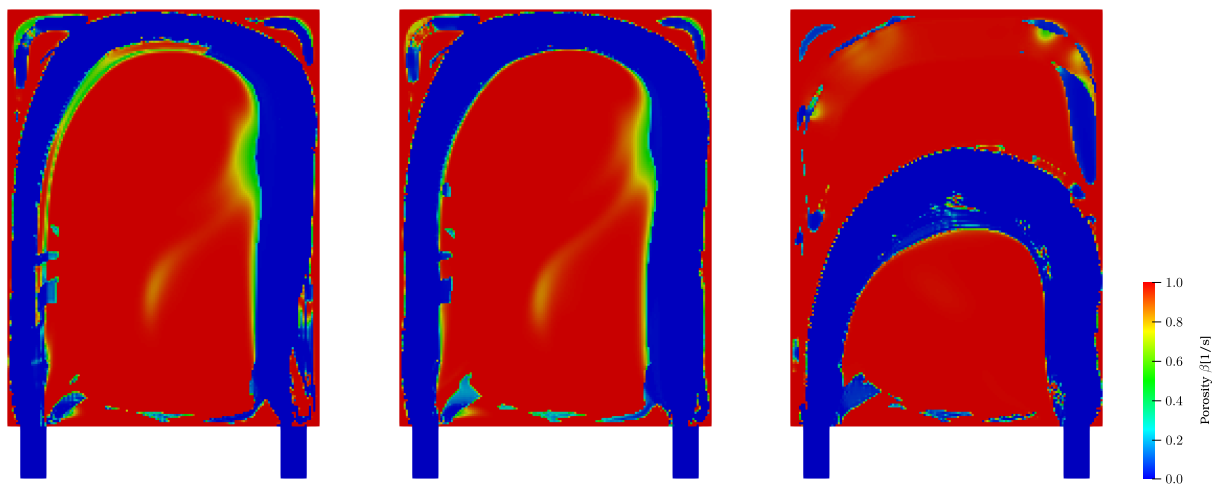
Figure 5.10: Resulting porosity fields for different weight combinations $w = 0.95$ (left), $w = 0.9$ (middle), $w = 0.8$ (right)

Viewing the figure from left to right, the first two fields do not seem to have many differences except that the duct in the middle is smoother and more well-defined than that on the left side. In both cases, the duct comes close to the heated boundaries of the domain so that the fluid exits at the highest temperature possible. On the other hand, the duct on the right side is further away from the top and left boundary of the domain and so its length is smaller than the other two. This greatly decreases the total pressure losses which are of greater importance when $w = 0.8$, in contrast to the other two cases.

The temperature fields corresponding to the above-mentioned porosity fields are presented in fig. 5.11.
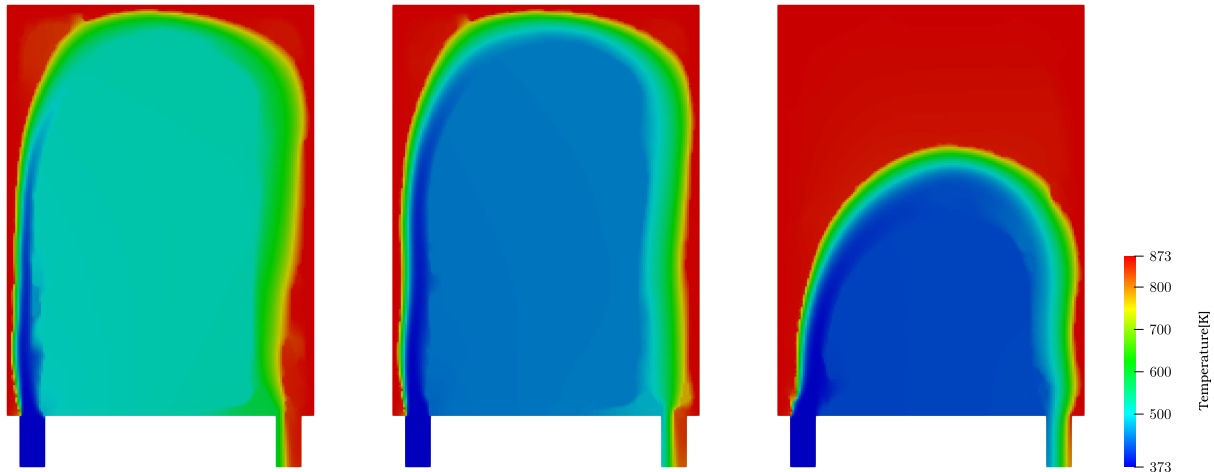
Figure 5.11: Resulting temperature fields for different weight combinations $w = 0.95$ (left), $w = 0.9$ (middle), $w = 0.8$ (right)

It is obvious that for $w = 0.95$ the temperature rise in the domain is significantly larger than in the other two cases. This is achieved due to the duct being closer to the left domain boundary near the inlet and because there is a solid island interrupting the flow near the outlet, further heating the fluid before exiting the domain. By slightly decreasing the value of w, the island near the outlet disappears as its presence increases the total pressure losses significantly, but also the outlet fluid temperature falls.

The velocity magnitude fields for the three cases are shown in fig. 5.12.
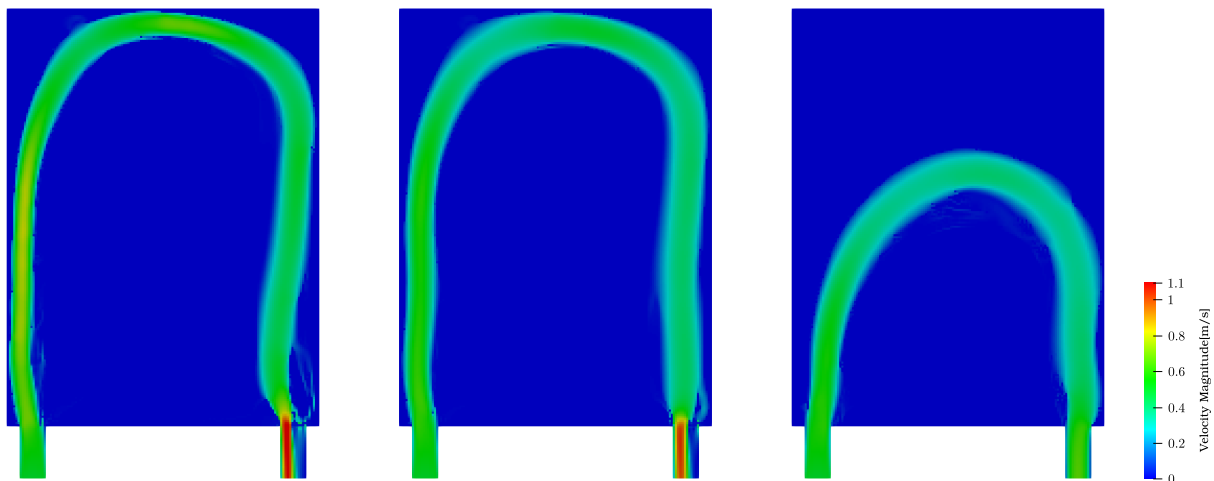

Figure 5.12: Resulting velocity magnitude fields for different weight combinations $w = 0.95$ (left), $w = 0.9$ (middle), $w = 0.8$ (right)

With the decrease of w, the width of the duct seems to become larger. This allows for smaller velocity magnitudes which in turn contributes to the decrease in total pressure losses. These conclusions are confirmed by the results of fig. 5.12.

The outlet fluid temperature computed through eq. (2.9), as well as the total pressure losses computed through eq. (4.4) are presented in table 5.5.

Comparing the TopO results to the ones produced by the primal solvers (**PBF1**,

| w	T_{out}[K]	Δp_t[Pa]
0.95	764.9	1.291
0.9	698.2	0.709
0.8	605.6	0.274

Table 5.5: Outlet temperature and total pressure losses for different weights in the objective function. Results produced by TopO on PM1 mesh.

PBF2, **PPB**), it is obvious that the mean outlet temperature is overestimated by the topology and the opposite for the total pressure losses.

In fig. 5.13a, the J^{total} convergence is shown for the three cases. In the first few cycles, the value of the objective function is not dropping constantly. This is because, at the beginning of the optimization, the equations are not well-converged due to the domain being all-fluid. As the solid areas are formed in the domain, the equations display better convergence and so the computed sensitivities are more accurate driving the optimization to constantly lower objective function values. Additionally, in the beginning, the volume constraint described by eq. (5.1) is not satisfied meaning that the MMA updates the design variables so that a feasible solution to the problem be reached, without paying "so much attention" to the reduction of the objective function. In figs. 5.13b and 5.13c the mean outlet temperature and the volume-averaged total pressure losses objective (eq. (2.10)) respectively are plotted.
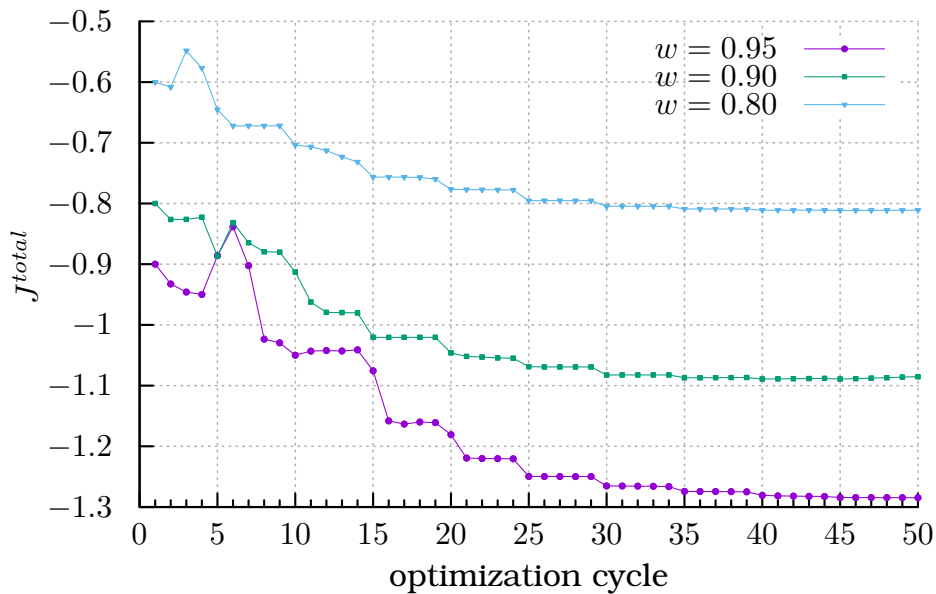
(a) Normalized total objective function for three weights.
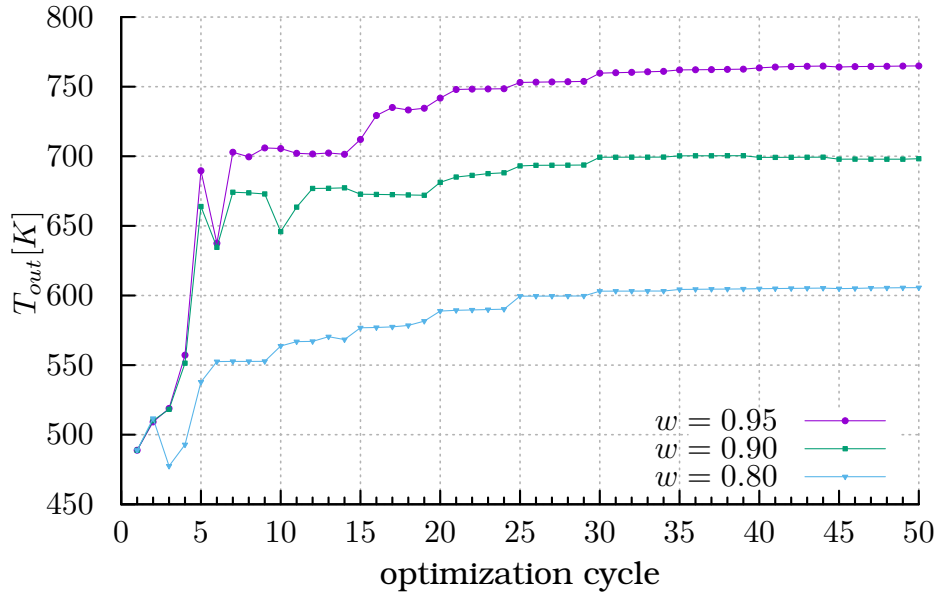
(b) Mean outlet temperature in each optimization cycle for three weights.
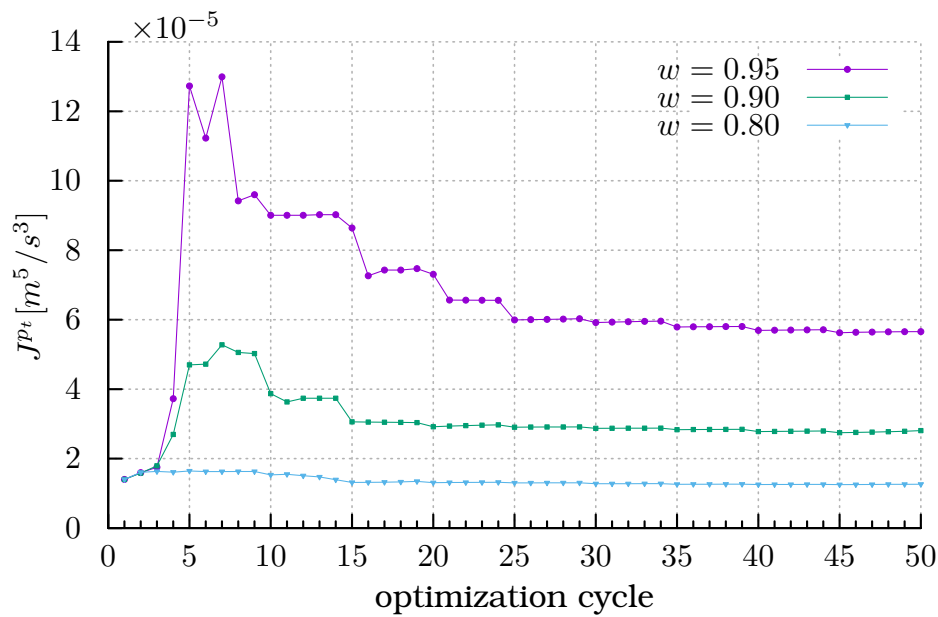
(c) Volume-averaged total pressure losses in each optimization cycle for three weights.

Figure 5.13: Convergence of the normalized total objective function as well as of each objective comprising it.

5.3.3 Optimization on the PM1 using dynamic TopO

In this section, TopO is conducted on the PM1 comprised of $\sim 120K$ cells using the dynamic TopO method discussed briefly in section 5.2. Four cases are run for different weights in the objective function eq. (2.8), starting from an all-fluid porosity field. The weights used are the same as the ones in section 4.5.

For the first 50 optimization cycles, a constant value of $b = 3$ is set in the

tanh function for the projection step. Additionally, a marching step is used, starting from the bottom of the domain and moving upward, which adds 40 new cell rows in the design space in each optimization cycle. After the tenth cycle, the whole design space becomes available for optimization. Then, another 50 cycles are run with the whole design space available and with a scaling value of the sharpening parameter, b, of the projection. Its value starts at $b = 2$ and with an increment of two for every ten optimization cycles, it ends at $b = 10$.

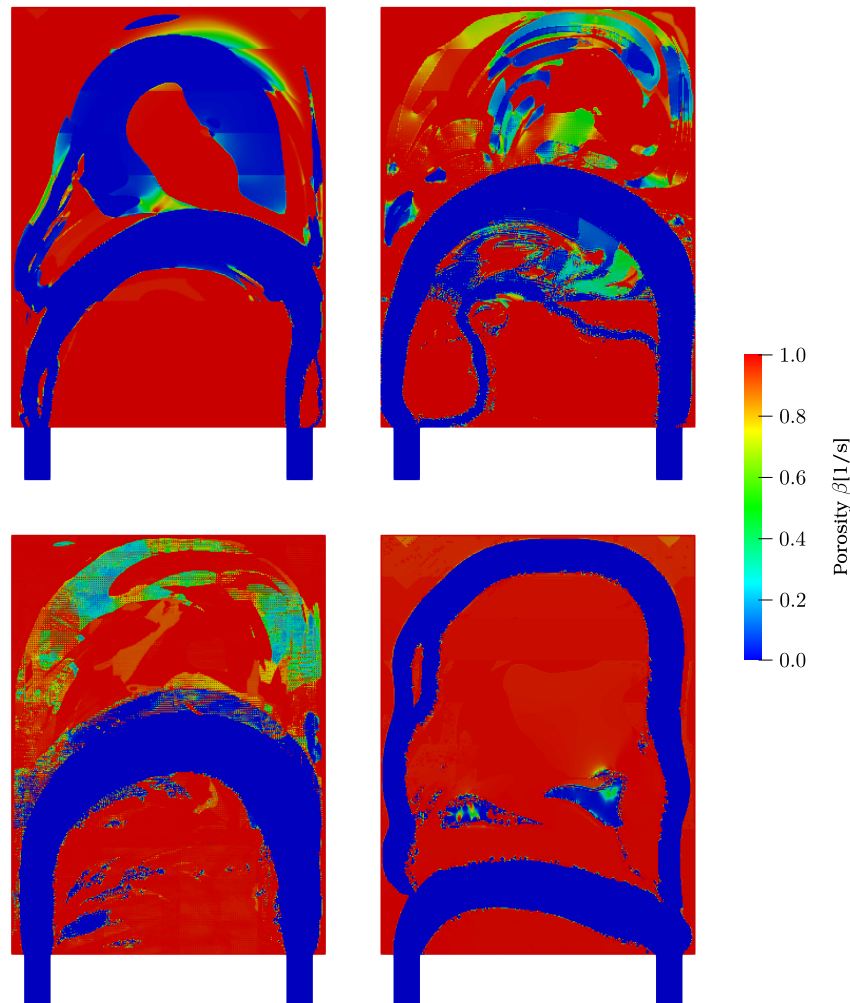The resulting porosity fields of the optimization are displayed in fig. 5.14.

Figure 5.14: Resulting porosity fields for different weights in the objective function, $w = 0.9$ (top left), $w = 0.8$ (top right), $w = 0.5$ (bottom left) and $w = 0.2$ (bottom right).

It can be observed that for the case with $w = 0.9$ parts of the domain are solidified near the outlet. This greatly contributes to the increase in the mean outlet temperature objective but also leads to an increase in the total pressure losses.

The mean outlet temperature, total pressure losses and FSI length are computed and shown in table 5.6.

w	T_{out}[K]	Δp_t[Pa]	FSI length[m]
0.9	731.1	0.964	0.946
0.8	593.2	0.283	1.250
0.5	450.5	0.086	0.687
0.2	415.3	0.074	1.316

Table 5.6: Outlet temperature, total pressure losses and FSI length for different weights in the objective function.

It should be noted that the increase in total pressure losses due to the extensions added at the inlet and outlet of the domain, is not incorporated in the results shown in table 5.6 and that the area-averaging of temperature is performed right before the outlet extension.

The temperature and velocity fields are also presented for the cases with the largest and the smallest w values. The temperature fields are shown in fig. 5.15 while the velocity fields are in fig. 5.16.
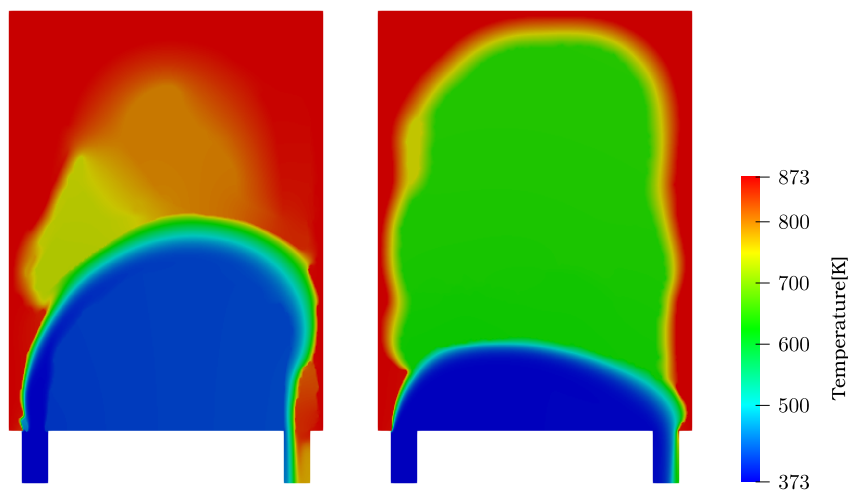

Figure 5.15: Resulting temperature fields for the cases with $w = 0.9$ (left) and $w = 0.2$ (right).
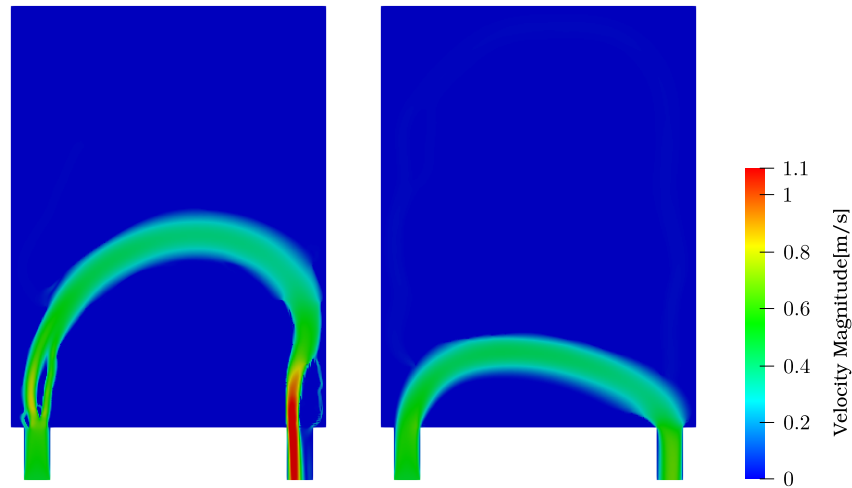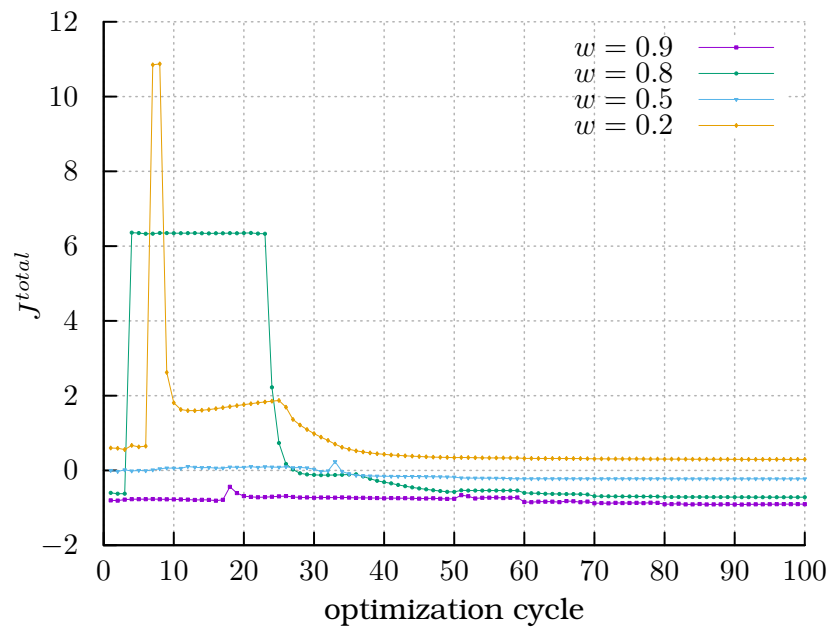
Figure 5.16: Resulting velocity fields for the cases with $w = 0.9$ (left) and $w = 0.2$ (right).

The J^{total} values in each optimization cycle for the four cases are plotted in fig. 5.17a. The values at every tenth optimization cycle of the mean outlet temperature as well as the total pressure losses are presented in fig. 5.17b and fig. 5.17c respectively.

(a) Normalized total objective function for four weights.
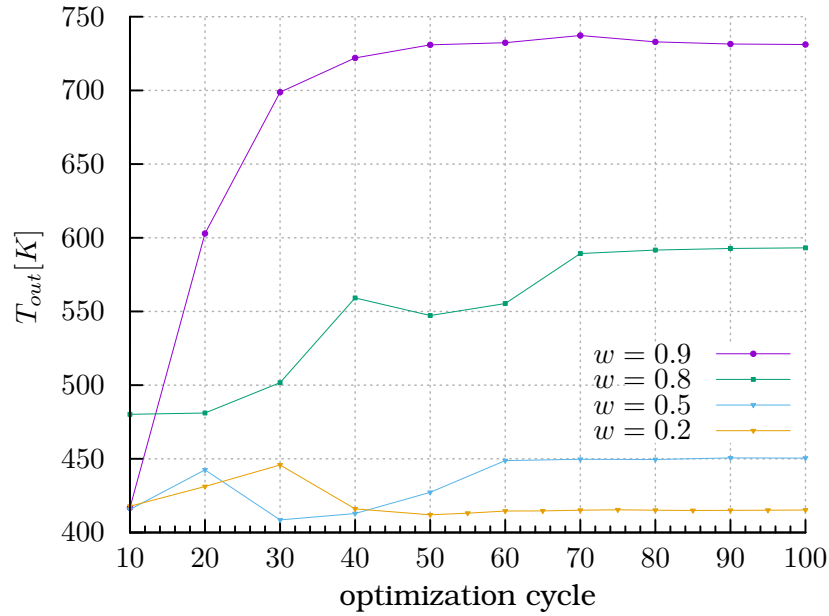
(b) Mean outlet temperature in every ten optimization cycles for four weights.
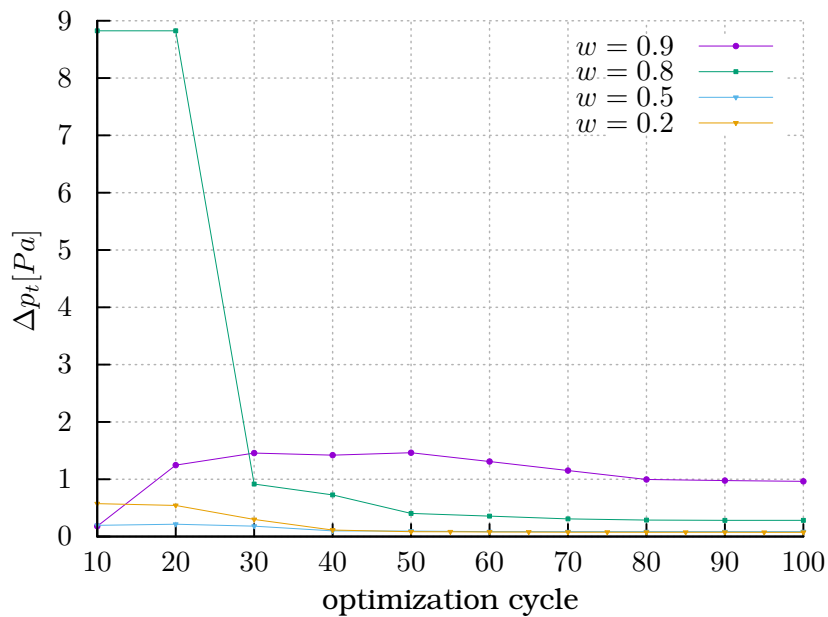
(c) Total pressure losses in every ten optimization cycles for four weights.

Figure 5.17: Convergence of the normalized total objective function as well as the values of mean outlet temperature and total pressure losses at every tenth optimization cycle.

5.4   Evaluation of the design produced with TopO

In sections 5.2 and 5.3.2, the geometries resulting from the TopO correspond to a U-shaped duct that approaches the heated walls as the value of w in the objective function increases. To evaluate the solution of the optimization, a

rough approximation of the geometry is designed and analyzed. At first, in section 5.4.1, the primal problem is solved using the **PBF2** solver. The same problem is, then, solved using the **PPB** solver and the results are compared with previous cases. Finally, in section 5.5 ShpO is performed on the design.

5.4.1 Primal solution on the U-shaped duct

The geometry used for the analysis is shown in fig. 5.18. The geometry is not an exact copy of the ones produced by TopO as it was arbitrarily designed and so an inconsistency in the results is to be expected.
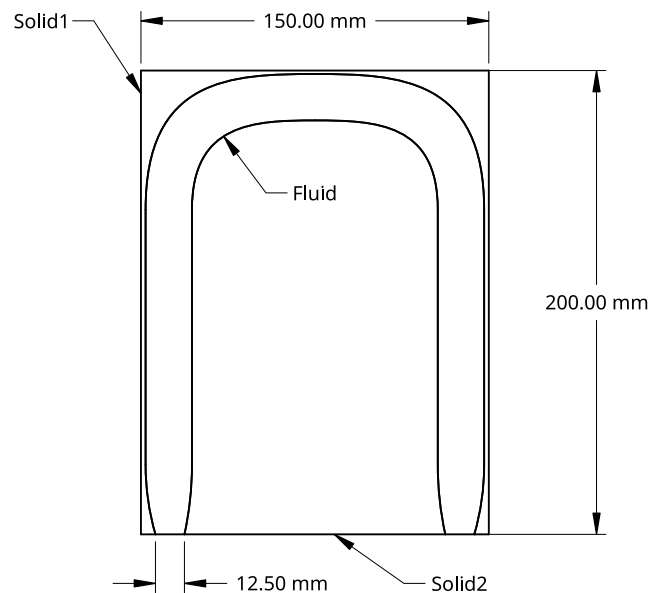

Figure 5.18: U-shaped duct geometry.

Additionally, the strange shape of the U-shaped duct is so that the percentage of fluid volume to the total volume of the domain is close to the upper bound set in the TopO (section 5.2). In the case of TopO, the volume percentage constraint is expressed by eq. (5.1) from which can be deduced that "grey" porosity areas contribute to the flow volume. Therefore, the newly designed duct is of larger width comparing it to the TopO results, nonetheless, there is consistency in the percentage of the volume occupied by the fluid in the domain.

The computational mesh used for the analysis is shown in fig. 5.19. This mesh is called BFM2 and is comprised of $\sim 16K$ cells in the fluid domain, $\sim 7.5K$ cells in the outer solid and $16K$ cells in the inner solid.
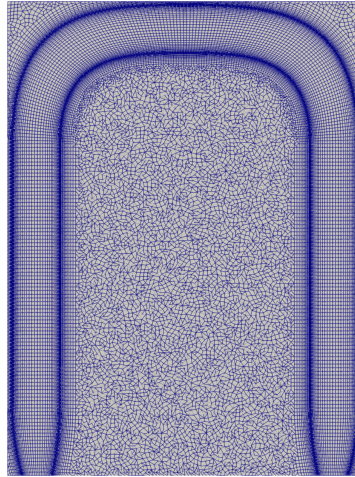
Figure 5.19: U-shaped duct mesh (BFM2).

The temperature and velocity field resulting from the CHT analysis of the U-shaped duct, are depicted in fig. 5.20.
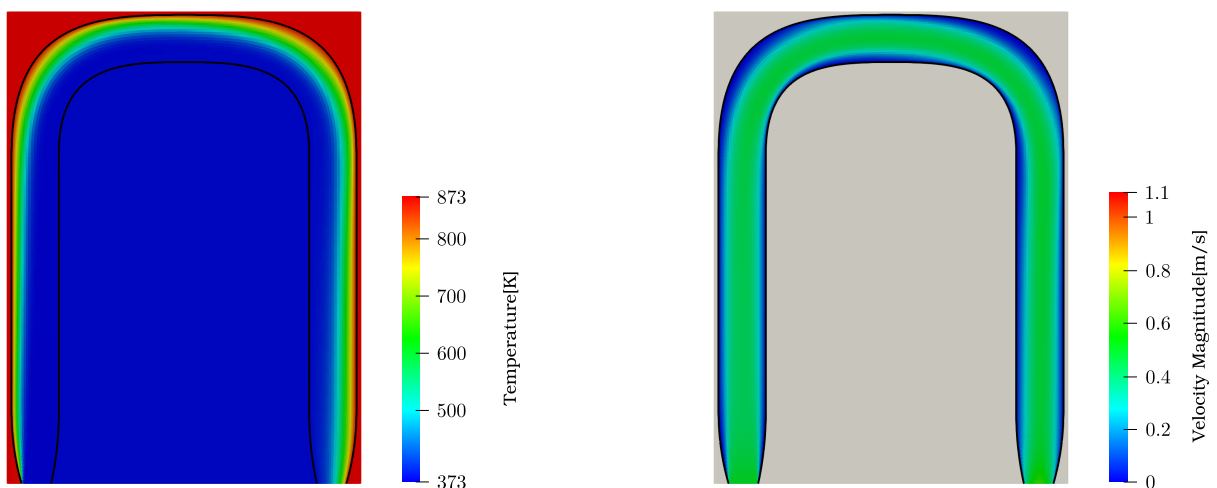

Figure 5.20: Temperature (left) and velocity magnitude (right) field computed using **PBF2**.

The computed mean outlet temperature is $T_{out} = 515.2\,\mathrm{K}$ while the total pressure losses are $\Delta p_t = 0.119\,\mathrm{Pa}$. Additionally, the FSI length computed is $0.934\,\mathrm{m}$. There is a great deviation in the results between this case and the ones presented in section 5.2 ($T_{out} = 747.7\,\mathrm{K}$, $\Delta p_t = 0.679\,\mathrm{Pa}$) and section 5.3.2 ($T_{out} = 698.2\,\mathrm{K}$, $\Delta p_t = 0.709\,\mathrm{Pa}$). A possible explanation is that this is caused due to solving the problems with different solvers. To examine this possibility, the same problem should be solved with the **PPB** solver.

5.4.2 Primal Problem solution using the PPB solver

In this section, the primal CHT problem is solved on the BFM2 mesh fig. 5.19 with the **PPB** solver in order to examine whether the porosity-based solver approach is the reason for the deviation of the results presented in the previous

section. The porosity field is set so that the cells that belong to the solid do-
main in the original problem (section 5.4.1) have a value of $\alpha = 1$ while the
others have zero value. The porosity field is depicted in fig. 5.21.
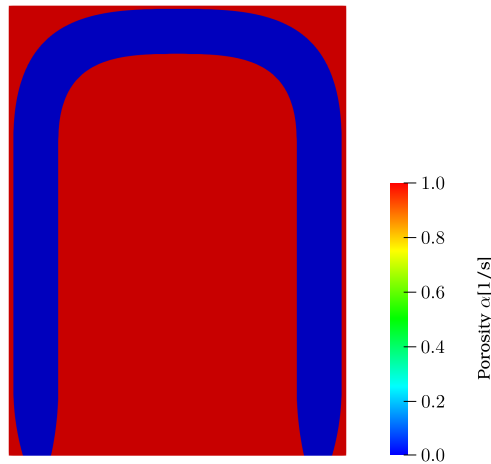

Figure 5.21: Porosity field representing the U-shaped duct geometry.

The resulting temperature and velocity fields are shown in fig. 5.22.
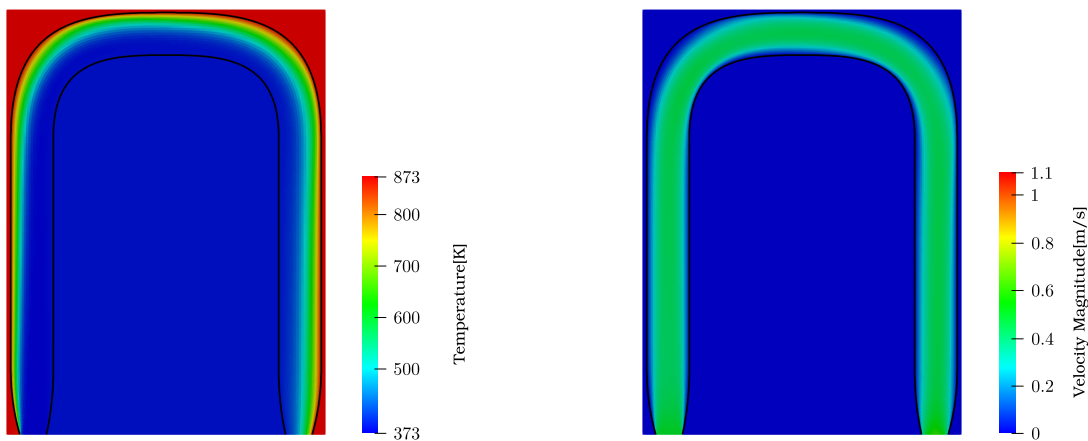

Figure 5.22: Temperature (left) and velocity magnitude (right) field computed
using the **PPB** solver.

The computed mean outlet temperature is $T_{out} = 524.5\,\text{K}$ while the total
pressure losses are $\Delta p_t = 0.132\,\text{Pa}$. Although the results do not differ noticeably
between this analysis and the one of the previous section (section 5.4.1) this is
not the case in comparison with the other two in sections 5.2 and 5.3.2. The
computed outlet temperature in this case is much lower and as are the total
pressure losses.

In both the previous cases, TopO tends to block the outlet by solidifying
some of the cells. Considering that the conductivity of the solid is greater than
the fluid's, the temperature value in those cells is higher than in the fluid cells.
The averaging of temperature includes cells of any type irrespective of whether
they are solid or fluid meaning that the mean outlet temperature is greatly
increased by the blocking of the outlet. Since this geometry detail is not taken
into account when designing the U-shaped duct geometry (fig. 5.18), mostly

because it negatively affects the second objective linked to the total pressure losses, the mean fluid outlet temperature of this geometry results to a much lower value.

Finally, in this section, the primal problem is solved on a strictly binary porosity field in which the FSI boundary is clearly defined. This is not the case in sections 5.2 and 5.3.2 where "grey" areas form on the FSI and thus the accuracy of the computations is compromised.

5.5 Shape optimization of the U-shaped duct

Four optimization cases are run with the weights used in section 4.5. Every case is run for 10 optimization cycles. The optimized geometries for the two extreme cases with $w = 0.9$ and $w = 0.2$ are shown in fig. 5.23 on top of the initial geometry.
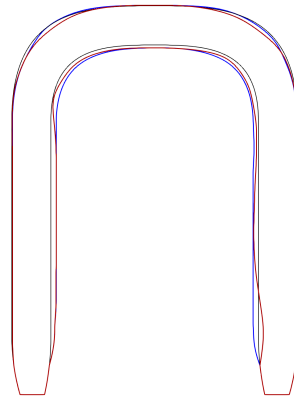

Figure 5.23: The red line corresponds to the geometry produced for $w = 0.9$, the blue for $w = 0.2$ and in black is the original U-shaped duct geometry.

The mean fluid temperature at the outlet, total pressure losses and FSI length computed in each case are presented in table 5.7 for all the weights studied.

w	T_{out}[K]	Temperature increase	Δp_t[Pa]	Losses decrease	FSI length[m]
0.9	512.9	$-0.44\,\%$	0.109	$8.81\,\%$	0.926
0.8	507.6	$-1.46\,\%$	0.100	$16.13\,\%$	0.923
0.5	506.7	$-1.65\,\%$	0.099	$16.76\,\%$	0.924
0.2	506.4	$-1.70\,\%$	0.099	$16.80\,\%$	0.924

Table 5.7: Outlet temperature, total pressure losses and FSI length for different weights in the objective function.

The normalized total objective function convergence is plotted in fig. 5.24a. Moreover, the values in each optimization cycle of the mean outlet temperature as well as the total pressure losses are presented in figs. 5.24b and 5.24c, respectively.
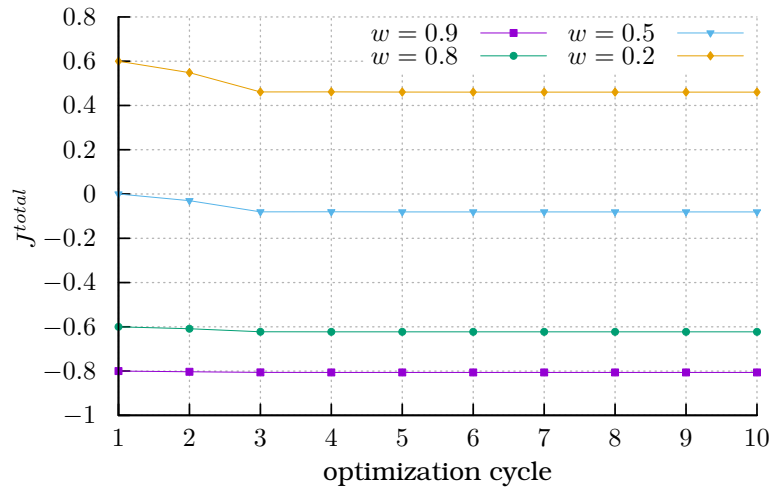
(a) Normalized total objective function for four weights.
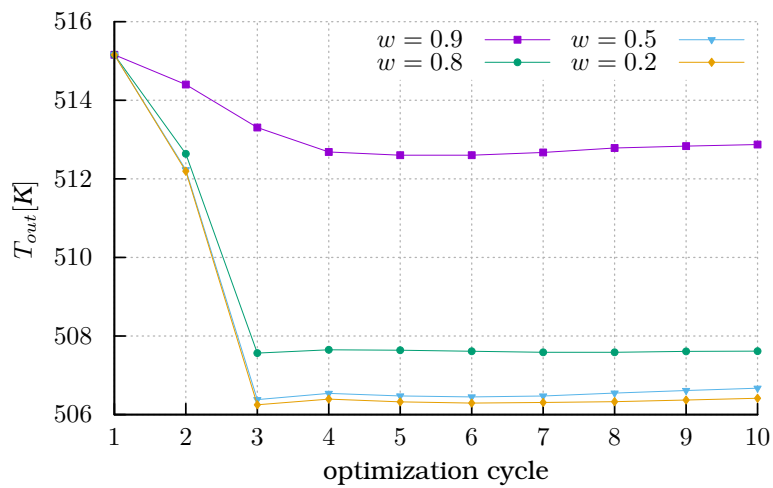
(b) Mean outlet temperature in each optimization cycle for four weights.
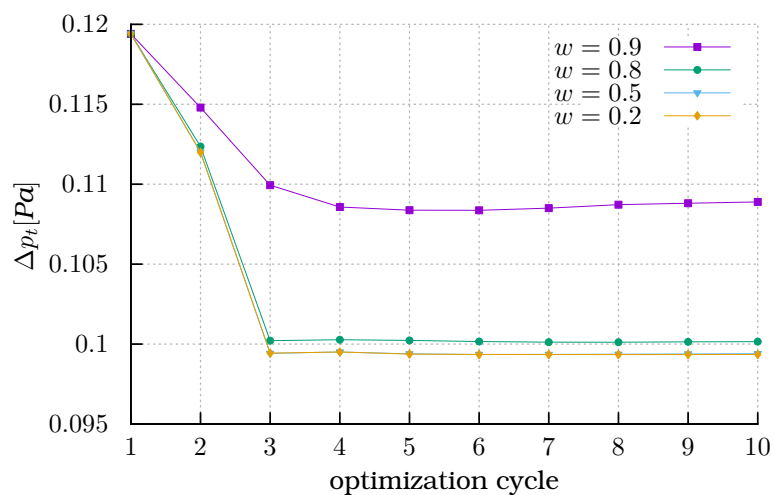
(c) Total pressure losses in each optimization cycle for four weights.

Figure 5.24: Convergence of the normalized total objective function as well as of each objective constituent of it.

For $w = 0.9$, almost no drop in the value of the objective function is observed, while for $w = 0.2$ decrease is higher. This is due to the optimization being able to lower the total pressure losses, the contribution of which is more significant in the objective function for the case with $w = 0.2$. The optimization is unable to increase the fluid outlet temperature for the current parameterization. Finally, it can be deduced that the initial design was already close to optimal and thus, the optimization converged in two to three cycles.

5.6 Conclusions

In this chapter, the test case introduced in chapter 4 was studied using a porosity-based solution approach. The results showed that despite the omission of boundary conditions on the FSI, the flow behavior can be adequately captured by the additional porosity-dependent source terms in the flow equations for TopO (eqs. (3.1)). The results and the convergence of the problem, are dependent on the β_{max} value which controls the permeability of the solidified areas. A higher β_{max} value increases the accuracy of the results since the FSI boundary conditions are more "strictly" imposed (e.g. flow velocity better approaches zero on the FSI).

As indicated by figs. 5.3 and 5.4, the absence of boundary conditions mostly affects the results for temperature near the inlet. In the typical solution approach used for ShpO (section 2.1) a Dirichlet condition is imposed on temperature that enforces temperature equality and heat-flux conservation at the FSI. On the other hand, in the porosity-based approach, only the heat-flux conservation condition is imposed through eqs. (3.1), whereas the temperature equality is not. Nonetheless, with the settling of the flow, the differences in the temperature field become smaller.

TopO was run on the BFM1 mesh for different weights in the objective function. The resulting geometries are shown in fig. 5.5 and correspond to a U-shaped duct. When the maximization of the outlet temperature is of greater importance, the resulting duct goes up to the heated domain walls. Moreover, a solid area is formed near the outlet which additionally helps with the flow temperature rise. On the other hand, when the prevailing objective is the minimization of total pressure losses, a U-shaped duct of smaller length is formed. Also, its width is bigger leading to smaller velocity magnitudes which, in turn, causes lower total pressure losses.

Moreover, a structured mesh was generated (fig. 5.9-left) as typically used in TopO cases. Straight extensions were added to the inlet and outlet of the domain so that the flow velocity profile is developed before it enters and exits the domain. At first, a mesh independence study was conducted that concluded to the adequate mesh resolution. After that, several TopO cases were run for different weights in the objective function. All the designs resulted in a U-shaped duct geometry. The mean outlet temperature and total pressure losses of the designs are summarized in table 5.5. To obtain a more intricate design from the TopO, the dynamic TopO method was used (explained in section 5.2). The resulting geometries can be seen in fig. 5.14.

In section 5.4, the design produced by TopO in sections 5.2 and 5.3.2 was

evaluated. An approximate design of the U-shaped duct was created which resembles, but is not the same as, the ones produced with TopO. Solving the primal problem with the **PBF2** solver, a great divergence in the results was observed. To examine whether this was caused due to the difference in the solver, the same problem was solved using the porosity-based approach. Again, the difference in the results was significant which is attributed to two reasons. The first one is errors in the approximate design of the U-shaped duct which differs from the ones created by TopO. The second and most important reason is accredited to the well-known disadvantage of the porosity-based TopO which is the absence of FSI. The porosity field used in section 5.4.2 is strictly binary meaning that there is a well-defined boundary separating the flow from the solid. On the contrary, in sections 5.2 and 5.3.2 many "grey" areas are formed in the porosity fields which causes large inaccuracies in the results since there are no proper conditions imposed between the region interfaces.

Chapter 6

Revisiting Previous Conclusions on a 2D Duct System

In this chapter, some of the assumptions drawn in previous chapters are revisited on a second test case regarding the design of a 2D duct system. At first, several TopO cases are run for different settings of the code. Then, a utility created by the PCOpt/NTUA based on the OpenFOAM©framework is used to create body-fitted mesh for both the fluid and solid regions based on the background mesh of TopO and the optimal porosity field produced by TopO. Finally, ShpO is run on the body-fitted mesh and the results for different weights in the objective function are discussed.

6.1   Problem Description

The geometry created as test case 2 is shown in section 6.1. The boundaries S_{I_1}, S_{I_2} are the two inlets while the S_O boundary is the outlet.
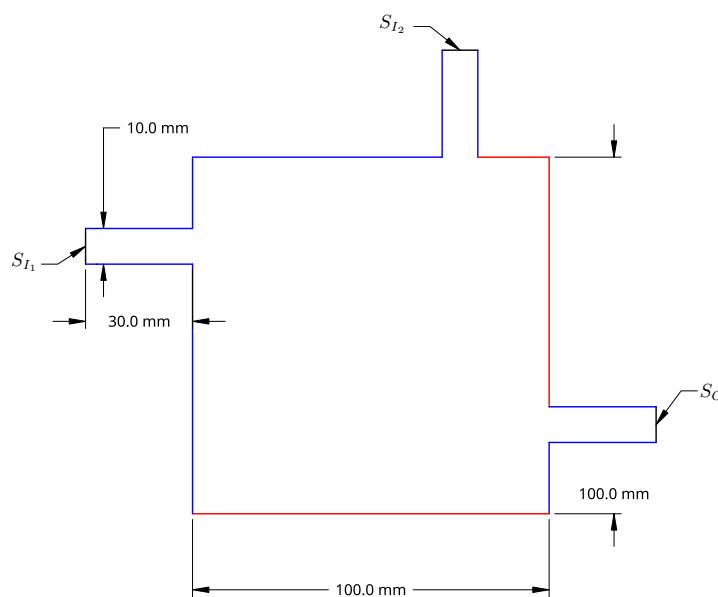

Figure 6.1: Geometry for test case 2. Red color is used to indicate hot walls and blue for adiabatic walls.

The fluid enters the domain with a velocity magnitude of $|v| = 0.01\,\mathrm{m/s}$ and with temperature $T = 293\,\mathrm{K}$. The fluid is water with kinematic viscosity $\nu = 1 \times 10^{-6}\,\mathrm{m^2/s}$, density $\rho^F = 998.2\,\mathrm{kg/m^3}$, specific heat capacity at constant pressure $c_p^F = 4180\,\mathrm{J/(kgK)}$ and thermal conductivity $k^F = 0.598\,\mathrm{W/(mK)}$. All its thermophysical properties are considered constant. The flow is laminar with $Re = 100$. The heated walls of the domain are kept at $T = 353\,\mathrm{K}$. Finally, the solid thermal conductivity is set as previously to $k^S = 12.7\,\mathrm{W/(mK)}$.

The mesh created for this case is structured and is composed of $\sim 25K$ cells. It can be seen in fig. 6.2 and will be called PM2.
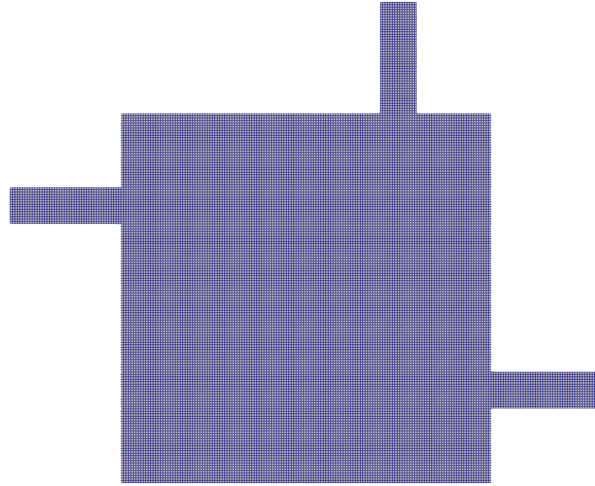

Figure 6.2: Computational mesh for test case 2 (PM2).

Again, straight extensions are added at the outlet and both inlets of the domain, so that the flow profile has been developed before the fluid enters the design space and the boundary conditions at the outlet are properly imposed. It should be noted that the extensions do not participate in the optimization and the porosity field has constantly zero value in those areas of the mesh.

6.2 TopO of the 2D duct system

The objective function used in the optimization is comprised of two objectives. The first objective is the minimization of the mean temperature in the domain while the other one is the minimization of the volume-averaged total pressure losses. The objective function is expressed as,

$$J^{total} = w\hat{J}^{meanT} + (1-w)\hat{J}^{p_t} \tag{6.1}$$

where $w \in [0,1]$ is a weight used to control the contribution of each objective in the total objective function. The hat symbol is used to indicate that the two objectives are normalized. Each objective is normalized with its value at the start of the optimization.

The volume-averaged temperature objective is computed by

$$J^{meanT} = \frac{\int_\Omega T d\Omega}{\int_\Omega d\Omega} \tag{6.2}$$

while the total pressure losses objective is given by eq. (2.10). Additionally, a constraint for the percentage of fluid volume in the domain as in eq. (5.1) is set. The fluid volume is kept lower than 0.4 of the total volume of the domain.

The β_{max} value used throughout the optimization is given by eq. (3.5) for $Da = 10^{-5}$ specifically, $\beta_{max} = 1000$. For the interpolation of thermophysical properties between the fluid and solid regions based on the scheme described by eq. (3.3), the SIMP function is used eq. (3.4) with $b = 3$. The Helmholtz PDE (eq. (3.6)) is employed for the regularization of the porosity field with $R \approx 0.0033$ m and eq. (3.7) is used for the projection. In particular, the parameter b controlling the steepness of the projection starts at $b = 3$ and is increased by 3 every 10 optimization cycles. The optimization is run for a total of 50 cycles.

TopO is run for four different weights in the objective, the same as those in section 4.5. The domain is all-fluid at the beginning of the optimization. The geometries designed by TopO are shown in fig. 6.3.
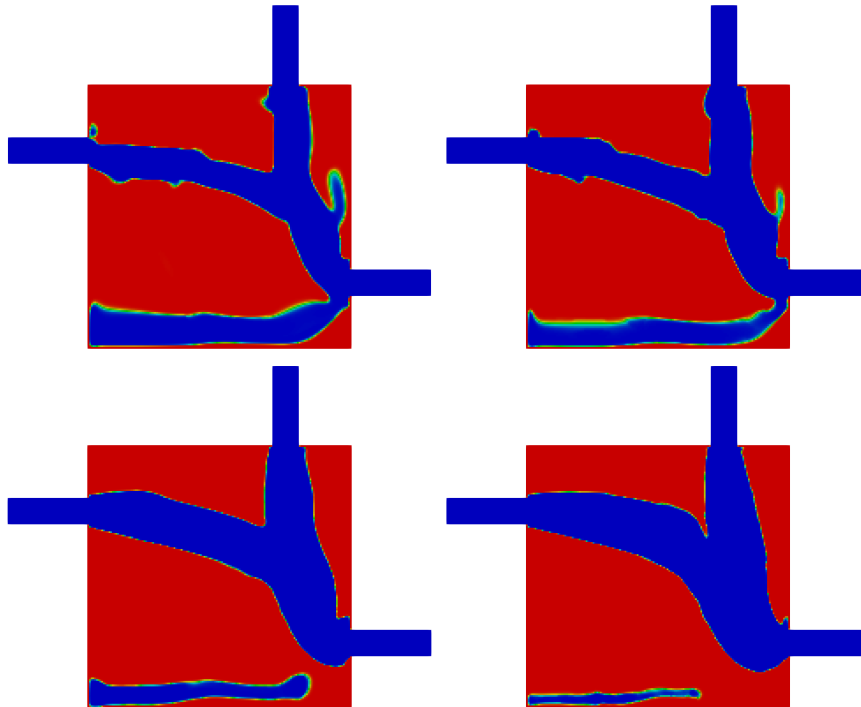
Figure 6.3: Resulting porosity fields for $w = 0.9$ (top-left), $w = 0.8$ (top-right), $w = 0.5$ (bottom-left), $w = 0.2$ (bottom-right).

The most obvious difference in the designs is the volume of the cavity of fluid, formed near the bottom wall. Specifically, as the value of w drops and so the significance of the temperature objective is lowered, the volume of the cavity decreases. This is because the cavity acts as thermal insulation preventing the heat from transferring further inside the domain. The thermal conductivity of water is far less than the solid's which means that the presence of stagnant flow along the width of the heated wall, reduces the diffusion of heat inside the domain. Conversely, for lower values of w the cavity volume is smaller but the width of the duct is larger allowing for lower total pressure losses.

In fig. 6.4, the temperature fields are shown for the cases with $w = 0.9$ and $w = 0.2$.
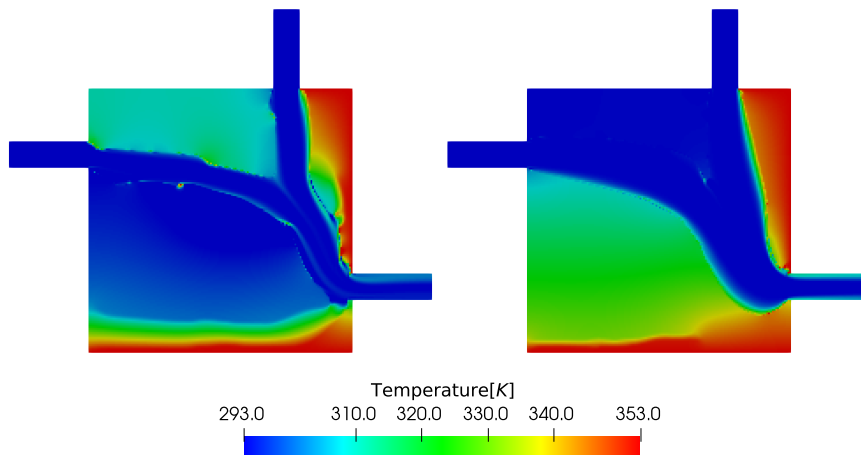
Figure 6.4: Resulting temperature fields for $w = 0.9$ (left) and $w = 0.2$ (right).

The velocity magnitude fields for the same cases are shown in fig. 6.5.
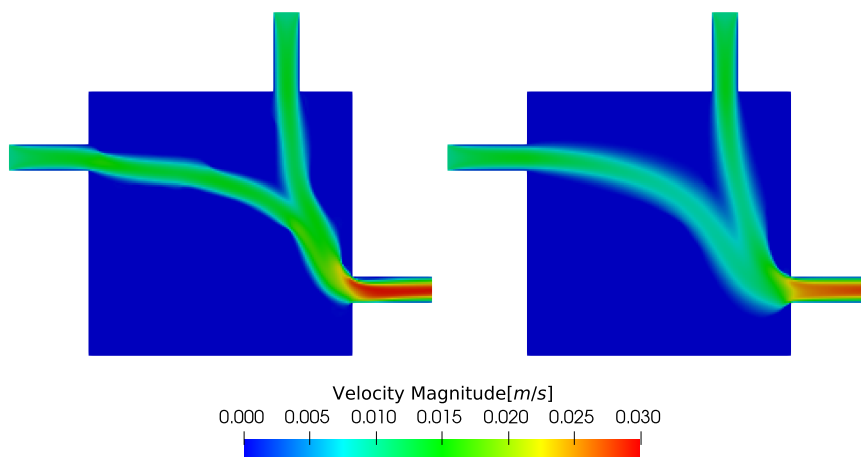
Figure 6.5: Resulting velocity magnitude fields for $w = 0.9$ (left) and $w = 0.2$ (right).

It is obvious from the temperature field in fig. 6.4-left, that the cavity manages to thermally isolate the hot bottom wall from the rest of the domain and therefore decrease its mean temperature contrary to fig. 6.4-right where the cavity is smaller. On the other hand, the wider duct that resulted for $w = 0.2$ presents smaller velocity magnitudes in the flow as shown in fig. 6.5-right which, in turn, decreases the total pressure losses.

In fig. 6.6 the normalized total objective function, the volume-averaged temperature and the total pressure losses coefficient are plotted respectively.
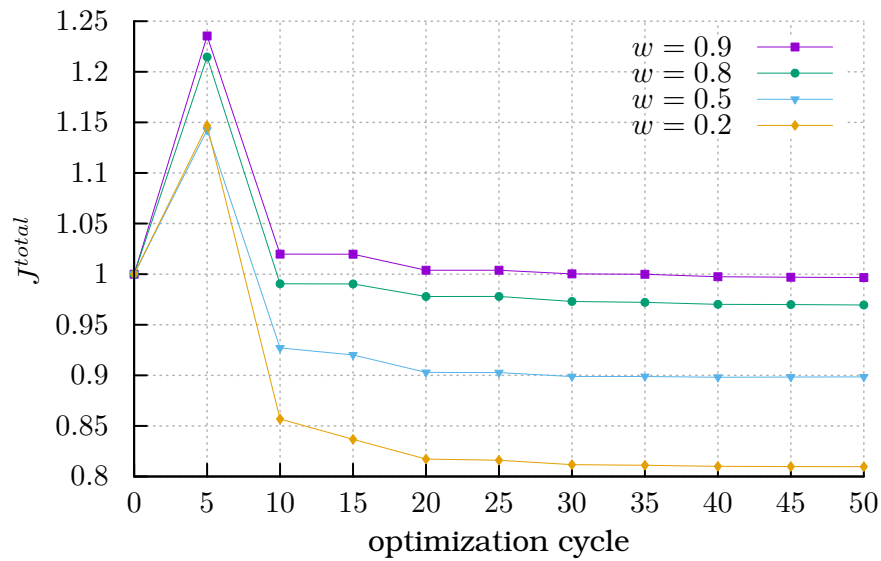
(a) Normalized total objective function for four weights.
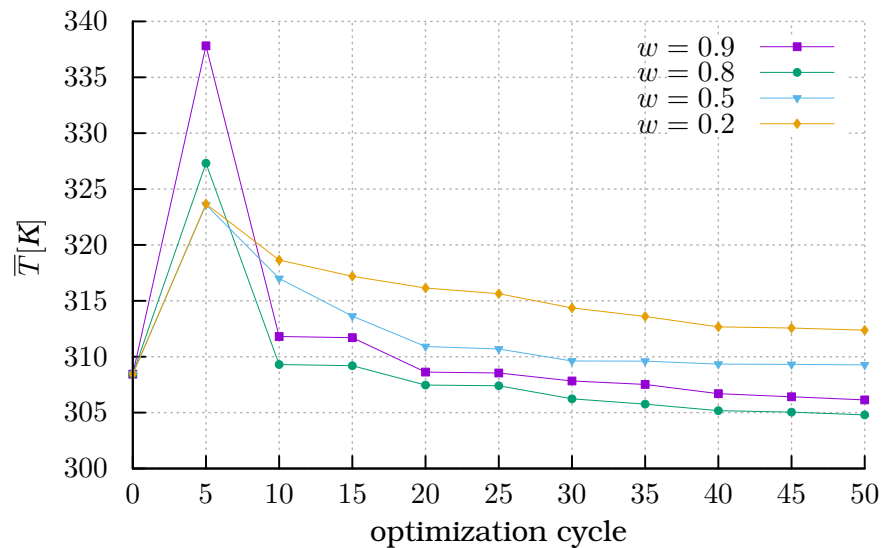
(b) Mean outlet temperature in each optimization cycle for four weights.
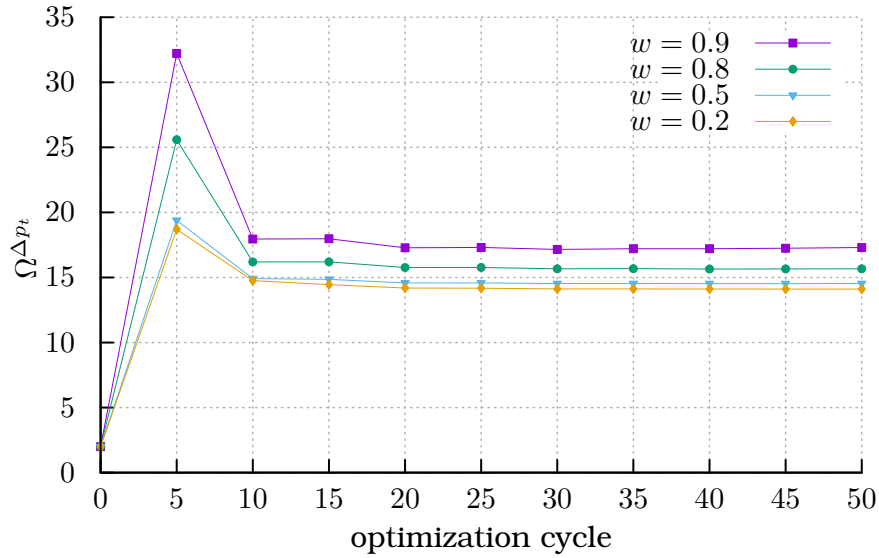
(c) Total pressure losses in each optimization cycle for four weights.

Figure 6.6: Convergence of the normalized objective function as well as of each objective constituent of it.

The total pressure losses coefficient is defined as the total pressure losses divided by the dynamic pressure at the inlet, namely,

$$\Omega^{\Delta p_t} = \frac{\Delta p_t}{1/2 \rho v^2} \tag{6.3}$$

It can be observed that the objectives begin to decrease after the fifth cycle. This is because the optimization starts with an all-fluid domain, which is an infeasible solution to the problem based on the volume constraint that has been set. Once a feasible solution has been reached, the value of the objectives starts to decrease. A great drop in the J^{total} value is achieved after the fifth cycle. The value of the volume constraint during the optimization is shown in fig. 6.7.
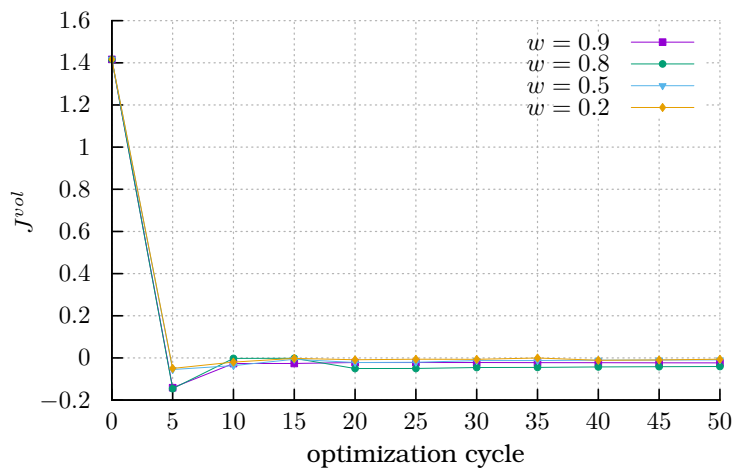
Figure 6.7: Normalized percentage of fluid volume in the domain during the optimization.

Finally, in table 6.1, the volume-averaged temperature in the domain and the total pressure coefficient for the resulting geometries are presented.

w	$\overline{T}[\mathrm{K}]$	$\Omega^{\Delta p_t}$
0.9	306.1	17.3
0.8	304.8	15.7
0.5	309.3	14.5
0.2	312.4	14.1

Table 6.1: Volume-averaged temperature and total pressure losses coefficient for different weights in the objective function.

6.3   TopO to ShpO Transition

In this section, a utility created by the PCOpt/NTUA is used to create body-fitted meshes for both the solid and fluid regions of the TopO case presented in the previous section for $w = 0.5$. The body-fitted meshes are generated based on the optimal porosity field shown in fig. 6.3-(bottom-left) and the PM2 mesh fig. 6.2 and are demonstrated in fig. 6.8.

Figure 6.8: Body-fitted meshes created from PM2 based on the optimal porosity field for $w = 0.5$. Body-fitted mesh for the fluid region (left) and the solid region (right).

Solving the primal problem with the **PBF2** solver on the body-fitted mesh, the resulting mean temperature in the domain is $\overline{T} = 309.1\,\mathrm{K}$ (instead of $\overline{T} = 309.3\,\mathrm{K}$) and the total pressure losses coefficient $\Omega^{\Delta p_t} = 14.3$ (instead of $\Omega^{\Delta p_t} = 14.5$) which are almost identical to the results produced by TopO for $w = 0.5$.

For the ShpO of the geometry, the first objective is slightly different than the one used in TopO, as it expresses the minimization of the mean temperature in the solid region rather than the entire domain. Nonetheless, the results are processed so that the mean temperature in the entire domain is computed and there can be a comparison with the results from the previous section.

Again, the FSI boundary is parameterized using a VBS morpher. The control box is composed of 11×11 control points shown in fig. 6.9.
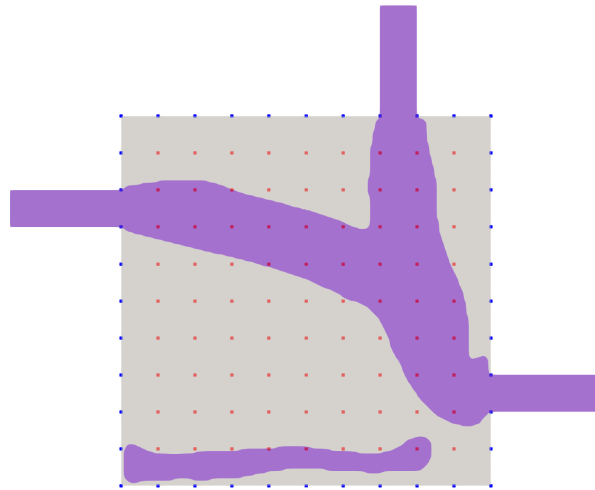
Figure 6.9: A 11×11 VBS box parameterizing the FSI. CPs in blue remain fixed and red ones are allowed to move.

The geometries formed by ShpO after 10 optimization cycles for the four weights are almost identical. In fig. 6.10, the geometries are shown on top of the initial design.
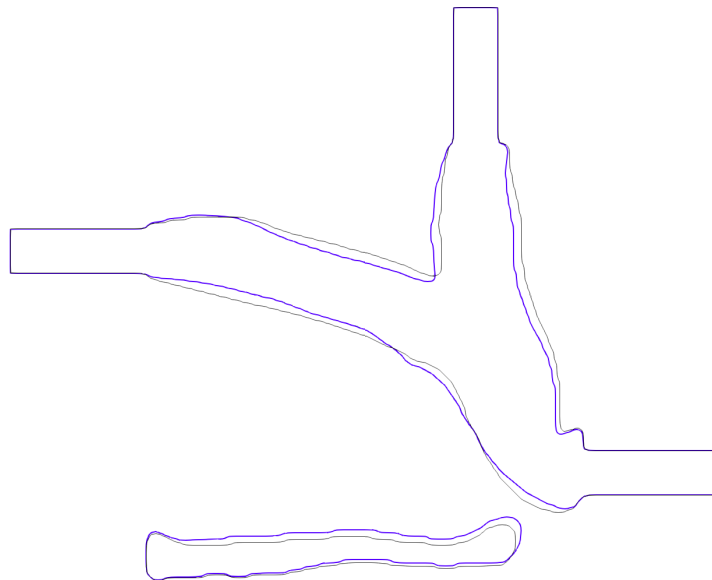
Figure 6.10: The geometry produced by the four different ShpO cases is in blue, while in black is the original geometry.

The optimized duct is narrower than the original and the volume of the cavity has slightly increased. The values in each optimization cycle of the volume-averaged temperature in the domain as well as the total pressure losses coefficient are plotted in figs. 6.11a and 6.11b respectively.
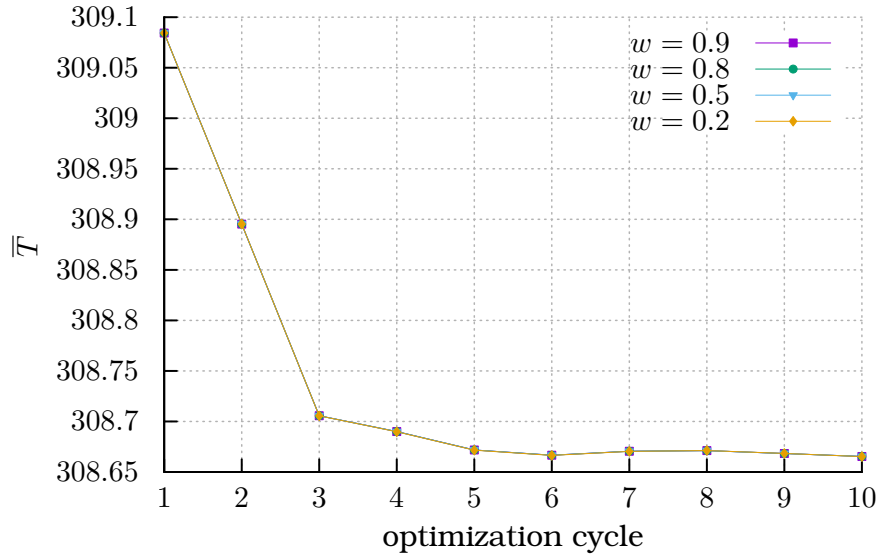
(a) Mean outlet temperature in each optimization cycle for four weights.
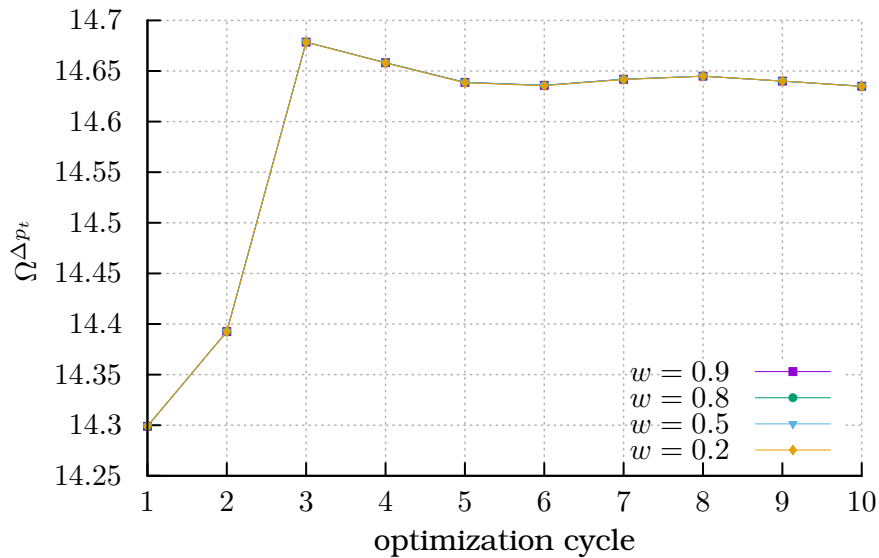
(b) Total pressure losses coefficient in each optimization cycle for four weights.

Figure 6.11: Convergence of the objective for different weighs.

The convergence of the objective for all the cases is almost the same. A slight increase in the total pressure losses objective caused by the narrowing of the duct and a small decrease in the average temperature caused by the enlargement of the cavity is observed. The similarity in the results for different weights and the fact that ShpO is unable to further decrease the total pressure losses indicates that the design produced by TopO is already close to optimal, meaning that the optimization is already close to a local minimum.

In table 6.2, the results for the original and the optimized geometries are presented.

	$\overline{T}[\mathbf{K}]$	$\Omega^{\Delta p_t}$
original	309.1	14.3
optimized	308.7	14.6

Table 6.2: Volume-averaged temperature and total pressure losses coefficient for the original and optimized geometries.

6.4 Conclusions

In this chapter, TopO is run on a second test case where the fluid (water) enters the domain from the left and top side and exits from the right. The objective is to minimize the volume-averaged temperature in the domain as well as the total pressure losses. Starting for an all-fluid domain, the geometries produced by TopO are presented in fig. 6.3 for different weights in the objective function. The formation of a cavity near the hot bottom wall, which acts as thermal insulation preventing heat transfer to the rest of the domain, can be seen. With the increase in w and hence the significance of the mean temperature objective, the cavity becomes larger and the duct's width becomes smaller. Since there is a constraint imposed on the percentage of fluid inside the domain, the increase in the cavity volume is compensated by the narrowing of the duct.

A utility created by the PCOpt/NTUA is used to create a body-fitted mesh for the fluid and the solid based on the background mesh of TopO and the optimal porosity field produced for $w = 0.5$ shown in fig. 6.8. The geometry is reevaluated using the **PBF2** solver and the results are very close to the ones produced by TopO namely, the computed mean temperature in the domain is $\overline{T} = 309.1\,\mathrm{K}$ (instead of $\overline{T} = 309.3\,\mathrm{K}$) and the total pressure losses coefficient is $\Omega^{\Delta p_t} = 14.3$ (instead of $\Omega^{\Delta p_t} = 14.5$).

Finally, ShpO is run on the body-fitted mesh for different weights and the results are almost the same in each case. The optimization managed to slightly decrease the mean temperature while on the other hand, the total pressure losses were slightly increased. The small impact of ShpO on the design indicates that the geometry was near-optimal from the start and the TopO result was already close to a local minimum.

Chapter 7

Closure-Conclusions

The purpose of this thesis was the study of the continuous adjoint method for CFD-based optimization of problems including CHT. Steady-state laminar flows of incompressible fluids were studied and both ShpO and TopO were conducted on 2D cases. The relevant software has been programmed by the PCOpt/NTUA based on the open-source CFD toolbox OpenFOAM$^©$. In the next paragraphs, the conclusions drawn from each chapter are summarized.

- In Chapter 4, a CHT analysis was conducted on a test case inspired by an internally cooled turbine blade. A comparison was made between the results computed by the publicly available OpenFOAM$^©$solver for compressible flows and the ones by the incompressible solver developed by the PCOpt/NTUA. Both solvers gave similar results summarized in table 4.2. After that, the incompressible solver was used to optimize the shape of the serpentine-like duct. The ShpO objectives were the maximization of the fluid mean outlet temperature (multiplied by w) and the minimization of total pressure losses (multiplied by $(1 - w)$). Runs were performed for several weight values in the objective function and the results showed a 2.43% increase in the outlet fluid temperature for the case with $w = 0.95$ and a 17.67% decrease of total pressure losses for the case with $w = 0.2$. The duct geometries produced by ShpO became wavy for larger values of w, reinforcing the transfer of heat from the solid to the fluid region through extended separation areas and longer FSI. The opposite was observed for lower w values.

- In Chapter 5, the serpentine-like duct was studied using the primal solver of the TopO. At first, a study was conducted for the independence of the results on the value of the β_{max} parameter controlling the permeability of solids. Then, a comparison was made between the results of this solver and the **PBF2** which showed that despite the absence of BCs on the FSI, the flow behavior can be adequately captured by the porosity-dependent source terms in the flow equations. A slight difference in the results of the two solvers was observed near the FSI and mainly close to the inlet. In section 5.2, TopO was run on the BFM1 mesh, resulting in a U-shaped duct geometry. With the increase in the w value, the duct comes closer to the hot walls of the domain while for smaller values, the duct length decreases and its width becomes larger. Also, TopO solidifies parts of the

68

domain near the outlet in order to increase the fluid outlet temperature. A fully-structured mesh (PM1) is created as used typically in TopO since the geometry is unknown. TopO runs on PM1 also resulted in a U-shaped duct geometry and thus, a rough approximation of the geometry was designed and evaluated. The study showed significant deviation from the previous TopO cases, which is contributed primarily to the known disadvantage of TopO namely, the formation of "grey" areas in the porosity field.

- In Chapter 6, a second test case was studied regarding the design of a 2D duct system. The objective of the TopO was to minimize the volume-averaged temperature in the domain and the total pressure losses. Several runs were made for different weights in the objective function and the optimization formed a cavity near the hot bottom wall which acted as thermal insulation preventing the heat from transferring to the rest of the domain. With the increase in w and hence the significance of the mean temperature objective, the cavity became larger and the duct's width became smaller compensating for the constraint imposed on the percentage of fluid in the domain. Then a utility developed by the PCOpt/NTUA was used to generate a body-fitted mesh for the fluid and the solid based on the background mesh of TopO and the optimal porosity field produced for $w = 0.5$. The analysis showed that the results of the primal solver **PBF2** were very close to the ones computed by the TopO. Finally, ShpO was run on the body-fitted mesh, which resulted in approximately the same geometries for all the weights used. The optimization managed to decrease the mean temperature by 0.13% from the TopO design while the total pressure losses were slightly increased by 2.1%. The small impact of ShpO on the design indicates that the geometry was near-optimal from the start and the TopO result was already close to a local minimum.

As a general overview, ShpO is a widely used design method in CFD-based optimization and its effectiveness is demonstrated here in problems involving CHT. Many of the TopO cases conducted in this thesis resulted in geometries with blockages and broken flow paths as well as other non-physical artifacts especially when the thermal objective function was more prioritized. Additionally, it was observed that TopO encounters numerical difficulties towards convergence specifically in high Reynolds number laminar flows where steep gradients and small-scale phenomena appear, for example, flow separation. For instance, the numerical verification of topology-optimized geometries in the first application with $Re = 417$ revealed differences in the objective values reported by the body-fitted solver. Conversely, a similar study conducted for the second application with $Re = 100$ demonstrated excellent convergence of the results. Despite the aforementioned problems of TopO, the formed geometries exhibited characteristics attributable to the diverse physics at play. Moreover, certain designs leverage complex features that can be perceived as an innovative foundation for constructing an engineering solution to address the tackled problem.

To sum up, the primary focus of this thesis was to apply topology optimization in order to investigate novel and unconventional optimal designs for ther-

mal systems. In this undertaking, an assortment of code configurations was subjected to rigorous testing, yielding useful insights applicable to individuals employing similar codebases. The cases setup also involved the generation of meshes, employing the Pointwise software for body-fitted meshes and the blockMesh utility for TopO meshes which is provided with OpenFOAM$^{©}$. A large part of the post-processing was made using the ParaView software and some using functions already available with OpenFOAM$^{©}$. Finally, some utilities were programmed based on the OpenFOAM$^{©}$framework for the computation of the FSI length and the heat-flux through a boundary patch.

Appendix A

VBS as a Parameterization and Mesh Displacement Tool

The VBS mesh displacement method uses a mesh of CPs enclosing (part of) the domain. Let b_m^{ijk}, $m \in [1,3]$, $i \in [0,I]$, $j \in [0,J]$, $k \in [0,K]$ be the Cartesian coordinates of the i, j and k-th CP of the $3D$ structured control mesh and $I+1$, $J+1$, $K+1$ are the number of CPs per control mesh direction. The Cartesian coordinates $\mathbf{x} = (x_1, x_2, x_3)^T = (x, y, z)^T$ of a CFD mesh point residing within the boundaries defined by the control mesh are given by

$$x_m(u,v,w) = \sum_{i=0}^{I} \sum_{j=0}^{J} \sum_{k=0}^{K} U_{i,pu}(u) V_{j,pv}(v) W_{k,pw}(w) b_m^{ijk} \qquad (A.1)$$

where u, v, w are the parametric coordinates of the mesh nodes, U, V, W are the VBS basis functions and pu, pv, pw are their corresponding degrees.

The i-th B-spline basis function of p-degree, denoted by $U_{i,p}(u)$, is defined by the following recursive formula [53]

$$U_{i,0}(u) = \begin{cases} 1 & \text{if } t_i \leq u < t_{i+1} \\ 0 & \text{otherwise} \end{cases} \qquad (A.2)$$

$$U_{i,p}(u) = \frac{u - t_i}{t_{i+p} - t_i} U_{i,p-1}(u) + \frac{t_{i+p+1} - u}{t_{i+p+1} - t_{i+p}} U_{i+1,p-1}(u)$$

where t_i are knots. The uniform b-splines basis functions are obtained by choosing a uniform knot vector $\mathbf{T}$ as

$$\mathbf{T} = [\underbrace{0, \cdots, 0}_{p+1}, \frac{1}{N}, \cdots, \frac{N-1}{N}, \underbrace{1 \cdots, 1}_{p+1}] \qquad (A.3)$$

where $N = N_u - p$ with N_u being the number of CPs along the parametric coordinate u. The curve is $(p-k)$ times continuously differentiable at a knot of multiplicity $k(\leq p)$ and thus has $C^{(p-k)}$ continuity. Repeating the knots at the end $p+1$ times indicates C^{-1} continuity and will force the endpoints to coincide with the control polygon. Thus the first and the last CPs of a curve with a knot vector described by eq. (A.3) coincide with the endpoints of the curve.

Given the control points' position, the knot vectors and the basis functions degrees, the parametric coordinates (u, v, w) of a point with Cartesian coordinates $\mathbf{r} = (x_r, y_r, z_r)^T$ can be computed by solving the following system of equations

$$\mathbf{R}(u, v, w) = \begin{bmatrix} x(u, v, w) - x_r = 0 \\ y(u, v, w) - y_r = 0 \\ z(u, v, w) - z_r = 0 \end{bmatrix} \tag{A.4}$$

where $x_m(u, v, w)$ are computed through eq. (A.1) after the computation of the basis functions eq. (A.2). The 3×3 system of equations described by eqs. (A.4), is non-linear and can be solved independently for each parameterized mesh point using the Newton-Raphson method. The so-computed parametric coordinates as well as the knot vectors remain fixed during the optimization.

After the parametric coordinates of any parameterized mesh point are known, the computation of its Cartesian coordinates comes at a very low computational cost through eq. (A.1). Consequently, since the mapping from $\mathbb{R}^3(x, y, z) \rightarrow \mathbb{R}^3(u, v, w)$ has been made, every control point displacement can easily be translated into a displacement of the computational mesh. This makes volumetric B-Splines a powerful mesh displacement tool.

Finally, in this thesis, the FI-adjoint formulation is used because of its increased computational accuracy regarding the shape optimization sensitivities, compared to the other formulations [43]. In this formulation, Field Integrals involving all variations in geometric quantities appear in the sensitivity derivatives this requires the computation of the mesh sensitivities w.r.t. the coordinates of the CPs. Differentiating eq. (A.1) w.r.t. b_n, the mesh sensitivities are computed as

$$\frac{\delta x_m}{\delta b_n} = \frac{\delta x_m}{\delta b_n^{abc}}(u, v, w) = \sum_{i=0}^{I} \sum_{j=0}^{J} \sum_{k=0}^{K} U_{i,pu}(u) V_{j,pv}(v) W_{k,pw}(w) \frac{\delta b_m^{ijk}}{\delta b_n^{abc}} =$$
$$= U_{a,pu}(u) V_{b,pv}(v) W_{c,pw}(w) \delta_{nm} \tag{A.5}$$

where δ_{nm} is the Kronecker delta.

Appendix B

Optimization Methods

In this appendix, the theory behind the optimization methods used in this thesis is explained. Those methods are used to update the values of the design variables given that the sensitivities of the objective function and constraints are known. A general constrained nonlinear minimization problem can be written in the following general form:

$$
\begin{aligned}
&\text{minimize} && f(x) \\
&\text{subject to} && g_i(x) \leq 0, && i = 1, \cdots, m \\
& && h_j(x) = 0, && j = 1, \cdots, n
\end{aligned}
\tag{B.1}
$$

where $x = (x_1, \ldots, x_n)^T \in \mathbb{R}^n$ is the vector of design variables, $f(x)$ is the objective function, $g_1, \ldots, g_m$ are functions representing the m inequality constraints and $h_1, \ldots, h_n$ represent the n equality constraints.

In the context of this diploma thesis, ShpO problems are solved using the ISQP method [11] presented in appendix B.1. It is one of the most effective methods for nonlinearly constrained optimization in terms of the number of function calls needed to get to the optimum and can handle many design variables and constraints.

On the other hand, TopO problems are solved using the MMA [52] presented in appendix B.2. MMA is known for its efficiency in solving large-scale optimization problems with many design variables and bound constraints. This makes it a great choice for TopO problems where the number of constraints is larger than or equal to the number of design variables since the porosity values are bounded.

B.1 ISQP

Sequential Quadratic Programming (SQP) [11] as well as its implicit variant (ISQP) [51] used in this thesis, is an iterative method for solving constrained nonlinear optimization problems described by eq. (B.1). SQP methods solve a sequence of optimization subproblems, each of which minimizes a quadratic approximation to the objective function subject to a linearization of the constraints.

Introducing an iteration index k and using Taylor's expansion, the problem described by eq. (B.1), at an iterate $(x_k, \lambda_k, \sigma_k)$, is modeled using the following quadratic program

$$\text{minimize} \quad f(x_k) + \nabla f(x_k)^T p + \tfrac{1}{2} p^T \nabla_{xx}^2 \mathcal{L}(x_k, \sigma_k, \lambda_k) p$$

$$\text{subject to} \quad g_i(x_k) + \nabla g_i(x_k)^T p \leq 0, \qquad\qquad i = 1, \cdots, m \qquad \text{(B.2)}$$

$$h_j(x_k) + \nabla h_j(x_k)^T p = 0, \qquad\qquad j = 1, \cdots, n$$

where $\nabla_{xx}^2 \mathcal{L}(x_k, \sigma_k, \lambda_k)$ is the Hessian of the Lagrangian function. The Lagrangian function is defined as

$$\mathcal{L}(x, \sigma, \lambda) = f(x) + \sum_{i=1}^{m} \sigma_i g_i(x) + \sum_{j=1}^{n} \lambda_j h_j(x) \qquad \text{(B.3)}$$

where $\sigma = (\sigma_1, \cdots, \sigma_m)^T$ is the vector of Karush-Kuhn-Tucker (KKT) multipliers and $\lambda = (\lambda_1, \cdots, \lambda_n)^T$ is the vector of Lagrangian multipliers.

Under certain conditions described in [11], the quadratic problem in eq. (B.2) can be solved leading to the solution p_k and updated Lagrangian multipliers. For each SQP iteration, p_k is used to obtain the new iterate $x_{k+1} = x_k + \eta p_k$, where η is determined by an appropriate line search method.

Many SQP methods approximate the Hessian of the Lagrangian through a quasi-Newton approach, the most commonly used being the Broyden–Fletcher–Goldfarb–Shanno (BFGS) algorithm [11]. The ISQP method overcomes one of the major drawbacks of the traditional SQP method which is computing and storing the entire Hessian of the Lagrangian. In ISQP, only a few vectors that represent the Hessian approximation implicitly according to the limited-memory BFGS algorithm proposed in [54] are stored.

Finally, any bounds constraints in the original problem are handled as inequality constraints. Then, the quadratic subproblem can be solved iteratively by active set strategies or interior point methods where each iteration requires the solution of an equality constrained quadratic programming problem.

B.2 MMA

The MMA, developed by Svanberg [52], represents a family of convex approximation methods suitable for efficiently solving inequality-constrained optimization problems with bounded design variables traditionally used in TopO problems. An inequality-constrained minimization problem can be described in the following general form:

$$\text{minimize} \quad f(x)$$

$$\text{subject to} \quad f_i(x) \leq 0, \qquad\qquad i = 1, \cdots, m \qquad \text{(B.4)}$$

$$x_j^{min} \leq x_j \leq x_j^{max}, \qquad j = 1, \cdots, n$$

Convex approximation methods generate and solve a sequence of explicit approximate convex problems until the solution to the original problem is reached. The general approach used by those methods is represented by the following iterative scheme:

Step 0. Choose a starting point $x^{(0)}$, and let the iteration index $k = 0$.

Step 1. Given an iteration point $x^{(k)}$, calculate $f_i(x^{(k)})$ and the gradients $\nabla f_i(x^{(k)})$ for $i = 0, 1, \cdots, m$.

Step 2. Generate a subproblem $P^{(k)}$ by replacing, in P, the (usually implicit) functions f_i by approximating explicit functions $f_i^{(k)}$, based on the calculations from step 1.

Step 3. Solve $P^{(k)}$ and let the optimal solution of this subproblem be the next iteration point $x^{(k+1)}$. Let $k = k + 1$ and go to step 1.

The process is interrupted when some convergence criteria are fulfilled, or when the user is satisfied with the current solution $x^{(k)}$.

Given the iteration point $x^{(k)}$, values of the parameters $L_j^{(k)}$ and $U_j^{(k)}$ are chosen, for $j = 1, \cdots, n$ such that

$$L_j^{(k)} \leq x_j^{(k)} \leq U_j^{(k)} \tag{B.5}$$

Then, for each $i = 0, 1, \cdots, m$, the approximating functions $f_i^{(k)}$ in the subproblem of the MMA algorithm, are defined by

$$f_i^{(k)} = r_i^{(k)} + \sum_{j=1}^{n} \left(\frac{p_{ij}^{(k)}}{U_j^{(k)} - x_j} + \frac{q_{ij}^{(k)}}{x_j - L_j^{(k)}} \right) \tag{B.6}$$

where

$$p_{ij}^{(k)} = \begin{cases} (U_j^{(k)} - x_j^{(k)})^2 \partial f_i / \partial x_j, & \text{if } \partial f_i / \partial x_j > 0 \\ 0, & \text{if } \partial f_i / \partial x_j \leq 0 \end{cases} \tag{B.7}$$

$$q_{ij}^{(k)} = \begin{cases} 0, & \text{if } \partial f_i / \partial x_j \geq 0 \\ -(x_j^{(k)} - L_j^{(k)})^2 \partial f_i / \partial x_j, & \text{if } \partial f_i / \partial x_j < 0 \end{cases} \tag{B.8}$$

$$r_i^{(k)} = f_i(x^{(k)}) - \sum_{j=1}^{n} \left(\frac{p_{ij}^{(k)}}{U_j^{(k)} - x_j} + \frac{q_{ij}^{(k)}}{x_j - L_j^{(k)}} \right) \tag{B.9}$$

where all derivatives $\partial f_i / \partial x_j$ are evaluated at $x = x^{(k)}$.

Then, as is easily checked, $f_i^{(k)}$ is a first order approximation of f_i at $x^{(k)}$, because

$$f_i^{(k)} = f_i(x^{(k)}) \quad \text{and} \quad \partial f_i^{(k)} / \partial x_j = \partial f_i / \partial x_j \text{ at } x = x^{(k)}$$

for $i = 0, 1, \cdots, m$ and $j = 1, \cdots, n$.

Furthermore, the second derivatives of $f_i^{(k)}$ at any point x such that $L_j^{(k)} < x_j < U_j^{(k)}$ for all j, are given by

$$\frac{\partial^2 f_i^{(k)}}{\partial x_j^2} = \frac{2p_{ij}^{(k)}}{(U_j^{(k)} - x_j)^3} + \frac{2q_{ij}^{(k)}}{(x_j^{(k)} - L_j)^3} \tag{B.10}$$

and

$$\frac{\partial^2 f_i^{(k)}}{\partial x_j \partial x_l} = 0 \; \textit{if } j \neq l$$

Thus, since $p_{ij}^{(k)} \geq 0$ and $q_{ij}^{(k)} \geq 0$, $f_i^{(k)}$ is a convex function. The moving asymptotes $L_j^{(k)}$ and $U_j^{(k)}$ for the design variable x_j can adjust the curvature of the approximating functions $f_i^{(k)}$. If asymptotes are selected to provide tight or loose bounds on the variables, the method becomes conservative and slow or aggressive and possibly oscillatory, respectively.

A general rule for how to change the values of $L_j^{(k)}$ and $U_j^{(k)}$, [55], is presented as follows.

In the first two iterations, when $k = 1$ and $k = 2$,

$$L_j^{(k)} = x_j^{(k)} - 0.5(x_j^{max} - x_j^{min}) \tag{B.11}$$

$$U_j^{(k)} = x_j^{(k)} + 0.5(x_j^{max} - x_j^{min}) \tag{B.12}$$

while in later iterations, when $k \geq 3$,

$$L_j^{(k)} = x_j^{(k)} - \gamma_j^{(k)}(x_j^{(k-1)} - L_j^{(k-1)}) \tag{B.13}$$

$$U_j^{(k)} = x_j^{(k)} + \gamma_j^{(k)}(U_j^{(k-1)} - x_j^{(k-1)}) \tag{B.14}$$

where

$$\gamma_j^{(k)} = \begin{cases} 0.7, & \text{if } (x_j^{(k)} - x_j^{(k-1)})(x_j^{(k-1)} - x_j^{(k-2)}) < 0, \\ 1, & \text{if } (x_j^{(k)} - x_j^{(k-1)})(x_j^{(k-1)} - x_j^{(k-2)}) = 0, \\ 1.2, & \text{if } (x_j^{(k)} - x_j^{(k-1)})(x_j^{(k-1)} - x_j^{(k-2)}) > 0 \end{cases} \tag{B.15}$$

Observing the $\gamma_j^{(k)}$ variable, if the signs of $(x_j^{(k)} - x_j^{(k-1)})$ and $(x_j^{(k-1)} - x_j^{(k-2)})$ are opposite indicating an oscillation in the variable x_j, the asymptotes are selected to provide tight bounds and when the signs are equal indicating that the asymptotes are slowing down the convergence, asymptotes are selected to provide loose bounds.

Now, with the approximating functions defined by eq. (B.6), the formulation of the subproblem solved in each iteration of the MMA called $P^{(k)}$ is presented. Omitting the iteration index (k) notation for simplicity, the subproblem is written as:

$$
\begin{aligned}
&\text{minimize} && f_0(x) + \sum_{i=1}^{m}(c_i y_i + \tfrac{1}{2}y_i^2) && \\
&\text{subject to} && f_i(x) - y_i \leq 0, && i = 1, \cdots, m, \\
& && x_j^{min} \leq x_j \leq x_j^{max}, && j = 1, \cdots, n, \\
& && y_i \geq 0, && i = 1, \cdots, m.
\end{aligned}
\tag{B.16}
$$

where each c_i should be a "relatively large" fixed real number and $y = (y_1, \cdots, y_m)^T \in \mathbb{R}^m$ are "artificial" variables. $P^{(k)}$ is a separable problem since both the objective and the constraints are a sum of functions of the individual variables x_j, y_i.

The introduction of the y_i variables guarantees that a feasible solution of the subproblem eq. (B.16) exists as, for any x it is possible to choose y such that the constraints become satisfied. Moreover, there is at least one optimal solution of eq. (B.16) and each of them always satisfies the KKT conditions.

If the coefficients c_i are chosen as sufficiently large numbers, then typically $\hat{y} = 0$ in any optimal solution $(\hat{x}, \hat{y})$ of eq. (B.16), and then the corresponding $\hat{x}$ is an optimal solution of eq. (B.4).

The MMA subproblem, obtains properties such as convexity and separability making it an ideal candidate for many numerical solution schemes. Of these solution strategies, a dual method is suggested and described in [52].

Bibliography

[1] J.-C. Han, S. Dutta, and S. Ekkad, *Gas Turbine Heat Transfer and Cooling Technology*. Taylor & Francis Group, 2012, p. 887.

[2] R. J. Goldstein, "Film cooling," pp. 321–379, 1971.

[3] W. D. Morris, *Heat transfer and fluid flow in rotating coolant channels*. Research Studies Press, 1981, p. 228.

[4] J.-C. Han, "Advanced cooling in gas turbines 2016 max jakob memorial award paper," *Journal of Heat Transfer*, vol. 140, no. 11, Jul. 2018.

[5] L. Davis, *Handbook of genetic algorithms*. Van Nostrand Reinhold, 1991, p. 385.

[6] G. Winter, *Genetic Algorithms in Engineering and Computer Science (Wiley Series in Computational Methods in Applied Sciences)*. John Wiley Sons, p. 480.

[7] T. Back, *Evolutionary Algorithms in Theory and Practice, Evolution Strategies, Evolutionary Programming, Genetic Algorithms*. Oxford University Press, USA, 1995, p. 328.

[8] P. E. Gill, *Practical optimization*. Academic Press, 1981, p. 401.

[9] D. P. Bertsekas, *Constrained optimization and Lagrange multiplier methods*. Athena Scientific, 1996, p. 395.

[10] D. P. Bertsekas, *Nonlinear Programming*. Athena Scientific, 1999, p. 802.

[11] J. Nocedal and S. Wright, *Numerical Optimization (Springer Series in Operations Research and Financial Engineering)*. Springer, 2006, p. 664.

[12] J. C. Newman, W. K. Anderson, and D. L. Whitfield, "Multidisciplinary sensitivity derivatives using complex variables," *Mississippi State University Publication, MSSU-EIRS-ERC-98-08*, 1998.

[13] É. Turgeon, D. Pelletier, J. Borggaard, and S. Etienne, "Application of a sensitivity equation method to the k–ϵ model of turbulence," *Optimization and Engineering*, vol. 8, no. 4, pp. 341–372, May 2007.

[14] H. Hu, "Application of an automatic differentiation method to a 2D Navier-Stokes CFD code," *Computer Methods in Applied Mechanics and Engineering*, vol. 156, no. 1-4, pp. 179–183, Apr. 1998.

[15] A. Jameson, "Aerodynamic design via control theory," *Journal of Scientific Computing*, vol. 3, no. 3, pp. 233–260, Sep. 1988.

[16] W. K. Anderson and D. L. Bonhaus, "Airfoil design on unstructured grids for turbulent flows," *AIAA Journal*, vol. 37, no. 2, pp. 185–191, Feb. 1999.

[17] S. Kim, J. Alonso, and A. Jameson, "A gradient accuracy study for the adjoint-based Navier-Stokes design method," in *37th Aerospace Sciences Meeting and Exhibit*, American Institute of Aeronautics and Astronautics, Jan. 1999.

[18] W. K. Anderson and V. Venkatakrishnan, "Aerodynamic design optimization on unstructured grids with a continuous adjoint formulation," *Computers & Fluids*, vol. 28, no. 4-5, pp. 443–480, 1999.

[19] A. Jameson and J. Reuther, "Control theory based airfoil design using the Euler equations," in *5th Symposium on Multidisciplinary Analysis and Optimization*, American Institute of Aeronautics and Astronautics, Aug. 1994.

[20] J. Elliott and J. Peraire, "Aerodynamic design using unstructured meshes," Jun. 1996.

[21] M. B. Giles, M. C. Duta, J.-D. Muller, and N. A. Pierce, "Algorithm developments for discrete adjoint methods," *AIAA Journal*, vol. 41, no. 2, pp. 198–205, Feb. 2003.

[22] L. Mangani, M. Cerutti, M. Maritano, and M. Spel, "Conjugate heat transfer analysis of NASA C3X film cooled vane with an object-oriented CFD code," in *Volume 4: Heat Transfer, Parts A and B*, ASMEDC, Oct. 2010.

[23] S. Caloni and S. Shahpar, "Multi-disciplinary Analyses for the Design of a High Pressure Turbine Blade Tip," in *Volume 5A: Heat Transfer*, American Society of Mechanical Engineers, Jun. 2016.

[24] K.-S. Ho, J. S. Liu, T. Elliott, and B. Aguilar, "Conjugate heat transfer analysis for gas turbine film-cooled blade," Jun. 2016.

[25] A. G. Fedorov and R. Viskanta, "Three-dimensional conjugate heat transfer in the microchannel heat sink for electronic packaging," *International Journal of Heat and Mass Transfer*, vol. 43, no. 3, pp. 399–415, Feb. 2000.

[26] K. K. Ambatipudi and M. M. Rahman, "Analysis of conjugate heat transfer in microchannel heat sinks," *Numerical Heat Transfer: Part A: Applications*, vol. 37, no. 7, pp. 711–731, 2000.

[27] B. H. Dennis, I. N. Egorov, G. S. Dulikravich, and S. Yoshimura, "Optimization of a large number of coolant passages located close to the surface of a turbine blade," Jan. 2003.

[28] K. Gkaragkounis, E. Papoutsis-Kiachagias, and K. Giannakoglou, "The continuous adjoint method for shape optimization in conjugate heat transfer problems with turbulent incompressible flows," *Applied Thermal Engineering*, vol. 140, pp. 351–362, Jul. 2018.

[29] B. Wang, W. Zhang, G. Xie, Y. Xu, and M. Xiao, "Multiconfiguration shape optimization of internal cooling systems of a turbine guide vane based on thermomechanical and conjugate heat transfer analysis," *Journal of Heat Transfer*, vol. 137, no. 6, Jun. 2015.

[30] A. Mousavi and S. Nadarajah, "Adjoint-based multidisciplinary design optimization of cooled gas turbine blades," in *49th AIAA Aerospace Sciences Meeting including the New Horizons Forum and Aerospace Exposition*, American Institute of Aeronautics and Astronautics, Jan. 2011.

[31] M. Zeinalpour, K. Mazaheri, and K. Kiani, "A coupled adjoint formulation for non-cooled and internally cooled turbine blade optimization," *Applied Thermal Engineering*, vol. 105, pp. 327–335, Jul. 2016.

[32] M. P. Bendsøe and O. Sigmund, "Material interpolation schemes in topology optimization," *Archive of Applied Mechanics (Ingenieur Archiv)*, vol. 69, no. 9-10, pp. 635–654, Nov. 1999.

[33] T. Borrvall and J. Petersson, "Topology optimization of fluids in Stokes flow," *International Journal for Numerical Methods in Fluids*, vol. 41, no. 1, pp. 77–107, 2002.

[34] A. Gersborg-Hansen, O. Sigmund, and R. Haber, "Topology optimization of channel flow problems," *Structural and Multidisciplinary Optimization*, vol. 30, no. 3, pp. 181–192, Jun. 2005.

[35] L. H. Olesen, F. Okkels, and H. Bruus, "A high-level programming-language implementation of topology optimization applied to steady-state Navier-Stokes flow," *International Journal for Numerical Methods in Engineering*, vol. 65, no. 7, pp. 975–1001, 2006.

[36] C. Othmer, "A continuous adjoint formulation for the computation of topological and surface sensitivities of ducted flows," *International Journal for Numerical Methods in Fluids*, vol. 58, no. 8, pp. 861–877, Nov. 2008.

[37] E. A. Kontoleontos, E. M. Papoutsis-Kiachagias, A. S. Zymaris, D. I. Papadimitriou, and K. C. Giannakoglou, "Adjoint-based constrained topology optimization for viscous flows, including heat transfer," *Engineering Optimization*, vol. 45, no. 8, pp. 941–961, Aug. 2013.

[38] E. Papoutsis-Kiachagias, "Adjoint methods for turbulent flows, applied to shape or topology optimization and robust design," Ph.D. dissertation, NTUA, 2013.

[39] A. Zymaris, D. Papadimitriou, K. Giannakoglou, and C. Othmer, "Continuous adjoint approach to the Spalart–Allmaras turbulence model for incompressible flows," *Computers & Fluids*, vol. 38, no. 8, pp. 1528–1538, 2009.

[40] F. M. White, *Viscous fluid flow*. McGraw-Hill New York, 2006, vol. 3.

[41] S. V. Patankar and D. B. Spalding, "A calculation procedure for heat, mass and momentum transfer in three-dimensional parabolic flows," in *Numerical prediction of flow, heat transfer, turbulence and combustion*, Elsevier, 1983, pp. 54–73.

[42] K. Gkaragkounis, "The continuous adjoint method in aerodynamic and conjugate heat transfer shape optimization, for turbulent flows," Ph.D. dissertation, NTUA, 2020.

[43] I. Kavvadias, E. Papoutsis-Kiachagias, and K. Giannakoglou, "On the proper treatment of grid sensitivities in continuous adjoint methods for shape optimization," *Journal of Computational Physics*, vol. 301, pp. 1–18, Nov. 2015.

[44] G. K. Karpouzas, "A hybrid method for shape and topology optimization in fluid mechanics," Ph.D. dissertation, NTUA, 2020.

[45] K. Yaji, T. Yamada, S. Kubo, K. Izui, and S. Nishiwaki, "A topology optimization method for a coupled thermal–fluid problem using level set boundary expressions," *International Journal of Heat and Mass Transfer*, vol. 81, pp. 878–888, Feb. 2015.

[46] B. S. Lazarov and O. Sigmund, "Filters in topology optimization based on Helmholtz-type differential equations," *International Journal for Numerical Methods in Engineering*, vol. 86, no. 6, pp. 765–781, Dec. 2010.

[47] E. M. Papoutsis-Kiachagias and K. C. Giannakoglou, "Continuous adjoint methods for turbulent flows, applied to shape and topology optimization: Industrial applications," *Archives of Computational Methods in Engineering*, vol. 23, no. 2, pp. 255–299, Dec. 2014.

[48] M. e. Abbassi, D. Lahaye, and K. Vuik, "Modelling turbulent combustion coupled with conjugate heat transfer in openfoam," in *Numerical Mathematics and Advanced Applications ENUMATH 2019*, Springer, 2021, pp. 1137–1145.

[49] L. Hylton, M. Mihelc, E. Turner, D. Nealy, and R. York, "Analytical and experimental evaluation of the heat transfer distribution over the surfaces of turbine vanes," Tech. Rep., 1983.

[50] E. Papoutsis-Kiachagias, N. Magoulas, J. Mueller, C. Othmer, and K. Giannakoglou, "Noise reduction in car aerodynamics using a surrogate objective function and the continuous adjoint method with wall functions," *Computers & Fluids*, vol. 122, pp. 223–232, Nov. 2015.

[51] M.-W. HUANG and J. Arora, "A self-scaling implicit SQP method for large scale structural optimization," *International journal for numerical methods in engineering*, vol. 39, no. 11, pp. 1933–1953, 1996.

[52] K. Svanberg, "The method of moving asymptotes—a new method for structural optimization," *International Journal for Numerical Methods in Engineering*, vol. 24, no. 2, pp. 359–373, Feb. 1987.

[53] L. Piegl, *The NURBS Book*. Springer Berlin Heidelberg, 1995, p. 646.

[54] J. Nocedal, "Updating quasi-newton matrices with limited storage," *Mathematics of Computation*, vol. 35, no. 151, pp. 773–782, 1980.

[55] K. Svanberg, "A class of globally convergent optimization methods based on conservative convex separable approximations," *SIAM Journal on Optimization*, vol. 12, no. 2, pp. 555–573, Jan. 2002.

Εθνικό Μετσόβιο Πολυτεχνείο
Σχολή Μηχανολόγων Μηχανικών
Εργαστήριο Θερμικών Στροβιλομηχανών
Μονάδα Παράλληλης ΥΡΔ & Βελτιστοποίησης

Βελτιστοποίηση Αγωγών Ψύξης με τη Συνεχή Συζυγή Μέθοδο για Προβλήματα Συζευγμένης Μεταφοράς Θερμότητας

Διπλωματική εργασία
Εκτενής Περίληψη στα Ελληνικά

Κουκουγκέλης Γεώργιος

Επιβλέπων: Κυριάκος Χ. Γιαννάκογλου, Καθηγητής ΕΜΠ

Αθήνα, 29 Ιουνίου 2023

1 Εισαγωγή

Η ολοένα και αυξανόμενη υπολογιστική ισχύς και η αξιοπιστία των υπολογιστικών μεθόδων, έθεσαν τη βάση για την εκτεταμένη χρήση της Υπολογιστικής Ρευστοδυναμικής (ΥΡΔ) σε πληθώρα πρακτικών προβλημάτων όπως είναι η προσομοίωση ροών σε περίπλοκα συστήματα αγωγών, καθώς και γύρω από γεωμετρίες αεροπλάνων και αυτοκινήτων. Η εισαγωγή της βελτιστοποίησης σε αυτόν τον τομέα, έχει οδηγήσει στην ανάπτυξη μεθόδων για τον αυτοματοποιημένο σχεδιασμό αερο/υδροδυναμικών μορφών.

Σε ένα πρόβλημα βελτιστοποίησης, σκοπός είναι η ελαχιστοποίηση/μεγιστοποίηση κάποιας ποσότητας γνωστής ως *συνάρτηση-στόχος* μέσω εύρεσης της κατάλληλης τιμής ενός σετ παραμέτρων που ονομάζονται *μεταβλητές σχεδιασμού*. Η τιμή της συνάρτησης-στόχου εξαρτάται τόσο από τις τιμές των μεταβλητών σχεδιασμού όσο και από τις τιμές των μεταβλητών της ροής, οι οποίες υπολογίζονται από την επίλυση των εξισώσεων ροής στην υπόψη γεωμετρία.

Οι μέθοδοι βελτιστοποίησης με χρήση ΥΡΔ διακρίνονται σε στοχαστικές [1] και αιτιοκρατικές [2]. Οι αιτιοκρατικές μέθοδοι, εκκινούν από μία δεδομένη λύση την οποία βελτιώνουν βασιζόμενες στις παραγώγους της συνάρτησης-στόχου ως προς τις μεταβλητές σχεδιασμού που αναφέρονται ως παράγωγοι ευαισθησίας.

Η απόδοση των αιτιοκρατικών μεθόδων είναι άρρηκτα συνδεδεμένη με το κόστος υπολογισμού των παραγώγων ευαισθησίας. Μεταξύ των διαφόρων μεθόδων υπολογισμού παραγώγων ευαισθησίας, η συζυγής μέθοδος [3, 4] διακρίνεται για την ανεξαρτησία του κόστους υπολογισμού των παραγώγων από το πλήθος των μεταβλητών σχεδιασμού. Οι συζυγείς μέθοδοι κατηγοριοποιούνται, ανάλογα με τη σειρά διαφόρισης και διακριτοποίησης, στη συνεχή [3] και τη διακριτή [4]. Η παρούσα εργασία ασχολείται αποκλειστικά με τη συνεχή συζυγή μέθοδο.

1.1 Βελτιστοποίηση Μορφής

Στην βελτιστοποίηση μορφής, σκοπός είναι η εύρεση του σχήματος της γεωμετρίας που ελαχιστοποιεί/μεγιστοποιεί ένα συγκεκριμένο κριτήριο απόδοσης ενώ παράλληλα ικανοποιεί τους περιορισμούς που έχουν τεθεί. Η υπό εξέταση γεωμετρία, ελέγχεται από έναν αριθμό παραμέτρων, όπως για παράδειγμα, τις συντεταγμένες των σημείων ελέγχου ενός πολυωνύμου Bézier-Bernstein οι οποίες αποτελούν μεταβλητές σχεδιασμού του προβλήματος βελτιστοποίησης. Η αντιστοίχηση από τις μεταβλητές σχεδιασμού στη γεωμετρία, ονομάζεται παραμετροποίηση γεωμετρίας. Στην παρούσα εργασία, η μέθοδος παραμετροποίησης που χρησιμοποιείται είναι οι ογκομετρικές B-Splines [5] οι οποίες πέραν της γεωμετρίας μετακινούν και το υπολογιστικό πλέγμα εξαλείφοντας έτσι την ανάγκη επαναπλεγματοποίησης.

1.2 Βελτιστοποίηση Τοπολογίας

Σκοπός της βελτιστοποίησης τοπολογίας είναι ο προσδιορισμός της βέλτιστης κατανομής υλικού στον χώρο και όχι απλώς η τροποποίηση του σχήματος μιας κατασκευής για τη βελτιστοποίησή της. Στα ρευστά, εφαρμόζεται με την εισαγωγή όρων πηγής στις εξισώσεις ροής που εξαρτώνται από ένα πεδίο πορώδους. Η ροή συναντά μεγάλη αντίσταση στις περιοχές με υψηλές τιμές πορώδους που σημαίνει

ότι η ταχύτητά της μηδενίζεται. Έτσι, αυτές οι περιοχές αντιστοιχούν στο στερε-
οποιημένο μέρος του χώρου ενώ περιοχές με μηδενική τιμή πορώδους ανήκουν
στη ροή αφού εκεί δεν εμφανίζεται αντίσταση επαγόμενη από το πορώδες. Για
μια δεδομένη συνάρτηση-στόχο, η βελτιστοποίηση τοπολογίας επιχειρεί να καθο-
ρίσει τις ιδανικές τιμές πορώδους σε κάθε κελί του πλέγματος με σκοπό να την
ελαχιστοποιήσει/μεγιστοποιήσει. Αυτό σημαίνει ότι ο αριθμός των μεταβλητών
σχεδιασμού ισούται με τον αριθμό των κελιών και, συνεπώς, η συζυγής μέθοδος
είναι η πιο κατάλληλη για τον υπολογισμό των παραγώγων ευαισθησίας.

2 Η Συνεχής Συζυγής Μέθοδος για προβλήματα βελ-τιστοποίησης μορφής

Στα προβλήματα με συζευγμένη μεταφορά θερμότητας, το υπολογιστικό χωρίο
αποτελείται από τα ρευστά τμήματα Ω^F και τα στερεά τμήματα Ω^S διαχωριζόμενα
από μία διεπιφάνεια $\overline{S}$. Για τα τμήματα του ρευστού, οι εξισώσεις που επιλύονται
είναι οι RANS για χρονικά μόνιμες και ασυμπίεστες ροές μαζί με την ενεργειακή
εξίσωση, ενώ για τα στερεά επιλύεται η εξίσωση χρονικά μόνιμης μεταφοράς θερ-
μότητας.

Πρώτο βήμα για τη διαμόρφωση των συζυγών εξισώσεων με την συνεχή συζυγή
μέθοδο [6] είναι η θεώρηση της επαυξημένης συνάρτησης-στόχου, J_{aug}, η οποία
ορίζεται προσθέτοντας τα ογκικά ολοκληρώματα των υπολοίπων των εξισώσεων κα-
τάστασης πολλαπλασιασμένα με τις συζυγείς μεταβλητές στην συνάρτηση στόχο
J. Διαφορίζοντας την επαυξημένη ως προς τις μεταβλητές σχεδιασμού, προκύ-
πτουν όροι που πολλαπλασιάζουν τις παραγώγους των μεταβλητών ροής ως προς
τις μεταβλητές σχεδιασμού ο υπολογισμός των οποίων έχει σημαντικό υπολογι-
στικό κόστος. Έτσι, μετά από εκτενή μαθηματική επεξεργασία, [7], οι συζυγείς
εξισώσεις όπως και οι οριακές συνθήκες προκύπτουν με τον μηδενισμό των προ-
αναφερθέντων όρων. Οι εξισώσεις και οι οριακές συνθήκες για το πρωτεύον και
το συζυγές πρόβλημα στη βελτιστοποίηση μορφής παρουσιάζονται αναλυτικά στο
Κεφάλαιο 2. Για την επίλυση των εξισώσεων αυτών γίνεται χρήση του αλγορίθμου
SIMPLE [8].

3 Η Συνεχής Συζυγής Μέθοδος για προβλήματα βελ-τιστοποίησης τοπολογίας

Το πρωτεύον πρόβλημα στη βελτιστοποίηση τοπολογίας περιγράφεται από τις
εξισώσεις Navier-Stokes (NS) μαζί με την ενεργειακή εξίσωση. Για την προσομοί-
ωση της στερεοποίησης τμημάτων του υπολογιστικού χωρίου, οι εξισώσεις ροής
επαυξάνονται με όρους πηγής που εξαρτώνται από το πεδίο του πορώδους α. Το
πεδίο του πορώδους παίρνει τιμές από 0 έως 1. Τα κελιά του πλέγματος με τιμή
πορώδους περίπου 0 ανήκουν στη ροή, ενώ τα αυτά με τιμή 1 ανήκουν στο στερεό.
Οι θερμοφυσικές ιδιότητες των κελιών που ανήκουν στην "γκρι" ζώνη, δηλαδή
έχουν τιμή πορώδους ανάμεσα στο 0 και το 1, προκύπτουν από παρεμβολή των
ιδιοτήτων του ρευστού και του στερεού.

Για την αποφυγή αποτελεσμάτων τύπου "σκακιέρας", δηλαδή με διαδοχική
εναλλαγή κελιών που παριστούν στερεό και ρευστό, εφαρμόζεται κανονικοποί-

ηση (regularization) του πεδίου του πορώδους με ένα φίλτρο Helmholtz. Έτσι παράγεται ένα νέο πεδίο που ονομάζεται $\tilde{\alpha}$. Καθώς η κανονικοποίηση του πεδίου του πορώδους θολώνει τη γραμμή μεταξύ ρευστών και στερεών τμημάτων, γίνεται ένα βήμα προβολής (projection) το οποίο αυξάνει την αντίθεση του πεδίου $\tilde{\alpha}$ παράγοντας το πεδίο β. Τα βήματα επεξεργασίας του πορώδους φαίνονται στο σχ. 1.
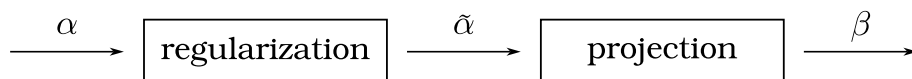

Σχήμα 1: Βήματα επεξεργασίας του πεδίου του πορώδους.

Εφαρμόζοντας την συνεχή συζυγή μέθοδο προκύπτουν οι συζυγείς εξισώσεις και οριακές συνθήκες. Για την αποφυγή υπολογισμού των όρων $\partial\tilde{\alpha}/\partial\alpha$, ένας επιπλέον όρος προστίθεται στην επαυξημένη με το ογκικό ολοκλήρωμα του υπολοίπου της εξίσωσης κανονικοποίησης. Έτσι, παράγεται μία ακόμα συζυγής εξίσωση που αποτελεί την συζυγή του φίλτρου Helmholtz. Οι εξισώσεις που επιλύονται για τη βελτιστοποίηση τοπολογίας παρουσιάζονται αναλυτικά στο Κεφάλαιο 3.

4 Ανάλυση Συζευγμένης Μεταφοράς Θερμότητας σε σωματόδετα πλέγματα

Η πρώτη εφαρμογή αφορά την επίλυση του πρωτεύοντος προβλήματος της ροής με συζευγμένη μεταφορά θερμότητας στη 2Δ γεωμετρία που φαίνεται στο σχ. 2. Η γεωμετρία αυτή σχεδιάστηκε με έναυσμα την πορεία που ακολουθεί η ροή σε ένα εσωτερικά ψυχόμενο πτερύγιο στροβιλομηχανής.
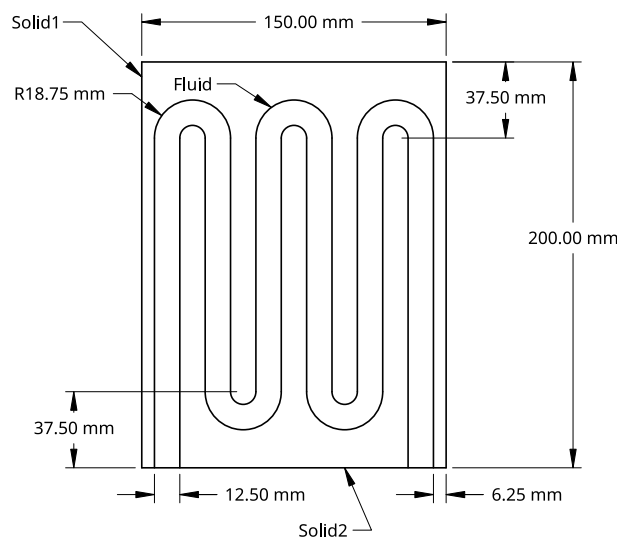

Σχήμα 2: Γεωμετρία και διαστάσεις καμπύλου αγωγού που χρησιμοποιείται στην ανάλυση. Διακρίνονται τρεις διαφορετικές περιοχές, μια περιοχή καλούμενη Fluid που ανήκει στη ροή και δύο περιοχές στερεού Solid1 και Solid2.

Η ροή εισέρχεται από την αριστερή πλευρά της περιοχής Fluid με ταχύτητα μέτρου $|v| = 0.5\,\mathrm{m/s}$ και θερμοκρασία $T^F = 373\,\mathrm{K}$. Το στερεό Solid1 έχει θερμο-

κρασία $T = 873\,\text{K}$ στο πάνω και τα πλευρικά τοιχώματα, ενώ τα τοιχώματα στην βάση των δύο στερεών περιοχών είναι αδιαβατικά.

Το υπολογιστικό πλέγμα που χρησιμοποιείται για την ανάλυση φαίνεται στο σχ. 3. Για την εύκολη διάκρισή του από τα πλέγματα που χρησιμοποιούνται στη συνέχεια, αυτό ονομάζεται BFM1 (Body-Fitted Mesh).
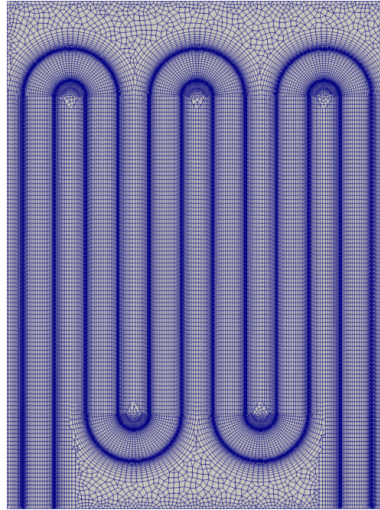
Σχήμα 3: Σωματόδετο πλέγμα καμπύλου αγωγού (BFM1).

Το πλέγμα στην περιοχή Fluid είναι δομημένο και αποτελείται από $\sim 32K$ κελιά ενώ το πλέγμα των στερεών περιοχών αποτελείται από $\sim 18K$ κελιά στην καθεμιά. Η ροή είναι στρωτή με αριθμό $Re = 417$. Το ρευστό θεωρείται αέρας με σταθερή πυκνότητα $\rho^F = 1.2\,\text{kg/m}^3$, κινηματική συνεκτικότητα $\nu^F = 1.5 \times 10^{-5}\,\text{m}^2/\text{s}$, ειδική θερμοχωρητικότητα υπό σταθερή πίεση $c_p^F = 1006\,\text{J/(kgK)}$ και θερμική αγωγιμότητα $k^F = 0.026\,\text{W/(mK)}$. Η θερμική αγωγιμότητα των στερεών λαμβάνεται ως $k^S = 12.7\,\text{W/(mK)}$ που αντιστοιχεί σε ανοξείδωτο χάλυβα ASTM 310.

Για την ανάλυση χρησιμοποιούνται δύο κώδικες. Ο πρώτος αποτελεί τμήμα της βασικής έκδοσης του OpenFOAM© για την επίλυση μόνιμων συμπιεστών ροών με συζευγμένη μεταφορά θερμότητας ενώ ο δεύτερος έχει δημιουργηθεί από τη ΜΠΥΡ&Β/ΕΜΠ βασισμένος στον κώδικα του OpenFOAM© και επιλύει ασυμπίεστες ροές. Για την διάκρισή τους, ο πρώτος καλείται **PBF1** (Primal Body-Fitted) ενώ ο δεύτερος **PBF2**. Σκοπός αυτής της σύγκρισης, είναι η επικύρωση των αποτελεσμάτων του **PBF2** καθώς αργότερα χρησιμοποιείται για τη βελτιστοποίηση.

Μετά τον υπολογισμό των πεδίων ταχύτητας, πίεσης και θερμοκρασίας από τους δύο κώδικες, υπολογίζονται η μέση θερμοκρασία του ρευστού στην έξοδο και οι απώλειες ολικής πίεσης. Τα αποτελέσματα παρουσιάζονται στον πίνακα 1.

	PBF1	**PBF2**
$T_{out}[\text{K}]$	629.6	630.1
$\Delta p_t[\text{Pa}]$	1.396	1.395

Πίνακας 1: Τιμές μέσης θερμοκρασίας εξόδου και απωλειών ολικής πίεσης που υπολογίστηκαν από τους δύο κώδικες.

Παρατηρείται ικανοποιητική ταύτιση μεταξύ των αποτελεσμάτων και συνεπώς, η αξιολόγηση των γεωμετριών που θα προκύψουν από τη βελτιστοποίηση μπορεί να πραγματοποιηθεί με τον κώδικα **PBF2**.

4.1 Βελτιστοποίηση μορφής

Η συνάρτηση-στόχος προς ελαχιστοποίηση, αποτελείται από δύο επιμέρους στόχους. Ο πρώτος αφορά την μεγιστοποίηση της μέσης θερμοκρασίας εξόδου του ρευστού ενώ ο δεύτερος, την ελαχιστοποίηση των απωλειών ολικής πίεσης. Η συνάρτηση-στόχος εκφράζεται ως

$$J^{total} = -w\hat{J}^{meanT} + (1-w)\hat{J}^{p_t} \tag{1}$$

όπου $w \in [0,1]$ είναι συντελεστής βαρύτητας. Το σύμβολο (∧) υποδηλώνει την κανονικοποίηση των δύο στόχων, η οποία γίνεται με διαίρεσή της τιμής τους με αυτή που λαμβάνουν στον μηδενικό κύκλο βελτιστοποίησης.

Οι ογκομετρικές B-Splines παραμετροποιούν τη διεπαφή μεταξύ των ρευστών και στερεών περιοχών που φαίνονται στο σχ. 2. Τα σημεία ελέγχου των ογκομετρικών B-Splines φαίνονται στο σχ. 4.
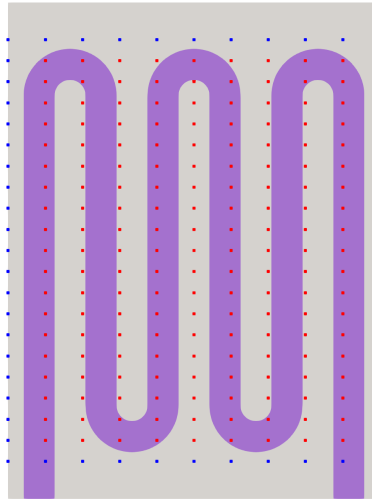
Σχήμα 4: Κουτί ογκομετρικών B-Splines 11×21 που παραμετροποιεί τη γεωμετρία. Τα σημεία ελέγχου με μπλε χρώμα παραμένουν σταθερά, ενώ τα κόκκινα μπορούν να κινηθούν.

Γίνονται τρεξίματα για 4 διαφορετικά βάρη ($w = \{0.9, 0.8, 0.5, 0.2\}$). Οι διάφορες γεωμετρίες που προκύπτουν με τη βελτιστοποίηση μορφής φαίνονται στο σχ. 5.
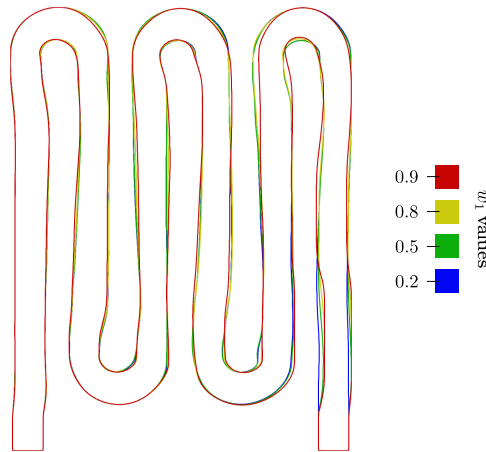
Σχήμα 5: Βέλτιστες γεωμετρίες που προκύπτουν για τα 4 βάρη που χρησιμοποιήθηκαν στη συνάρτηση-στόχο.

Με τη μείωση της τιμής του βάρους w, παρατηρούνται λιγότεροι κυματισμοί στην γεωμετρία του αγωγού. Οι κυματισμοί ενισχύουν την μεταφορά θερμότητας από το στερεό στο ρευστό καθώς δημιουργούνται ανακυκλοφορίες στην ροή και αυξάνεται η επιφάνεια εναλλαγής θερμότητας. Παράλληλα ωστόσο, αυτή η αλλαγή στη γεωμετρία έχει ως αποτέλεσμα την αύξηση των απωλειών ολικής πίεσης. Στον πίνακα 2 παρουσιάζονται η μέση θερμοκρασία της ροής στην έξοδο και οι απώλειες ολικής πίεσης για τις βελτιστοποιημένες γεωμετρίες καθώς και η ποσοστιαία μεταβολή τους από την αρχική.

w	T_{out}[K]	Temperature increase	Δp_t[Pa]	Losses decrease
0.95	645.4	2.43 %	1.517	−8.69 %
0.9	635.3	0.82 %	1.250	10.42 %
0.8	630.5	0.07 %	1.178	15.46 %
0.5	627.2	−0.45 %	1.165	16.49 %
0.2	622.9	−1.13 %	1.149	17.67 %

Πίνακας 2: Μέση θερμοκρασία στην έξοδο και απώλειες ολικής πίεσης για τις βελτιστοποιημένες γεωμετρίες.

5 Ανάλυση με τον επιλύτη της Βελτιστοποίησης Τοπολογίας.

Για αρχή, το πρωτεύον πρόβλημα που μελετήθηκε στο τμήμα 4 αναλύεται εδώ με τη χρήση του επιλύτη του πρωτεύοντος προβλήματος της βελτιστοποίησης τοπολογίας καλούμενος **PPB** (Primal Porosity-Based). Η βασική διαφορά είναι ότι ο επιλύτης αυτός δεν επιβάλλει οριακές συνθήκες στη διεπαφή μεταξύ των περιοχών του πλέγματος αλλά, αυτές εφαρμόζονται έμμεσα με τη χρήση των όρων πηγής στις εξισώσεις. Έτσι, χρησιμοποιώντας ένα βοηθητικό λογισμικό του OpenFOAM$^©$, παράγεται ένα πεδίο πορώδους με τιμή μονάδα στα κελιά που ανήκουν στις πε-

ριοχές Solid1, Solid2 και μηδενική τιμή στα κελιά που ανήκουν στην περιοχή
Fluid.

Μια παράμετρος η οποία αποδείχθηκε ότι έχει μεγάλη επίδραση στα αποτελέσματα του επιλύτη **PPB** είναι το β_{max}. Η παράμετρος αυτή συναντάται στους όρους πηγής των εξισώσεων και επιβάλλει τον μηδενισμό της ταχύτητας στις στερεοποιημένες περιοχές του πεδίου. Με την αύξηση της τιμής του β_{max} η διαπερατότητα του πορώδους μειώνεται και έτσι προσεγγίζεται η συμπεριφορά του απολύτως στερεού. Αφού λοιπόν έγινε μία μελέτη ανεξαρτησίας των αποτελεσμάτων του επιλύτη **PPB** από την αύξηση του β_{max}, ακολούθησε η σύγκριση με τον **PBF2**.

Η σύγκριση των δύο επιλυτών έδειξε ότι οι μεγαλύτερες διαφορές στα αποτελέσματα εμφανίζονται κοντά στη διεπαφή ρευστού-στερεού με μέγιστη απόκλιση κοντά στην είσοδο. Αυτό φαίνεται στο σχ. 6 όπου απεικονίζεται η διαφορά της κατανομής της θερμοκρασίας στην είσοδο μεταξύ των δύο επιλυτών.
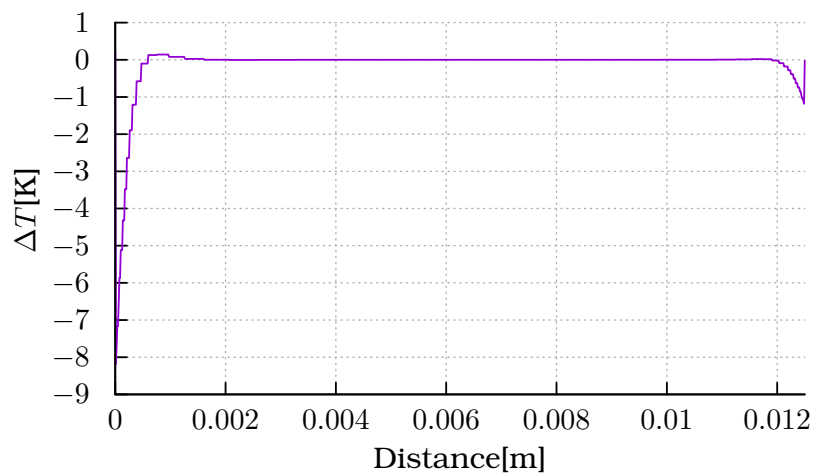
Σχήμα 6: Διαφορές θερμοκρασίας κατά μήκος της εισόδου μεταξύ των επιλυτών **PBF2** και **PPB**.

Η διαφορά αυτή των αποτελεσμάτων, οφείλεται στην απουσία Dirichlet οριακών συνθηκών για τη θερμοκρασία στη διεπαφή στερεού-ρευστού. Αν και η διαφορά στην είσοδο είναι μεγάλη, παρατηρήθηκε ότι οι αποκλίσεις μειώνονται όσο η ροή διασχίζει τον αγωγό.

Η μέση θερμοκρασία που υπολογίστηκε από τον επιλύτη **PPB** στην έξοδο καθώς και οι απώλειες ολικής πίεσης, παρουσιάζονται στον πίνακα 3, μαζί με τα αποτελέσματα των **PBF1** και **PBF2**.

	PBF1	**PBF2**	**PPB**
$T_{out}[\mathrm{K}]$	629.6	630.1	630.3
$\Delta p_t[\mathrm{Pa}]$	1.396	1.395	1.394

Πίνακας 3: Μέση θερμοκρασία ρευστού στην έξοδο και απώλειες ολικής πίεσης για το πρωτεύον πρόβλημα από τους τρεις επιλύτες.

5.1 Βελτιστοποίηση Τοπολογίας

Για τη βελτιστοποίηση τοπολογίας, δημιουργείται ένα νέο πλέγμα το οποίο είναι δομημένο. Αυτό γίνεται διότι το σύνηθες στη βελτιστοποίηση τοπολογίας είναι να χρησιμοποιείται δομημένο πλέγμα καθώς η γεωμετρία είναι άγνωστη. Το πλέγμα φαίνεται στο σχ. 7 και θα καλείται PM1 (Porosity Mesh).
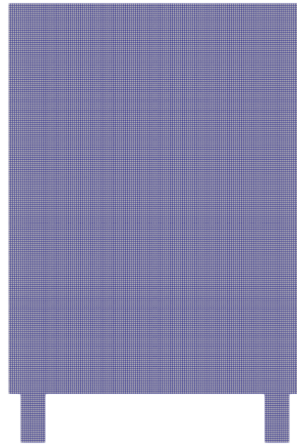
Σχήμα 7: Δομημένο πλέγμα για τη βελτιστοποίηση τοπολογίας (PM1).

Παρατηρείται ότι έχουν προστεθεί στο υπολογιστικό χωρίο εξοχές στην είσοδο και την έξοδο, οι οποίες ωστόσο δεν συμμετέχουν στη βελτιστοποίηση. Αυτό γίνεται ώστε η κατανομή της ταχύτητας να έχει σχηματιστεί προτού η ροή εισέλθει στον χώρο σχεδιασμού, όπου δεν υφίστανται οριακές συνθήκες στη διεπαφή ρευστού-στερεού.

Η συνάρτηση-στόχος παραμένει η ίδια με αυτήν που χρησιμοποιήθηκε για τη βελτιστοποίηση μορφής, η οποία περιγράφεται από την εξ. 1. Έχει προστεθεί ένας περιορισμός για τον λόγο του όγκου του ρευστού προς τον συνολικό ο οποίος ισοδυναμεί με αυτόν της αρχικής γεωμετρίας με τον καμπύλο αγωγό (σχ. 2). Γίνεται βελτιστοποίηση για τρία διαφορετικά βάρη $w = \{0.95, 0.9, 0.8\}$. Οι γεωμετρίες που προκύπτουν φαίνονται στο σχ. 8.
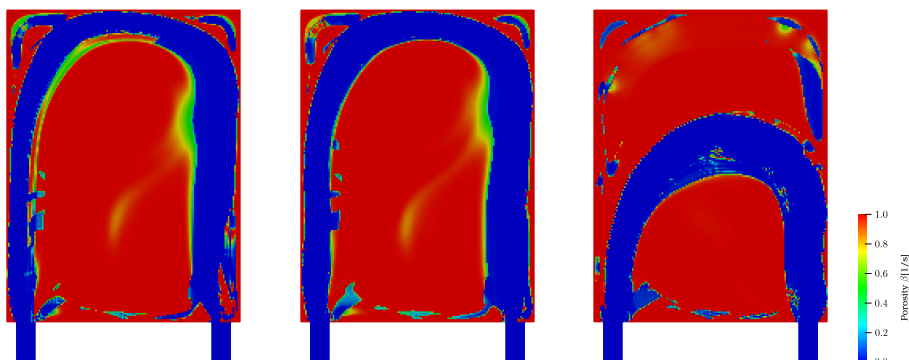
Σχήμα 8: Βέλτιστη γεωμετρία για $w = 0.95$ (αριστερά), $w = 0.9$ (μέση), $w = 0.8$ (δεξιά).

Παρατηρώντας το παραπάνω σχήμα, φαίνεται πως όσο μειώνεται η τιμή του w η γεωμετρία γίνεται πιο ομαλή. Στις περιπτώσεις $w = 0.95$ και $w = 0.8$, ο αγωγός

πλησιάζει τα θερμά τοιχώματα με αποτέλεσμα την αύξηση της θερμοκρασίας στην έξοδο. Αντιθέτως, στην τρίτη περίπτωση για $w = 0.8$ ο αγωγός έχει μικρότερο μήκος αλλά μεγαλύτερο πλάτος, το οποίο έχει ως αποτέλεσμα μικρότερες ταχύτητες ροής σε σχέση με τις άλλες δύο περιπτώσεις και άρα μικρότερες απώλειες ολικής πίεσης. Παράλληλα, στην περίπτωση όπου $w = 0.95$, παρατηρείται μπλοκάρισμα της εξόδου από στερεό, το οποίο παρότι αυξάνει τις απώλειες ολικής πίεσης, αυξάνει επίσης τη θερμοκρασία εξόδου της ροής.

Η μέση θερμοκρασία εξόδου της ροής και οι απώλειες ολικής πίεσης για τις παραπάνω γεωμετρίες, παρουσιάζονται στον πίνακα 4. Τα παραπάνω αποτελέσματα,

w	T_{out}[K]	Δp_t[Pa]
0.95	764.9	1.291
0.9	698.2	0.709
0.8	605.6	0.274

Πίνακας 4: Μέση θερμοκρασία εξόδου της ροής και απώλειες ολικής πίεσης για τις γεωμετρίες που προέκυψαν από βελτιστοποίηση τοπολογίας.

φαίνεται να απέχουν αρκετά από αυτά των προηγούμενων κεφαλαίων. Ένας σημαντικός παράγοντας που δημιουργεί ανακρίβεια στα αποτελέσματα της βελτιστοποίησης τοπολογίας είναι η ύπαρξη "γκρίζων" ζωνών. Το γεγονός ότι το πεδίο του πορώδους δεν είναι δυαδικό, οδηγεί σε αρκετά προβλήματα όπως είναι η διαρροή ρευστού μέσα στο στερεό και η αλλοίωση των χαρακτηριστικών τις ροής από τους όρους πηγής στις περιοχές που το πορώδες δεν έχει ακριβώς τιμή μηδέν. Αυτά είναι αποδεκτά προβλήματα της βελτιστοποίησης τοπολογίας στην ΥΡΔ παρόλα αυτά, αποτελεί ένα πολύ χρήσιμο εργαλείο για την παραγωγή σχεδίων σε πρώτο στάδιο, τα οποία όμως πρέπει να αξιολογηθούν εκ νέου με μεγαλύτερη ακρίβεια.

5.2 Αξιολόγηση των αποτελεσμάτων βελτιστοποίησης τοπολογίας

Για την αξιολόγηση των αποτελεσμάτων, σχεδιάζεται προσεγγιστικά ένας αγωγός σχήματος U όμοιος αλλά όχι ίδιος με αυτόν που προέκυψε από τη βελτιστοποίηση τοπολογίας (σχ. 8-μέση). Η γεωμετρία του αγωγού φαίνεται στο σχ. 9.
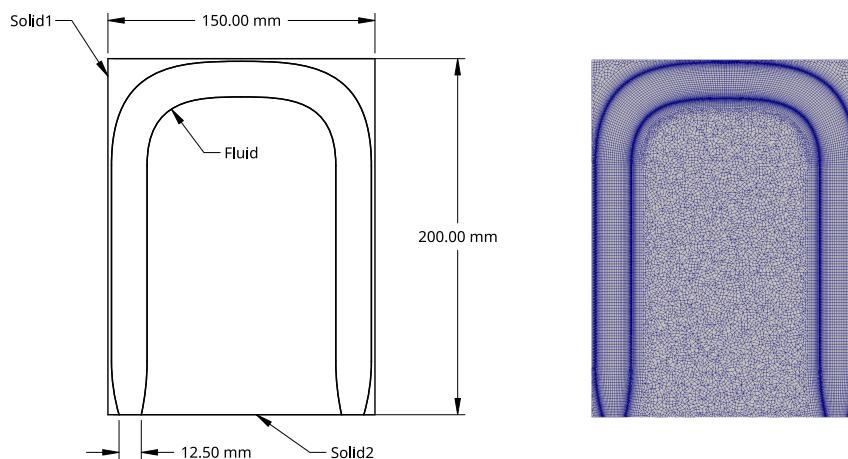

Σχήμα 9: Διαστάσεις (αριστερά) και πλέγμα (δεξιά) αγωγού σχήματος U.

Το πλέγμα αποτελείται από $\sim 16K$ κελιά στην περιοχή Fluid, $\sim 7.5K$ κελιά στην περιοχή Solid 1 και $\sim 16K$ κελιά στην περιοχή Solid 2. Η μέση θερμοκρασία της ροής στην έξοδο υπολογίζεται $T_{out} = 515.2$ K (έναντι του $T_{out} = 698.2$ K) και οι απώλειες ολικής πίεσης $\Delta p_t = 0.119$ Pa (έναντι του $\Delta p_t = 0.709$ Pa).

Όπως ήταν αναμενόμενο, οι αποκλίσεις στα αποτελέσματα είναι σημαντικές και οφείλονται σε έναν συνδυασμό αιτιών. Αρχικά, η γεωμετρία πάνω στην οποία γίνεται η αξιολόγηση, διαφέρει από αυτήν που προέκυψε από τη βελτιστοποίηση. Σημαντική ίσως είναι η παράλειψη του στερεοποιημένου τμήματος της εξόδου που σχηματίζεται από τη βελτιστοποίηση. Δεύτερος λόγος είναι η έλλειψη επιβολής οριακών συνθηκών στη διεπαφή ρευστού-στερεού, η επίδραση της οποίας συζητήθηκε σε προηγούμενο κεφάλαιο. Τέλος, ο σημαντικότερος λόγος είναι η ύπαρξη "γκρίζων" ζωνών στο πεδίο του πορώδους το οποίο είναι και η βασικότερη πηγή σφαλμάτων στη βελτιστοποίηση τοπολογίας.

6 Επανεξέταση Προηγούμενων Συμπερασμάτων σε ένα 2Δ Σύστημα Αγωγών

Για την επανεξέταση των συμπερασμάτων που έχουν εξαχθεί από προηγούμενες μελέτες, γίνεται μία δεύτερη μελέτη που αφορά τον σχεδιασμό ενός 2Δ συστήματος αγωγών. Η γεωμετρία που μελετάται καθώς και το υπολογιστικό πλέγμα που καλείται PM2, φαίνονται στο σχ. 10.
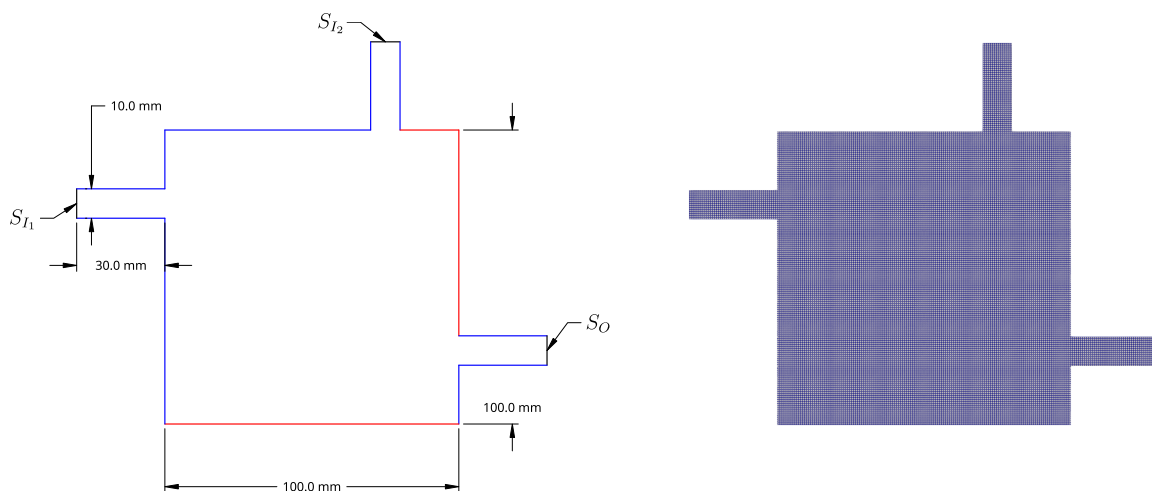
Σχήμα 10: Γεωμετρία (αριστερά) & πλέγμα PM2 (δεξιά) χωρίου 2Δ συστήματος αγωγών. Με κόκκινο σημειώνονται τα θερμά τοιχώματα του χωρίου ενώ με μπλε είναι τα αδιαβατικά.

Το πλέγμα αποτελείται από $\sim 25K$ κελιά. Η διάταξη έχει δύο εισόδους της ροής την S_{I_1} και S_{I_2} και έξοδο την S_O όπως φαίνονται στο σχήμα. Η ροή εισέρχεται με ταχύτητα μέτρου $|v| = 0.01$ m/s και θερμοκρασία $T = 293$ K. Το ρευστό είναι νερό με κινηματική συνεκτικότητα $\nu = 1 \times 10^{-6}$ m^2/s, πυκνότητα $\rho^F = 998.2$ k/m^3, ειδική θερμοχωρητικότητα υπό σταθερή πίεση $c_p^F = 4180$ J/(kgK) και θερμική αγωγιμότητα $k^F = 0.598$ W/(mK). Όλες οι θερμοφυσικές ιδιότητες του ρευστού θεωρούνται

σταθερές. Η ροή είναι στρωτή με $Re = 100$. Τα θερμά τοιχώματα έχουν θερμοκρασία $T = 353\,\mathrm{K}$ και η θερμική αγωγιμότητα του στερεού είναι $k^S = 12.7\,\mathrm{W/(mK)}$ όπως στις προηγούμενες μελέτες.

6.1 Βελτιστοποίηση Τοπολογίας 2Δ Συστήματος Αγωγών

Η συνάρτηση-στόχος ως προς την οποία γίνεται η βελτιστοποίηση τοπολογίας του 2Δ συστήματος αγωγών αποτελείται από δύο επιμέρους στόχους. Πρώτος στόχος είναι η ελαχιστοποίηση της μέσης κατ' όγκο θερμοκρασίας του χωρίου ενώ ο δεύτερος είναι η ελαχιστοποίηση των απωλειών ολικής πίεσης. Αυτό εκφράζεται ως

$$J^{total} = w\hat{J}^{meanT} + (1-w)\hat{J}^{p_t} \tag{2}$$

όπου $w \in [0,1]$ είναι συντελεστής βαρύτητας μεταξύ των δύο στόχων. Το σύμβολο (ˆ) υποδηλώνει την κανονικοποίηση της τιμής του κάθε στόχου με την τιμή που αυτός λαμβάνει στον μηδενικό κύκλο βελτιστοποίησης. Γίνονται τρεξίματα για 4 διαφορετικά βάρη $w = \{0.9, 0.8, 0.5, 0.2\}$ και οι γεωμετρίες που προκύπτουν μετά από 50 κύκλους βελτιστοποίησης φαίνονται στο σχ. 11.
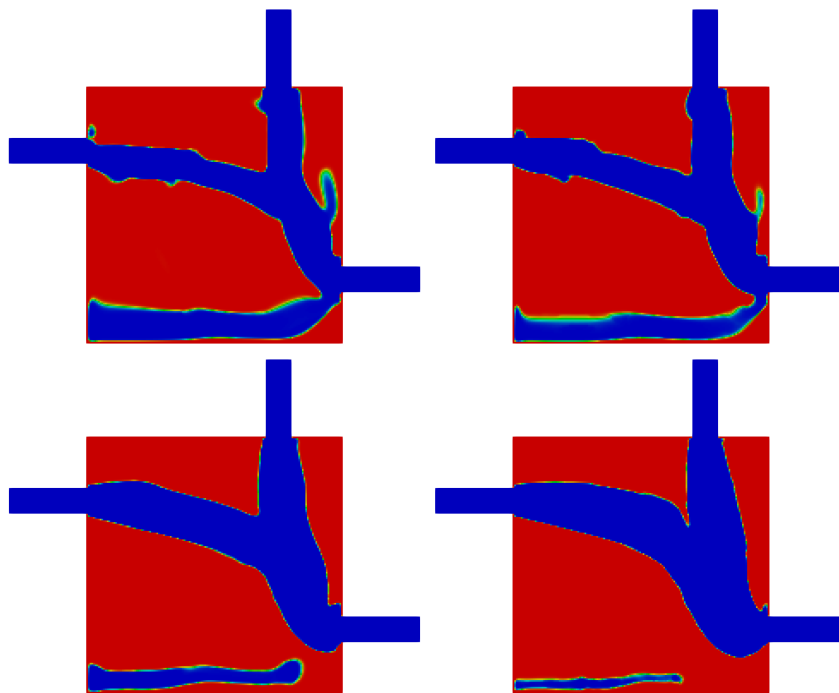
Σχήμα 11: Βέλτιστο πεδίο πορώδους για $w = 0.9$ (πάνω-αριστερά), για $w = 0.8$ (πάνω-δεξιά), για $w = 0.5$ (κάτω-αριστερά), για $w = 0.2$ (κάτω-δεξιά).

Παρατηρείται ο σχηματισμός μίας κοιλότητας ακίνητου ρευστού κοντά στο θερμό τοίχωμα της βάσης του χωρίου. Δεδομένου ότι η θερμική αγωγιμότητα του νερού είναι πολύ μικρότερη από αυτή του στερεού, η κοιλότητα δυσχεραίνει την μεταφορά θερμότητας από το θερμό τοίχωμα στο υπόλοιπο χωρίο, λειτουργώντας έτσι ως θερμική μόνωση. Αυτό έχει ως αποτέλεσμα τη μείωση της τιμής του στόχου J^{meanT}. Συνεπώς, με τη μείωση του w ο όγκος της κοιλότητας μικραίνει ενώ παράλληλα οι αγωγοί αποκτούν μεγαλύτερο πάχος το οποίο συμβάλλει ενεργά στην ελαχιστοποίηση των απωλειών ολικής πίεσης.

Ορίζοντας τον συντελεστή απωλειών ολικής πίεσης, ο οποίος εκφράζεται ως

$$\Omega^{\Delta p_t} = \frac{\Delta p_t}{1/2\rho v^2} \tag{3}$$

οι τιμές των στόχων για την κάθε γεωμετρία παρουσιάζονται στον πίνακα 5.

w	$\overline{T}[\mathrm{K}]$	$\Omega^{\Delta p_t}$
0.9	306.1	17.3
0.8	304.8	15.7
0.5	309.3	14.5
0.2	312.4	14.1

Πίνακας 5: Μέση κατ' όγκο όγκο θερμοκρασία του χωρίου και συντελεστής απωλειών ολικής πίεσης για τις βέλτιστες γεωμετρίες.

## 6.2   Μετάβαση από Βελτιστοποίηση Τοπολογίας σε Βελτιστοποίηση Μορφής

Για την μετάβαση από βελτιστοποίηση τοπολογίας σε βελτιστοποίηση μορφής χρησιμοποιείται ένα βοηθητικό λογισμικό που αναπτύχθηκε από την ΜΠΥΡ&Β/ΕΜΠ το οποίο δημιουργεί σωματόδετα πλέγματα για τις περιοχές των ρευστών και των στερεών, βάσει του πλέγματος της βελτιστοποίησης τοπολογίας και του βέλτιστου πεδίου πορώδους που προέκυψε. Με χρήση του λοιπόν στο βέλτιστο πεδίο πορώδους που προέκυψε για $w = 0.5$ (σχ. 11-(κάτω-αριστερά)), το σωματόδετο πλέγμα που προκύπτει για το ρευστό και το στερεό φαίνεται στο σχ. 12.

Σχήμα 12: Σωματόδετα πλέγματα κατασκευασμένα βάσει του PM2 και του βέλτιστου πεδίου πορώδους για $w = 0.5$. Πλέγμα για την περιοχή του ρευστού (αριστερά) και την περιοχή του στερεού (δεξιά).

Με επίλυση του πρωτεύοντος προβλήματος στο παραπάνω πλέγμα με τον κώδικα **PBF2**, προκύπτουν μέση θερμοκρασία του χωρίου $\overline{T} = 309.1\,\mathrm{K}$ (αντί για $\overline{T} = 309.3\,\mathrm{K}$) και απώλειες ολικής πίεσης $\Omega^{\Delta p_t} = 14.3$ (αντί για $\Omega^{\Delta p_t} = 14.5$) που είναι πολύ κοντά στα αποτελέσματα που προέκυψαν από τη βελτιστοποίηση τοπολογίας.

Για τη βελτιστοποίηση μορφής, η διεπιφάνεια ρευστού-στερεού παραμετροποιείται με ογκομετρικές B-Splines. Τα σημεία ελέγχου φαίνονται στο σχ. 13.
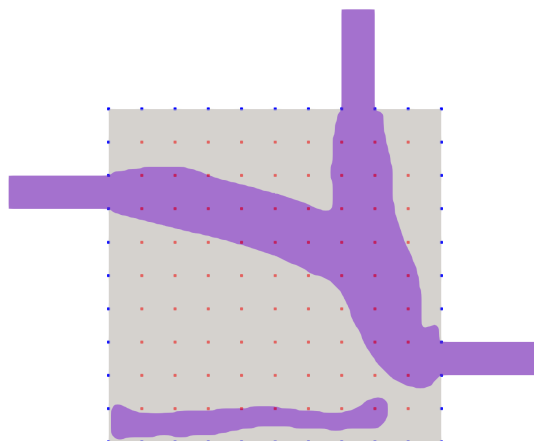
Σχήμα 13: Κουτί ογκομετρικών B-Splines 11×11 που παραμετροποιεί τη γεωμετρία. Τα σημεία ελέγχου με μπλε χρώμα παραμένουν σταθερά, ενώ τα κόκκινα μπορούν να κινηθούν.

Οι γεωμετρίες που προέκυψαν μετά από 10 κύκλους βελτιστοποίησης για τα 4 διαφορετικά βάρη σχεδόν ταυτίζονται και φαίνονται στο σχ. 14 μαζί με την αρχική.
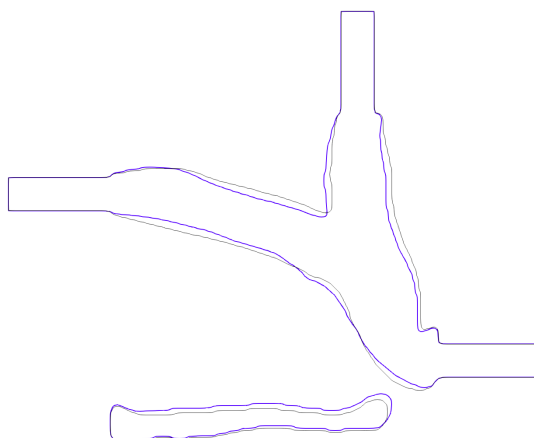
Σχήμα 14: Γεωμετρίες που προέκυψαν από τη βελτιστοποίηση μορφής για 4 βάρη στη συνάρτηση-στόχο. Με μαύρο χρώμα είναι η αρχική γεωμετρία.

Στις βέλτιστες γεωμετρίες, παρατηρείται αύξηση του όγκου της κοιλότητας στάσιμου ρευστού ενώ παράλληλα το πάχος των αγωγών μειώνεται. Τα αποτελέσματα για τις παραπάνω γεωμετρίες καθώς και για την αρχική, φαίνονται στον πίνακα 6.

Γεωμετρία	$\overline{T}[\mathrm{K}]$	$\Omega^{\Delta p_t}$
Αρχική	309.1	14.3
Βέλτιστη	308.7	14.6

Πίνακας 6: Μέση κατ'όγκο θερμοκρασία χωρίου και συντελεστής απωλειών ολικής πίεσης για την αρχική και τις βέλτιστες γεωμετρίες.

Παρατηρείται ότι ενώ επιτεύχθηκε κάποια μείωση της μέσης θερμοκρασίας, οι απώλειες ολικής πίεσης ελαφρώς αυξήθηκαν. Η ελάχιστη διαφορά μεταξύ των

αποτελεσμάτων για τα διαφορετικά βάρη καθώς και η μικρή επίδραση της βελτιστοποίησης στην γεωμετρία, καταδεικνύουν ότι η βελτιστοποίηση τοπολογίας είχε βρει ήδη λύση πολύ κοντά σε τοπικό ελάχιστο της συνάρτησης-στόχου.

Βιβλιογραφία

[1] L. Davis, *Handbook of genetic algorithms*. Van Nostrand Reinhold, 1991, σ. 385.

[2] J. Nocedal και S. Wright, *Numerical Optimization (Springer Series in Operations Research and Financial Engineering)*. Springer, 2006, σ. 664.

[3] A. Jameson, «Aerodynamic design via control theory», *Journal of Scientific Computing*, τόμ. 3, αρθμ. 3, σσ. 233–260, Σεπτ. 1988.

[4] W. K. Anderson και D. L. Bonhaus, «Airfoil Design on Unstructured Grids for Turbulent Flows», *AIAA Journal*, τόμ. 37, αρθμ. 2, σσ. 185–191, Φεβ. 1999.

[5] L. Piegl, *The NURBS Book*. Springer Berlin Heidelberg, 1995, σ. 646.

[6] W. K. Anderson και V. Venkatakrishnan, «Aerodynamic design optimization on unstructured grids with a continuous adjoint formulation», *Computers & Fluids*, τόμ. 28, αρθμ. 4-5, σσ. 443–480, 1999.

[7] K. Gkaragkounis, «The Continuous Adjoint Method in Aerodynamic and Conjugate Heat Transfer Shape Optimization, for Turbulent Flows», Διδακτορική διατρ., NTUA, 2020.

[8] S. V. Patankar και D. B. Spalding, «A calculation procedure for heat, mass and momentum transfer in three-dimensional parabolic flows», στο *Numerical prediction of flow, heat transfer, turbulence and combustion*, Elsevier, 1983, σσ. 54–73.